# HETEROJUNCTION BIPOLAR TRANSISTORS AND ULTRAVIOLET-LIGHT-EMITTING DIODES BASED IN THE III-NITRIDE MATERIAL SYSTEM GROWN BY METALORGANIC CHEMICAL VAPOR DEPOSITION

A Ph.D Dissertation
Presented to
The Academic Faculty


by


Zachary M. Lochner


In Partial Fulfillment
of the Requirements for the Degree
Doctor of Philosophy in the
School of Electrical and Computer Engineering


Georgia Institute of Technology
August 2013

# HETEROJUNCTION BIPOLAR TRANSISTORS AND ULTRAVIOLET-LIGHT-EMITTING DIODES BASED IN THE III-NITRIDE MATERIAL SYSTEM GROWN BY METALORGANIC CHEMICAL VAPOR DEPOSITION

Approved by:

Dr. Russell D. Dupuis, Advisor
School of Electrical and Computer
Engineering
*Georgia Institute of Technology*

Dr. Shyh-Chiang Shen
School of Electrical and Computer
Engineering
*Georgia Institute of Technology*

Dr. P. Douglas Yoder
School of Electrical and Computer
Engineering
*Georgia Institute of Technology*

Dr. Wenshan Cai
School of Electrical and Computer
Engineering
*Georgia Institute of Technology*

Dr. Eric M. Vogel
School of Materials Science and
Engineering
*Georgia Institute of Technology*

 Date Approved:  15 May 2013

# ACKNOWLEDGEMENTS

# TABLE OF CONTENTS

# LIST OF TABLES

# LIST OF FIGURES

ix

# SUMMARY

The material and device characteristics of InGaN/GaN heterojunction bipolar transistors (HBTs) grown by metalorganic chemical vapor deposition are examined. Two structures grown on sapphire with different $p$-In$_x$Ga$_{1-x}$N base-region compositions, $x_{In} = 0.03$ and $0.05$, are presented in a comparative study. The structure with the higher indium content base is expected to provide improvements in device performance due to its higher $p$-type doping efficiency and lower bulk resistivity. However, the D.C. gain for both devices is the same at ~37. The tradeoffs involved with using higher indium composition in the base for $NpN$ HBTs are investigated using atomic-force microscopy, Hall-effect measurement, and device characterization.

In a second experiment, $NpN$-GaN/InGaN/GaN HBTs are grown and fabricated on free-standing GaN (FS-GaN) and sapphire substrates to investigate the effect of dislocations on III-nitride HBT epitaxial structures. The performance characteristics of HBTs on FS-GaN with a $20 \times 20$ $\mu$m$^2$ emitter area exhibit a maximum collector-current density of ~12.3 kA/cm$^2$, a D.C. current gain of ~90, and a maximum differential gain of ~120 without surface passivation. These characteristics represent a substantial improvement over similar devices grown on sapphire. The improved performance is attributed to the reduction in threading-dislocation density afforded by homoepitaxial growth on a high-crystalline-quality substrates. The minority-carrier diffusion length increases significantly owing to both a mitigated carrier-trap effect via fewer dislocations and reduced microscopic localized states.

For the development of deep-ultraviolet optoelectronics, several various structures of optically-pumped lasers at 257, 246, and 243 nm are demonstrated on (0001) AlN substrates. The substantial reduction of the threading-dislocation density in the active region of the laser by using a native substrate over sapphire is critical to the realization of stimulated emission. The $Al_xGa_{1-x}N/AlN$ heterostructures were grown by metalorganic chemical vapor deposition and then the substrate was thinned and the wafer was cleaved into laser bars of various widths. The threshold-power density at room temperature was reduced to as low as 297 kW/cm$^2$. The dominating polarization was measured to be transverse electric in all cases.

InAlN material was developed to provide lattice matched, high-bandgap energy cladding layers for a III-N UV laser structure. This would alleviate strain and dislocation formation in the structure, and also mitigate the polarization charge. However, a gallium auto-doping mechanism was encountered which prevents the growth of pure ternary InAlN, resulting instead in quaternary InAlGaN. This phenomenon is quantitatively examined and its source is explored.

# CHAPTER 1

# INTRODUCTION

III-nitrides have recently come to the forefront of research and development as a possible alternative for next-generation electronic and optoelectronic devices. The wide-bandgap and high thermal stability of III-nitride semiconductors make them ideal for high-power applications. Silicon, the most commonly used semiconductor, has a narrow and *indirect* bandgap, meaning the recombination of electron-hole pairs must generate a phonon, releasing heat to the crystal lattice, before it can emit a photon. Nitrides have a *direct* bandgap, meaning the recombination process can emit a photon directly, giving them a clear advantage over silicon for photonic devices. The bandgap energies of the binary combinations of III-nitrides cover a wide range of the electromagnetic spectrum- from ultraviolet to infrared (Figure 1.1)- making III-nitride materials suitable for a variety of optoelectronic applications.

This thesis will focus on two nitride-based devices: an electronic heterojunction bipolar transistor demonstrating ultra-high power operation and a photonic ultraviolet-light emitter demonstrating stimulated emission. Following a brief introduction to the material system and epitaxial growth technique, the background of each device is

presented with its technical challenges. The experimental approach to solving these

challenges will then be discussed, along with the results obtained thus far. Finally, a

summary of the work completed and a proposal for further research will be presented.
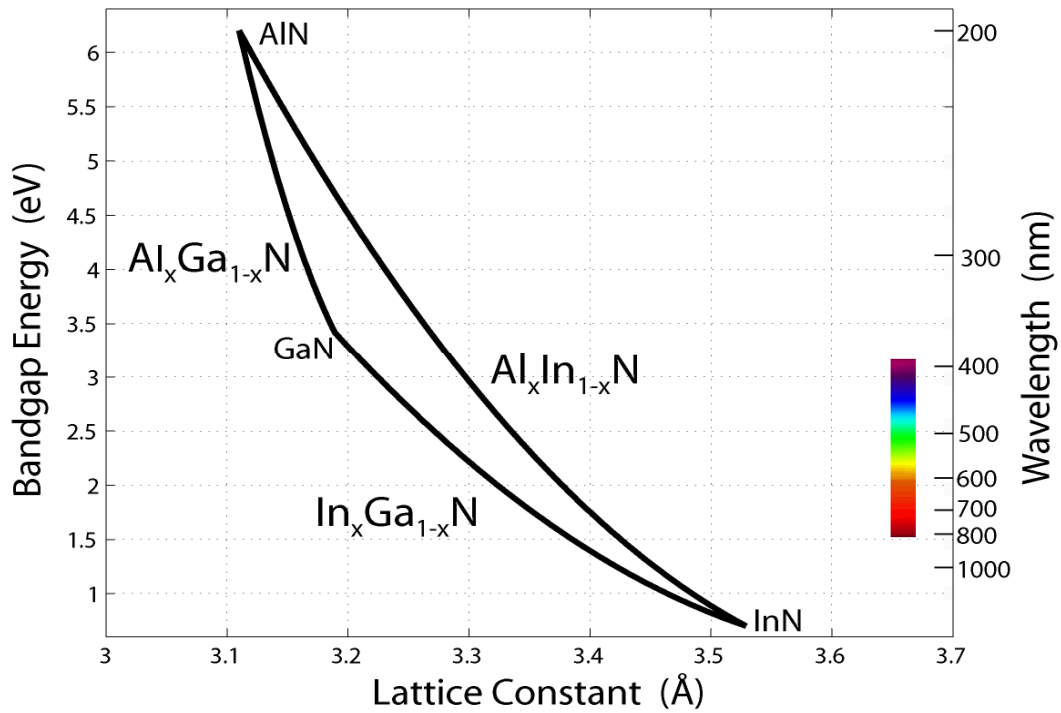


**Figure 1.1 Bandgap energy vs. lattice constant for III-nitride materials.**

## 1.1 III-Nitride Materials

Epitaxial films of GaN were first grown and characterized in 1969 by Maruska

and Tietjen by hydride-vapor-phase epitaxy (HVPE) [1]. The first instance of GaN

epitaxial growth using metalorganic chemical vapor deposition (MOCVD), now the

2

preferred method for devices, was by Manasevit et al. in 1971 [2]. Ternary combinations, such as $In_xGa_{1-x}N$ and $Al_xGa_{1-x}N$, were soon developed. In the ternary combinations, the composition determines the lattice parameter and bandgap as per Vegard's law:

$$a_{In_xGa_{1-x}N}(x) = x \cdot a_{InN} + (1-x) \cdot a_{GaN} + bx(1-x) \text{, and} \qquad (1.1)$$

$$E_{g,In_xGa_{1-x}N}(x) = x \cdot E_{g,InN} + (1-x) \cdot E_{g,GaN} + bx(1-x) \text{,} \qquad (1.2)$$

where $E_g$ is the bandgap energy, $a$ is the lattice parameter, $x$ is the % alloy composition (in $In_xGa_{1-x}N$ or $Al_xGa_{1-x}N$), and $b$ is the bandgap bowing parameter specific to each compound and determined experimentally.

The nitrides have a hexagonal/wurtzite crystal lattice and thus four axes: the c-axis perpendicular to the basal planes, and three a-axes perpendicular to the c-axis as shown in Figure 1.2. The Bravais lattice of both the hexagonal and trigonal crystal systems are the only two to have 120° rotational symmetry, with the hexagonal system having an addition six-fold symmetry about the c-axis. So while the Miller indices of the hexagonal system can be expressed with just three vectors – $a_1$, $a_2$, and $c$ or (hkl) – an additional vector 120° from $a_1$ and $a_2$ is often used to yield the four-axis Miller-Bravais

indices in the form (*hkil*). Since the intercept of the plane on this $a_3$ axis is determined by its intercept on $a_1$ and $a_2$, the Miller-Bravais indices share the relationship: $i = -(h+k)$.

In the cubic crystal system, crystal directions given by [*XYZ*] are numerically equivalent to the Miller indices of the perpendicular plane, i.e. [*XYZ*] = [*hkl*]. But this is not necessarily the case for all directions in every other crystal system. This complicates the directional scheme in the hexagonal crystal system, and the conversion from three- to four-index directions is not straightforward.
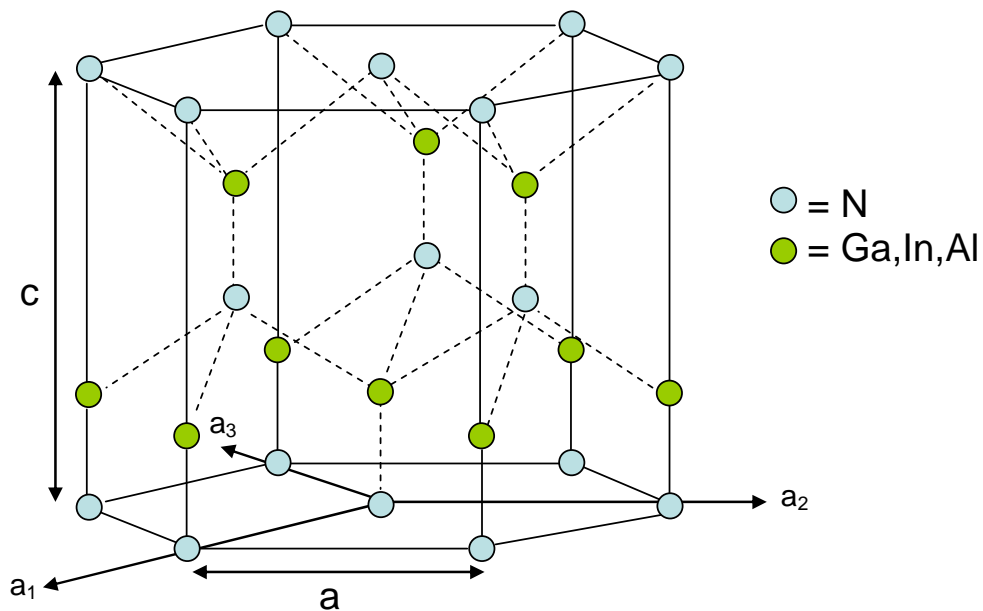


**Figure 1.2 Hexagonal/wurtzite unit cell of III-nitride crystal.**

Directions in a hexagonal lattice can be described by three coordinates: [*XYZ*], corresponding to vectors parallel to $a_1$, $a_2$, and $c$. To recognize the inclusion of the $a_3$

axis, a fourth coordinate is added, yielding a new set of directional vectors, [*uvtw*], such that $u = X + t$, $v = Y + t$, $t = -(u + v)$ and $w = Z$. Note that the sum of the three new basal-plane vectors is equal to zero yielding $t = -(X+Y)/3$. Therefore, converting from three- to four-coordinate directions is accomplished by the following equations:

$$u = X - \frac{(X+Y)}{3} = \frac{2X - Y}{3}, \tag{1.3}$$

$$v = Y - \frac{(X+Z)}{3} = \frac{2Y - X}{3}, \tag{1.4}$$

$$t = -\frac{(X+Y)}{3}, \text{ and} \tag{1.5}$$

$$w = Z. \tag{1.6}$$

The early work in GaN epitaxy was plagued by the lack of lattice-matched substrates. Sapphire ($Al_2O_3$) was commonly used because of its hexagonal symmetry, thermal stability, availability, and low cost. However there is a ~14% lattice mismatch in the c-plane between GaN and the Al bonding sites on sapphire which results in crystal strain and high-defect density formation in the range of $10^{11}$ $cm^{-2}$ for epitaxially grown layers. Furthermore, these early films all exhibited a high background-carrier density of ~$10^{19}$ $cm^{-3}$ which made it difficult to control *n*-type doping, and nearly impossible to create *p*-type conduction. The inability to produce even a simple *pn*-junction, the staple of

semiconductor devices, hindered interest in commercial development of III-nitrides for

many years.

A major breakthrough occurred in 1985 when Amano and Akasaki grew the first

high-quality GaN epitaxial films on sapphire by MOCVD using a low-temperature AlN

buffer layer [3]. The dislocation density was reduced by two orders of magnitude, to $\sim 10^9$

$cm^{-2}$, and the intrinsic-background-electron concentration was lowered to $10^{16}$ $cm^{-3}$. The

low-temperature (LT) buffer layer allows for the nucleation of 3D islands which lowers

the interfacial free energy between the substrate and thin film. The following high-

temperature layers grow laterally across the dense island cluster, resulting in a high-

quality and uniform film.

Because of the reduced background-carrier concentration, $n$-type doping of GaN

layers can now be controlled. Doping in gallium nitride is achieved by atomic

substitution of either Ga or N by a dopant atom. Donor ($n$-type) dopants for GaN include

group IV elements, notably germanium and silicon. These elements act as donors since

they favor replacement of the Ga atom over N because of the lower difference in covalent

radii as can be seen in Table 1.1. Doping efficiency is quite high for silane ($SiH_4$), with

reported carrier concentrations as high as $n = 2$ x $10^{19}$ $cm^{-3}$ via MOCVD [4]. Silane

doping was also found to maintain crystal quality, even at high doping concentrations.

**Table 1.1 Covalent radii of gallium, nitrogen and common GaN dopants.**

| Atom | Covalent Radius (Å) |
|---|---|
| Gallium | 1.26 |
| Nitrogen | 0.75 |
| Silicon | 1.11 |
| Germanium | 1.22 |
| Magnesium | 1.36 |
| Indium | 1.44 |
| Aluminium | 1.18 |

Magnesium is a commonly used acceptor that replaces the Ga atom as is the case with silicon. However, magnesium is compensated by hydrogen as grown within the GaN crystal matrix [5]. To activate the Mg acceptor, this hydrogen bond must be broken by a method such as low-energy electron-beam irradiation (LEEBI) [6] or thermal annealing [7]. But even then, the doping efficiency is quite low at ~1%, meaning that a magnesium concentration as high as $10^{20}$ $cm^{-3}$ will yield a carrier concentration of only 1 x $10^{18}$ $cm^{-3}$. The covalent radius of Mg is also larger than that of Ga, which leads to degradation of crystal quality at high concentrations.

## 1.2 Metalorganic Chemical Vapor Deposition

The process of MOCVD was pioneered by Manasevit in 1968 [8]. In the years that followed, he was successful in demonstrating the deposition of several various

materials onto semiconductors and insulators, such as GaAs, GaP, GaAlAs, AlN and GaN

[2]. However, these epitaxial layers often suffered from impurity related defects, as the

metalorganic sources and reactor designs were still in their infancy. The first practical

devices grown using MOCVD were the AlGaAs/GaAs-solar cells and quantum-well

injection laser by Dupuis et al. in 1977 and 1978 [9,10]. This set off a flurry of research

in the area which has led to large-scale commercialization of MOCVD-grown devices

such as light-emitting diodes (LEDs) and high-electron-mobility transistors (HEMTs).

The primary use of MOCVD is for the growth of III-V epitaxial layers. It is

favored by industry because it is well developed, scalable, and functions at pressures

close to atmospheric. As the name implies, metalorganic compounds are used as the

precursors. These usually consist of an organic trimethyl- or triethyl- group connected to

a group III metal such as Ga, Al, or In. Group V precursors come in the form of hydrides

such as $AsH_3$ (arsine) or $NH_3$ (ammonia).

As previously discussed, good *n*-type doping can be accomplished with silicon,

using $SiH_4$ as a precursor. The issues surrounding *p*-type doping using magnesium with

bis(cyclopentadienyl)magnesium ($Cp_2Mg$) as a precursor are further complicated by the

"memory effect" in MOCVD [11]: Mg source molecules are prone to sticking to the

walls of the reactor before reaching the substrate. This sticking effect results in reduced

incorporation into the sample or a gradual "turn on" as Mg first adheres to the walls and then to the substrate surface. To avoid this, a pre-growth coating is used to saturate the Mg layer on the reactor walls.

An inert carrier gas, $H_2$ or $N_2$, is used to carry the precursors to the reaction chamber. The precursors are broken down by pyrolysis and adsorb onto the substrate. Epitaxial crystals are formed by the chemical reaction:

$$A_3M\ (g) + EH_3\ (g) \rightarrow ME\ (s) + 3AH\ (g), \hspace{2cm} (1.7)$$
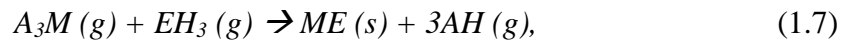
where $A$ is the alkyl group of $CH_3$ or $C_2H_5$, $M$ is the group III metal, $E$ is the group V atom, and $H$ is hydrogen.

Nitride work using MOCVD developed rapidly in the late 1980s, following the major breakthrough of two-step growth by Amano, et al. in 1986 [3]. The same group was successful in $p$-doping gallium nitride in 1989 [6]. In 1992, Nakamura provided the final breakthroughs in the high-quality growth of InGaN on GaN needed for blue and green double-heterostructure-optoelectronic devices via his two-flow reactor design [12]. Commercialization of InGaN/GaN-based blue LEDs and laser diodes (LDs) soon followed in the form of now ubiquitous Blu-ray$^{TM}$ disk players.

The MOCVD reactor used for this thesis research is a Thomas Swan 6 x 2"

rotating disk reactor with a close coupled showerhead (CCS™). The CCS enables for the

intermixing of precursors within close proximity to the substrates, resulting in uniform

deposition. A three-zone heater allows for control of temperature gradients within the

chamber to further control uniformity. A diagram of this system is presented in Figure

1.3.
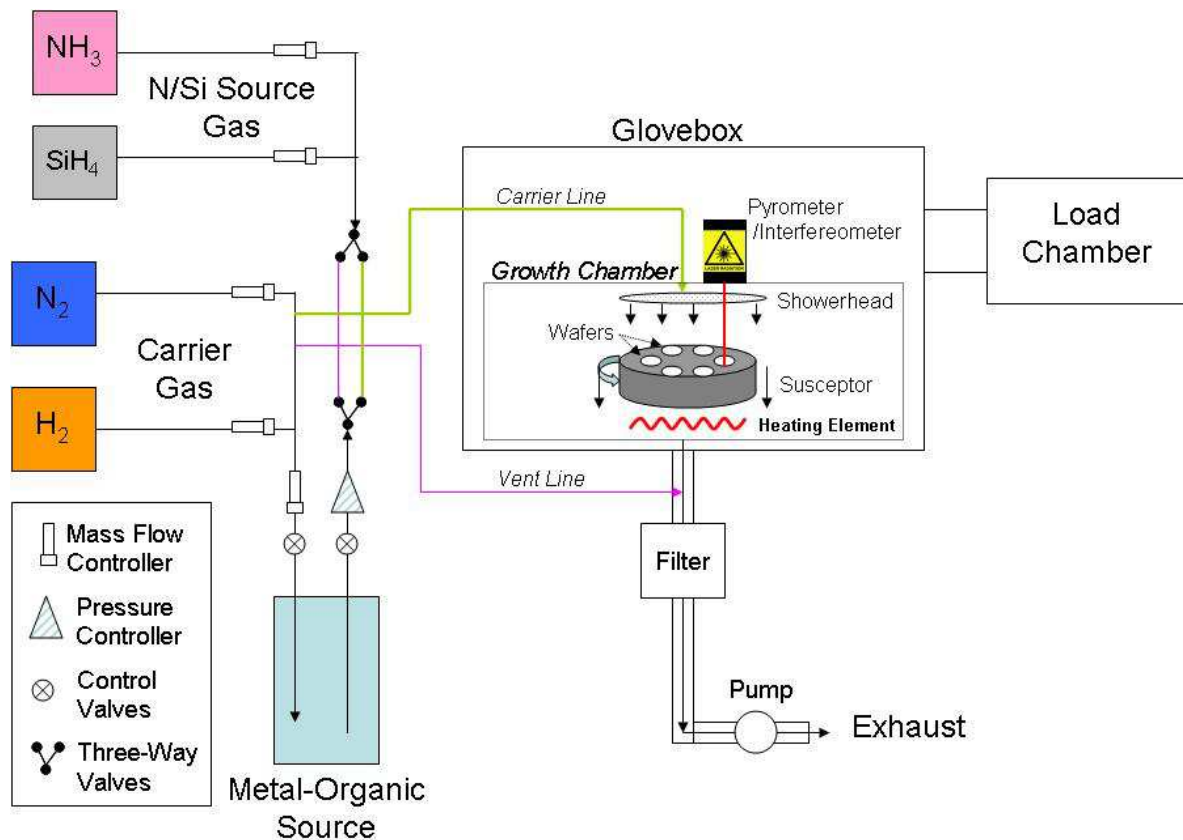


**Figure 1.3 Basic diagram of an MOCVD reactor. Not to scale.**

## 1.3 Motivation for III-Nitride Heterojunction Bipolar Transistors

Wide-bandgap III-nitride based semiconductors have been widely developed over the past decade because of their unique properties which provide advantages over silicon and other III-V materials. They have excellent chemical and thermal stability, and exhibit high-breakdown fields, on the order of 2 MV/cm [13], which make them ideally suited for electronic devices that operate under high temperatures and at high-power densities. One such device is the heterojunction bipolar transistor (HBT) which has been investigated as a high-power amplifier and switch. While much effort has been put forth in III-nitride based heterostructure-field-effect transistors (HFETs), HBTs offer advantages in terms of higher current handling, higher power density, lower 1/f noise, and increased usage of wafer area as vertical fabrication allows for smaller-footprint devices [14,15].

However, the development of bipolar junction transistors has been held back by problems related to material growth and device fabrication. The greatest challenge is *p*-type doping of the III-nitride materials, and fabrication challenges related to forming ohmic contact to *p*-type layers. Nevertheless, the advantages to a practical III-ntride HBT have garnered the attention of several research groups starting around 1999. Most notable are the groups at the University of California at Santa Barbara [16,17], the University of

Florida [18], and the NTT Corporation [19,20,21]. From common-emitter or common-base mode I-V characteristics and Gummel plots, the reported DC current gains range from 3-50 with collector current densities limited to under 10 kA/cm$^2$. These groups used several methods to push the performance of these devices higher, such as emitter regrowth, base regrowth, and growth on SiC substrates for improved material quality.

The majority of efforts in III-nitride bipolar transistors have been focused on *Npn*-AlGaN/GaN HBTs with *p*-GaN as the base (capital letter *N* is used to denote a wider bandgap *n*-type material for the emitter) [22,23,24,25]. These devices benefit from high breakdown fields and large bandgap variance for efficient hole blocking at the base-emitter junction, but their performance is limited by the relatively high acceptor-activation energy (~170 meV) in Mg-doped GaN [26]. This reduces the *p*-type doping efficiency of GaN to about 1%, and the resulting lack of carriers leads to low D.C. gain and a highly resistive base region, which in turn increases the contact resistance and limits high-frequency operation of the device.

Despite their advantageous characteristics, such as higher current handling capabilities and smaller-footprint devices, the development of HBTs based on AlGaN/GaN heterojunction structures, as opposed to the case of steady development of AlGaN/GaN HFETs [27], has been hampered by both serious technical challenges and

relative lack of research efforts: current gain has been limited; large offset voltages as a result of high base contact and sheet resistance; limited power density; and no meaningful RF performance characteristics have been reported [28-30].

This limitation may soon be overcome by the advent of native GaN substrates which have recently become commercially available. Among several native substrates prepared by different techniques, the free-standing GaN (FS-GaN) substrates [31] are the most technologically matured and currently offer a threading-dislocation density below the order of $10^6$ cm-2 with a large size of >2 inch diameter. The reduced lattice strain and dislocation density afforded by the use of FS-GaN is predicted to yield increased gain and current density for HBTs, as has previously been reported for AlGaN/GaN-based *Pnp* devices [32].

In this work, we have optimized the structure of an *NpN-* GaN/InGaN/GaN HBT for growth on a FS-GaN substrate. The use of InGaN for the base allows for a higher *p*-type doping concentration owing to a reduced acceptor activation energy. Coupled with the reduction of strain and defects afforded by homoeptixaial growth on FS-GaN, we were able to achieve a higher gain and much higher power density than previously reported. Thus III-N HBTs are closer to widespread use in practical applications than ever before.

## 1.4 Motivation for III-Nitride Deep Ultraviolet Light Emtiters

Owing to the III-nitride direct bandgap and the commercial success of blue GaN LEDs [33], a primary focus of III-nitride research has been for optoelectronic applications. By tailoring the alloy composition using aluminum, gallium, and indium, a tunable bandgap is obtained from 0.7 eV (InN) to 6.20 eV (AlN), corresponding to the wavelengths between 1771 nm and 200 nm (shown in Figure 1.1). Theoretically, the quaternary AlGaInN alloys can provide a wide spectral coverage from the infrared to the deep ultraviolet.

While Nakamura introduced InGaN-based candela-class LEDs and laser diodes in the early 90's that have since been well developed [34], the wider-bandgap AlGaN-based nitride materials, candidates for ultraviolet (UV) light-emitting diodes (LEDs) and injection lasers, are less developed. In the 2000s, as epitaxial growth technology continued to improve, there was a surge of research activity in the development of UV optoelectronic devices based on the wider bandgap III-nitride semiconductors [35,36]. Such a solid-state, high-efficiency UV light source could be employed in a variety of applications in water purification, food sanitation, bio-agent detection, optical memory storage, and medical sterilization [37,38,39,40]. Conventional sources of UV radiation include high pressure mercury lamps and excimer lasers, which suffer the disadvantages

of containing toxic materials and low portability. A compact and efficient semiconductor device emitting in the germicidal UV range is therefore a desirable alternative.

The wide-bandgap III-nitride material system, specifically AlN and its composites: AlGaN and AlInGaN, can access the entire ultraviolet spectral range including near (320-400 nm) [41,42], middle (280-320 nm) [43,44], and deep-UV (200-280 nm) [45,46]. However, a number of difficulties arise as one increases the aluminum mole fraction to achieve a wider bandgap and shorter wavelength. The formation of cracks and dislocations in the epitaxial layers associated with lattice strain relaxation act as carrier traps that inhibit radiative recombination, thus lowering the output efficiency and increasing the power threshold for stimulated emission [47]. These defects must be reduced or eliminated in high-aluminum-containing structures to achieve high-power operation and lasing in the deep-ultraviolet (DUV) spectral range. A summary of the results thus far for sub-300 nm lasers is listed in Table 1.2.

Nitride materials are typically grown via heteroepitaxy on non-native substrates such as sapphire or SiC because of their relative availability and low cost compared to AlN and GaN substrates. However, the difference in lattice constants and thermal conductivities of heteroepitaxially grown materials leads to strain relaxation, cracking and dislocation formation during growth that is particularly severe for higher aluminum

contents [48]. Therefore, electrical-injection UV-LDs are thus far limited to an emission wavelength of 336 nm due to limitations in material quality and effective doping of AlGaN with high aluminum content [49]. Dislocation reduction techniques such as the inclusion of a low-temperature nucleation layer [50], superlattices [51], graded layers [52], and epitaxial lateral overgrowth schemes [53] have been used to some degree of success in UV emitters. However, emission in the sub-300 nm spectral range remains elusive, especially for laser diodes, where a minimized defect density is critical for the realization of stimulated emission. Optically pumped AlGaN multi-quantum well (MQW) structures have been reported for wavelengths as short as 241.5 nm on SiC, however the threshold power density was relatively high [54].

In this work, we have demonstrated stimulated emission from an AlGaN based multi-quantum well below 250 nm via optical pumping. Defect reduction via homoepitaxial growth on AlN substrate is crucial to this goal. Optimizations of the layer structure and growth techniques have allowed us to reduce the threshold density to 297 kW/cm$^2$.

**Table 1.2 Summary of sub-300 nm lasers**

| Affiliation | Laser structure (Active; Waveguide; Cladding; Substrate) | Excitation wavelength (nm) | Cavity length (mm) | $\lambda$ (nm) | $P_{th}$ (kW/cm$^2$) | Journal Source |
|---|---|---|---|---|---|---|
| Kohgakuin University | $Al_{0.66}Ga_{0.34}N/Al_{0.76}Ga_{0.24}N$ MQW $Al_{0.76}Ga_{0.24}N$ WG $Al_{0.84}Ga_{0.16}N$ clad 4H-SiC substrate | 193 | 0.45 | 241.5 | 1200 | APL **84**, 3567 (2004) |
| Ioffe Physical-Technical Institute, Russia | $Al_{0.39}Ga_{0.61}N/Al_{0.49}Ga_{0.51}N$ MQW $Al_{0.49}Ga_{0.51}N$ WG $Al_{0.66}Ga_{0.34}N$ clad Sapphire substrate | 266 | 1 | 303 | 800 | APL **96**, 14112 (2010) |
| Palo Alto Research Corporation | 3x $Al_xGa_{1-x}N/Al_yGa_{1-y}N$ MQWs n-type $Al_{0.7}Ga_{0.3}N$ layer AlGaN cladding AlN substrate | 248 | 1 | 267 | 126 | APEX **4**, 092101 (2011) |

## 1.5 Motivation for InAlGaN material

While InGaN and AlGaN have been well developed, the third ternary of the conventional III-nitride system, InAlN, has been less so. InAlN offers many attractive benefits in terms of crystal quality and device performance resulting from its ability to lattice match the other ternary compounds, but with a higher bandgap energy. In heterojunction-field-effect transistors, InAlN can be used as the barrier layer with variations in the composition leading to tensile strained, lattice matched, a compressively strained configurations for both depletion and enhancement-mode operation [55,56]. The higher bandgap is extremely beneficial for ultraviolet emitters, as InAlN can theoretically be used as a cladding layer by providing optical and electrical confinement while still being lattice matched to the active region [57]. The reduction in interface strain at each heterojunction would serve the purpose of reducing the quantum confined stark effect resulting from piezoelectric fields, and reducing interface polarization charge which inhibits the flow of carriers and disrupts carrier wavefunctions.

However, there are several practical difficulties in growing InAlN in dealing with the competing conditions for optimal InN and AlN growth. InN requires a low temperature (~800º C), a $N_2$ carrier gas environment, a high V/III ratio and high pressure, whereas AlN is optimized under the opposite conditions: a high temperature (>1200º C),

a $H_2$ carrier gas, a low V/III ratio and low pressure. Further complications arise because of the mismatch in covalent radius, with indium being much larger than aluminum, inhibiting its incorporation into an aluminum-rich AlN matrix [58,59]. Thus the optimal conditions for growing InAlN are difficult to balance between these competing forces and must be methodically explored.

In our efforts to utilize InAlN in our UV devices, we noticed a difficulty in controlling the composition of the ternary material. Temperature, pressure, and flow rates all seemed to irregularly affect the amount of indium, leading us to initially believe there to be a state of "compositional locking" within the parameter space. However, the composition also varied amongst runs of the exact same recipe, which defies conventional reasoning. A deeper analysis of the chemical makeup of the material revealed a gallium auto-doping effect to be occurring every time we grew InAlN.

In the literature, we have found few other cases of gallium auto-doping reported. One example is by Trejo and Gillespie et al. but it was not very deeply explored [60,61]. The team used "proprietary techniques" to eliminate the gallium incorporation without further elaboration. Other groups have done significant research on InAlN and not seen any gallium incorporation in RBS and SIMS depth profiles such as Yakovlev et al. in reference 62 and Hums et al. in reference 63, each using a horizontal flow style reactor,

and Manuel et al. who grew InAlN/GaN heterostructures using plasma assisted molecular beam epitaxy in reference 64. The lack of gallium auto-doping in these experiments may be a result of the geometry of their reactors: the exhaust scheme of horizontal flow reactors being more efficient at expelling unused precursors, or in the case of MBE, the nature of the molecular beam is such so as to prevent the formation of the In-Ga eutectic. Unfortunately, there are many studies of InAlN that rely solely on indirect techniques to determine the material composition, such as XRD or photoluminescence, and operate under the assumption that their material is indeed ternary. Methods which would alert these groups to the autodoping effect such as SIMS, RBS, x-ray photoelectron spectroscopy, or energy dispersive x-ray spectroscopy are more rarely used because of cost and availability. Thus, for our future work, we must operate under the assumption of growing InAlGaN at all times. A survey of previous works focusing on the quaternary material have revealed that the indium composition of epitaxially grown quaternary material is limited by contradicting growth parameters of AlN and InN to $x_{In} < 11\%$ [65,66,67,68]. This coincides with our observations, however there may be techniques that have yet to be developed that would allow greater control over the composition. This would be critical to its encourage its widespread use in III-nitride devices.

## 1.6 Scope of this Dissertation

This work demonstrates the achievement of high performance electronic and optoelectronic devices based in the III-nitride materials system, specifically a heterojunction bipiolar transistor, and deep-ultraviolet stimulated emission from an AlGaN MQW structure. The background and motivation for this work along with a review of the literature has been established in this chapter. Techniques used by the author and the author's colleagues to characterize qualities of III-nitride materials are described in Chapter 2. A basic primer on the semiconductor device basics is presented in Chapter 3. The experimental procedure, device processing details, and experimental data for high-power III-nitride HBTs are presented in Chapter 4. In Chapter 5, deep-ultraviolet stimulated is demonstrated, along with efforts to lower the threshold power density for lasing via process and design optimization. Chapter 6 explores the "auto-doping" phenomenon of InAl(Ga)N, describing a possible cause, and ways to further control the composition. Finally, Chapter 7 is a summary of the work thus far, and provides for possible directions of future work.

# CHAPTER 2

# MATERIAL CHARACTERIZATION TECHNIQUES

Several methods are employed to measure the properties and quality of MOCVD grown epitaxial layers. Since there is often a direct correlation between material quality and device performance, these methods are useful metrics to predict fabricated device performance results. Described here are the characterization techniques of atomic force microscopy, photoluminescence, electroluminescence, scanning electron microscopy, transmission electron microscopy, secondary ion mass spectrometry, Hall-effect measurement, and x-ray diffraction.

## 2.1 Atomic Force Microscopy

The atomic force microscope (AFM) was first developed in 1986 by Binnig, Quate, and Gerber [69]. It consists of five major components: a cantilever, probe tip, sample stage, measurement device, and feedback mechanism. The probe tip is the needle which senses the sample, and must be as sharp as possible to achieve sub nanometer scale resolution. An ideal tip has a diameter of just one atom at its apex. The probe is attached to the cantilever which acts as a spring, the spring constant of which must be extremely

small in order to detect forces in the range of $10^{-8} - 10^{-12}$ N (with a theoretical lower limit of $10^{-18}$ N) and deflections as small as $10^{-4}$ Å according to Hooke's law:

$$F = -kx \qquad (2.1)$$

where $F$ is the force applied, $k$ is the spring constant, and $x$ is the displacement of the spring.

In the original design of the AFM (Figure 2.1a), a scanning tunneling microscope (STM) was used to measure the deflection of the cantilever. Figure 2.1b depicts a modern incarnation of the AFM in which the STM has been replaced with a laser and photodiode, known collectively as the "scanner."
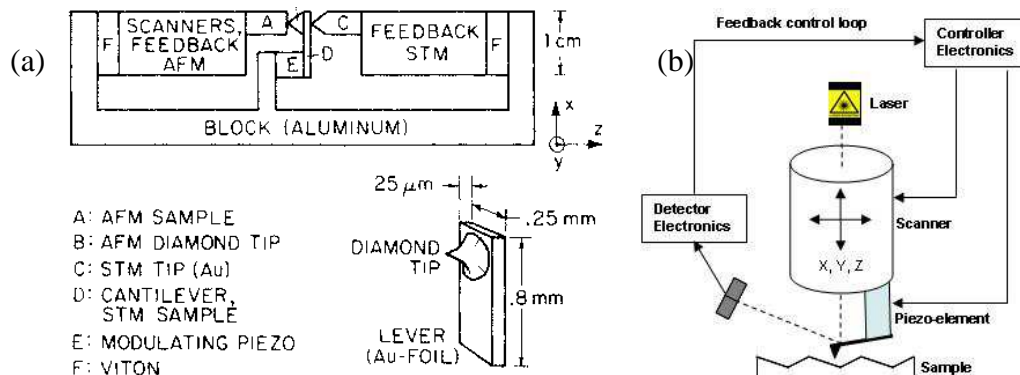


**Figure 2.1 Anatomy of an AFM. (a) The original device invented by Binnig, et al. in 1986 [69]. (b) Modern incarnation of an AFM.**

Atomic force microscopy has three primary modes of operation: contact, tapping, and non-contact. In contact mode, the probe tip is kept in physical contact with the sample at all times as it is raster scanned across the surface. The cantilever deflection is measured by the laser and photodiode and used to construct the image by the detector electronics. The feedback mechanism ensures a constant force between the probe tip and sample surface by a piezoelectric element in the scanner.

In tapping mode, the cantilever is oscillated at its resonant frequency by a piezoelectric element in the scanner, close to the cantilever. The probe tip then taps the sample surface at that frequency. As the cantilever oscillates, the reflected laser also oscillates over the photodiode. The computer measures the amplitude, frequency, and phase of this oscillation to create an image, and also provide feedback to the scanner piezoelectric which will adjust the height of the probe to ensure a constant oscillation frequency.

In non-contact mode, the probe tip is oscillated at or slightly above its resonant frequency. The tip is scanned just above the surface, close enough to be deflected by interatomic force interactions such as Van der Walls forces. These forces dampen the oscillation, which is detected by the laser and photodiode measurement.

The AFM used in this thesis is a Veeco Dimension 3100 scanning probe microscope operated in tapping mode. High resolution (0.01nm) scans are obtained at $5\times5$ $\mu m^2$.

## 2.2 Photoluminescence

Photoluminescence (PL) is an optical characterization technique primarily for determining the band gap energy of a material, but can also be used to determine material quality. The basic premise is based on radiative recombination. If energy is added to a semiconductor in excess of the forbidden energy bandgap, an electron will be excited from the valence band to the conduction band, leaving behind a "hole" which is an imaginary particle, but convenient way to model the lack of an electron. If the energy is very high, electrons can be excited to an energy state above the conduction band, but with no energy barrier in the way, most will naturally fall to the conduction band edge, emitting heat or transferring energy to secondary/Auger electrons. In PL, this excitation energy is in the form of a light source, typically a high energy/short wavelength laser.

For direct bandgap semiconductors, the majority of the electron-hole pairs will recombine at the band-edge energy, emitting photons of the corresponding wavelength as per the relation:

$$E_g = h\nu = h\frac{c}{\lambda},$$ (2.2)

where $E_g$ is the bandgap, $h$ is Plank's constant, $v$ is frequency of light, $c$ is speed of light, and $\lambda$ is the wavelength.

A detector composed of a monochromator and CCD scans the spectrum and records the intensity at each wavelength. The peaks in intensity correspond to the bandgap energy of the material. Since the material is not perfect, each peak will be broadened and thus have a measurable line width. Sub-bandgap levels created by dopants and defects will broaden the spectrum or produce peaks of their own.

PL measurements in this thesis were performed using an 193 nm ArF pulsed-excimer laser as the excitation source. PL measured in this way is not a specific metric of luminous intensity or light output. Rather, it is used to compare the brightness between samples. Therefore, the light intensity in a PL measurement is given in terms of arbitrary

units (a.u.). Data from multiple samples are usually plotted together to determine which is

brighter.


## 2.3 Hall-Effect Measurement

The Hall-effect measurement, as put to practice by L. J. Van der Pauw in 1958

[70], is a simple way to measure the resistivity, majority carrier type, majority carrier

concentration, and carrier mobility of a semiconductor sample. An approximately $1{\times}1$

$cm^2$ square sample is prepared by depositing an ohmic contact to each corner. The contact

is ideally infinitely small, but pragmatically smaller than the distance between contacts.

Indium eutectic is commonly used for contact to n-type III-nitride material, and

evaporated Ni/Ag/Pt for p-type III-N contact.
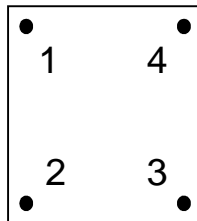
**Figure 2.2 A typical hall sample; variation on Van der Pauw Geometry.**

Free-standing resistivity is measured by applying a current across one pair of contacts and measuring the voltage across the other pair in the two configurations as per the following equation:

$$\rho = 2.266t\left(\frac{V_{43}}{I_{12}} + \frac{V_{23}}{I_{14}}\right)F ,$$
(2.3)

where $t$ is the sample thickness, $I$ is the applied current, $V$ is the measured voltage, and $F$ is a correction factor based on sample symmetry (1 for a perfect square).

Carrier concentration and mobility are derived from the Hall coefficient. When a magnetic field is applied perpendicular to an applied current, the resulting Lorentz force pushes the carriers to one side, creating an electric field normal to the current. The voltage produced by this electric field yields the Hall coefficient by

$$R_H = \frac{V_h \cdot t}{I \cdot B} ,$$
(2.4)

where $V_h$ is the Hall voltage, $t$ is the sample thickness, $I$ is the applied current, and $B$ is the applied magnetic field. The polarity of $V_h$ is determined by the material: positive for $p$-type and negative for $n$-type. The free-carrier concentration and mobility follow thusly:

$$N = \frac{1}{qR_H}, \text{ and} \tag{2.5}$$

$$\mu = \frac{R_H}{\rho}. \tag{2.6}$$

The Hall measurements carried out for this thesis were performed using an Accent HL5500PC Hall measurement system.

## 2.4 Secondary Ion Mass Spectrometry

Secondary ion mass spectrometry (SIMS) is a powerful method that produces a 2D profile of a sample in the form of atomic concentration as a function of depth. Layer thickness, doping concentration, background contamination concentrations and interface quality can thus all be observed empirically. The drawback is that this is a destructive process.

In SIMS, the sample is sputtered by a primary ion beam composed of an ionized species such as $O_2^+$ or $Cs^+$. Atomic and molecular secondary ions are thus released from

the sample surface. A mass analyzer scans the spectrum of mass to charge ratios and counts the ions at each step (in ions per second). Since every element has a roughly unique mass to charge ratio, the peaks of the ion counts correlate to the elements under investigation. As the sample is sputtered, the ion count is plotted over time for each element. At the end of the sputtering, the depth of the sputtered crater is measured using a profilometer. That depth divided by time yields average sputter rate from which an elemental depth profile can be calculated. The ion count is converted to elemental concentration (atoms/cc) via the following equation:

$$C_E = RSF \cdot \frac{I_E C_M}{I_M} \qquad (2.7)$$

where $C_E$ is the concentration of the element of interest, $RSF$ is its relative sensitivity factor, $I_E$ is the secondary ion intensity for the element of interest, $C_M$ is the major/matrix element concentration, and $I_M$ is the ion intensity of the major element. The concentration versus depth profile is thus obtained.

## 2.5 Scanning Electron Microscopy

Scanning electron microscopy (SEM) is a powerful tool in micro- and nano-electronics allowing surface resolution to the nanometer scale, and exceeding 100,000x magnification. The basic premise revolves around inelastic electron scattering.

In a typical SEM, an electron gun produces a beam via thermionic emission from a tungsten filament. These electrons have energies on the scale of several keV. The beam is focused and accelerated by a magnetic coil. When the narrow beam is incident upon the sample surface, the high-energy primary electrons excite the sample, and are able to cause the discharge of secondary electrons. As the primary beam is raster scanned over the sample surface, secondary electrons with different energies and trajectories are released. These secondary electrons are gathered by a detector and processed via computer into an image of the surface. The detector is able to filter out the secondary electrons from stray primary electrons, and any electromagnetic radiation that results from electron bombardment of the surface. Thus a very good picture of the surface morphology of a sample can be obtained.

One drawback of the SEM is that it must be performed under high vacuum to prevent atmospheric scattering of the electron beam. It also has difficulty measuring insulating samples for extended periods of time. Note that the measuring mechanism is

by definition electrically charged. A conducting sample is able to evenly distribute this charge while an insulating sample will yield a charge buildup in the scan area over time. This built-up charge can deflect the primary beam, causing a shift in the image. Therefore, SEM for III-nitride samples is best done in a short amount of time and over larger areas (micron scale) to prevent any large buildup of electrons in a small area.

## 2.6 Transmission Electron Microscopy

The resolution of a conventional optical microscope is limited to a few hundred nanometers by the wavelength of light ($\lambda$) and its numerical aperture ($NA$) and given by:

$$r = \frac{0.61\lambda}{NA}. \qquad (2.8)$$

As such, optical imaging requires a smaller wavelength to resolve smaller features. One way to overcome this barrier to take advantage of the wave-particle duality of electrons. The wavelength of an electron depends on its accelerating energy, and is typically less than one angstrom at several hundred kV.

In a TEM, electrons are generated in similar fashion to that of the SEM, via thermionic emission from a tungsten filament and then focused by electro-magnetic coils

acting as the analog to optical lenses. But, as the name implies, TEM imaging relies on the transmitted electrons, rather than those absorbed or backscattered. Bright-field images simply measure these transmitted electrons, where denser material with higher atomic number will appear dark. Higher resolution can be obtained by measuring not only transmitted, but also *diffracted* beams: the electron beam will undergo Bragg scattering depending on the angle measured, and thus only those beams which constructively interfere will produce an image. This is particularly useful when measuring distortions in a crystal lattice. Further precision still can be obtained by measuring the phase contrast of these transmitted beams in high-resolution transmission electron microscopy (HRTEM). In practice, the resolution is limited to ~0.05 nm by "lens aberrations" caused by difficulties in magnetic focusing of electron beams [71]. But this is still more than sufficient for imaging crystal planes.

All TEM analysis in this work was performed by our colleagues at Arizona State University under Dr. Fernando A. Ponce.


## 2.7 X-ray Diffraction

X-ray diffraction (XRD) is a useful method to determine the lattice constant, alloy composition, strain, and superlattice period of a crystal structure. The x-ray data used in

this report was obtained with a Phillips X'Pert MRD High Resolution X-ray

diffractometer. The x-ray source emits characteristic Cu $K_\alpha$ radiation that is collimated by

a four-crystal Ge (220) Bartels monochromator, which enables 0.00001° resolution.
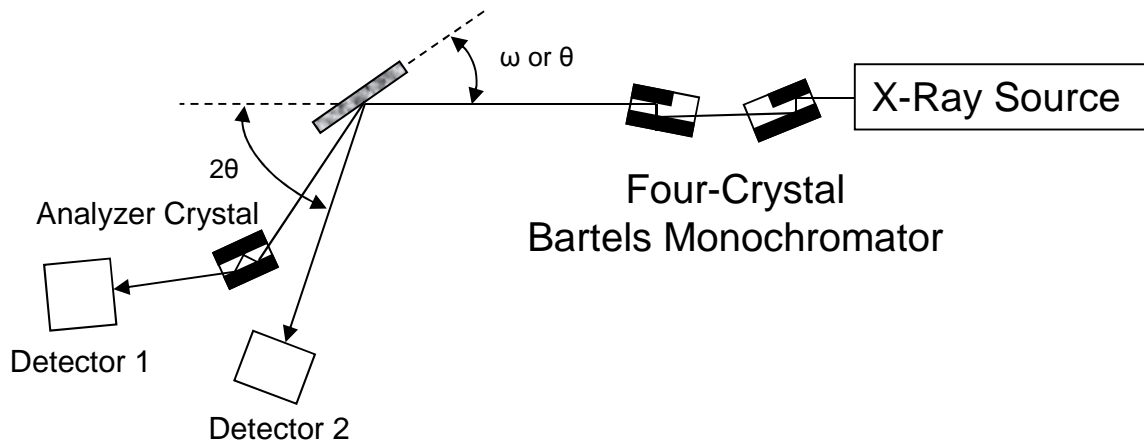
**Figure 2.3 Schematic diagram of an x-ray diffraction setup.**

The basic principle of XRD is based on Bragg's law:

$$n\lambda = 2d_{hkl}\sin\theta_B,$$ (2.9)

where *n* is an integer representing the diffraction order, $\lambda$ is the incident wavelength, $d_{hkl}$

is the spacing of the crystal planes, and $\theta_B$ is the Bragg angle. For a cubic crystal, the

lattice spacing of the plane (*hkl*) is given by:

$$\frac{1}{d_{hkl}^2} = \frac{h^2 + k^2 + l^2}{a^2}.$$ (2.10)

For a hexagonal Bravais lattice, the lattice spacing is given as:

$$\frac{1}{d_{hkl}^2} = \frac{4}{3}\left(\frac{h^2 + hk + k^2}{a^2}\right) + \frac{l^2}{c^2}$$ (2.11)

where $d_{hkl}$ is the spacing between planes, $a$ and $c$ are lattice constants, and $h$, $k$, and $l$ are the Miller indices of the plane of interest. When the x-ray is incident upon the sample at the Bragg angle for a given set of crystal planes (or "Bragg planes"), the reflections from those planes constructively interfere, creating an intensity spike at the detector. Bragg planes of the form (*00l*) are called symmetric planes, while all others are known as asymmetric planes. The *c* lattice constant can be determined from a single symmetric XRD scan by combining equations 2.9 and 2.11 to get:

$$c = \frac{n\lambda l}{2\sin\theta}.$$ (2.12)

The most commonly used XRD scan is the rocking curve otherwise known as the $\omega$-scan. In this configuration, the detector is kept at a fixed angle relative to the primary beam ($2\theta$) while the sample is rotated or "rocked" across the $\omega$ axis, perpendicular to the sample surface as shown in the schematic diagram in Figure 2.3. Rocking curves are useful for determining the $c$ lattice constant via equation 2.12. In a perfect crystal with no strain or defects, the $\omega$-scan produces a $\delta$-function at the Bragg angle. But in the presence of imperfect plane spacing, the Bragg peak is broadened. The full width half maximum (FWHM) or linewidth of this broadened peak is useful for comparing the relative quality of different samples. Asymmetric rocking curves on planes such as $(10\bar{1}2)$ or $(10\bar{1}4)$ can provide more information since the FWHM of these Bragg peaks are sensitive to threading dislocations [72,73].

One drawback of the rocking curve is that since the detector is not moved along with the sample, they have a limited angular range of only ~1°. For III-nitride materials grown on non-native substrates with large lattice mismatch (e.g. sapphire), the Bragg angles for the epitaxial layers are much smaller than that of the substrate such that film/substrate lattice mismatch information cannot be gathered in a single scan.

The $\omega$-$2\theta$ scan can overcome this limitation. In this configuration, the detector moves at twice the angular rotation rate as the sample so that the measured diffraction

angle is always *2θ* with respect to the transmitted incident beam. Therefore, scans over larger angles can be taken and data can be gathered for multiple layers. Furthermore, the diffractions peaks are narrower, reducing the overlap between layers in the diffraction spectrum, allowing for better analysis of individual layers.

Reciprocal space mapping (RSM) is a powerful technique made possible by XRD. In this configuration, an *ω-2θ* scan is plotted against a rocking curve in reciprocal space. The resulting two-dimensional image allows for the analysis of strain and relaxation between layers, in addition to the relative crystal quality of each layer. In an asymmetric RSM, both the *a* and *c* lattice constants can be directly calculated from the reciprocal lattice vectors corresponding to the peak positions. The FWHM of each peak along the *ω* directional corresponds to the "mosaicity" of the associated layer: if it has many disoriented grain boundaries the FWHM will be large, while a more ideal single crystal will have a lower FWHM. The FWHM along *ω-2θ* indicates the level of fluctuations in the *c*-lattice constant, which result from uneven strain in the material or compositional grading. If the centers of each peak are vertically aligned along the same *ω* (i.e. they share a common Bragg angle and thus common plane spacing and common lattice constants) then the layers are fully strained. Displacement of peaks in the horizontal direction indicates that relaxation has taken place. While a basic description has been

given here, a more detailed look at RSM and its geometric significance can be found

elsewhere [74,75].

# CHAPTER 3

# DEVICE BASICS

This chapter will review the operation of bipolar transistors and laser diodes.

Basic device structures and technical challenges will be discussed.

## 3.1 Heterojunction Bipolar Transistors

The bipolar junction transistor (BJT) consists of three regions: the emitter, base,

and collector. These layers are alternately doped forming two back-to-back *pn*-junction

diodes: either *pnp* or *npn*. This work will focus on the latter. As with its cousin, the field

effect transistor, the BJT can function as a switch under proper biasing conditions.

However the doping characteristics of the BJT enable it to obtain high levels of current

gain when a bias is placed along the device and current injected, making it useful as a

power amplifier.

### 3.1.1 Minority Transport and Current Gain

The commonly accepted symbol for an *npn* transistor is shown in Figure 3.1

including applied voltages and currents for forward biasing. The arrow in the symbol

points in the direction of current flow from the emitter. The device is governed by the

flow of minority carriers in the base; in this case, electrons are emitted from the emitter,

drift across the *p*-type base in forward biasing and are collected by the *n*-type collector.
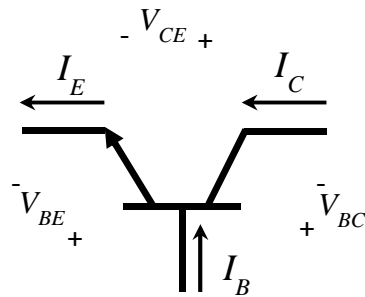
**Figure 3.1 Circuit symbol for an *npn* bipolar junction transistor**

The current flows found in a BJT are further illustrated in Figure 3.2. As electrons

flow across the *p*-type region, some of them will recombine with the majority holes. Hole

injection is provided by the base current to replenish depleted majority carriers. Electrons

that make it across the base contribute to the gain of the device. Thus the D.C. gain ($\beta$) is

given by the equation:

$$\beta = \frac{I_C}{I_B},$$ 

(3.1)

where $I_C$ is the collector current and $I_B$ is the base current. A fundamental assumption of a

BJT is that the width of the base ($W$) is less than the diffusion length of the minority

carrier in the base ($L_B$).

Hole Injection

Emitter

Back-Injection    Base Recombination

Collector

Electron Flow    Current

*n++*          *p+*          *n-*

Emitter      Base      Collector
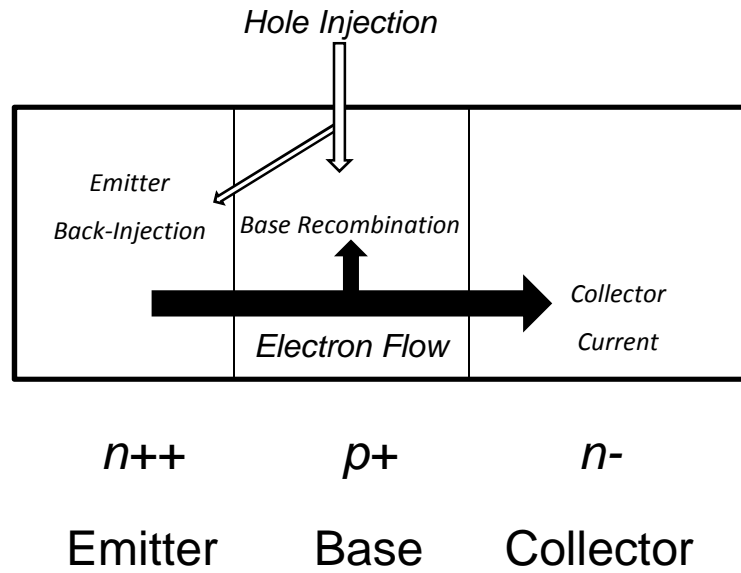
**Figure 3.2 Schematic a BJT summarizing hole and electron flows.**

The emitter back injection consists of holes that diffuse into the emitter. This

reverse current adversely affects the gain of the device, and is quantified by the emitter

injection efficiency ($\gamma$) [76]:

$$\gamma = \frac{I_{En}}{I_{En} + I_{Ep}} = \frac{1}{1 + \dfrac{D_E N_B n_{iE}^2 W}{D_B N_E n_{iB}^2 L_E}}, \tag{3.2}$$

where $I_{En}$ and $I_{Ep}$ are the electron and hole currents in the emitter, $D_E$ and $D_B$ are the diffusion coefficients for the emitter and base, $N_E$ and $N_B$ are carrier concentrations for the emitter and base, $n_{iE}$ and $n_{iB}$ are intrinsic carrier concentrations for the emitter and base, respectively, $W$ is the width of the base, and $L_E$ is the diffusion length of a carrier in the emitter.

### 3.1.2 Homo- vs. Hetero-junction Bipolar Transistor

In a conventional BJT, the doping of the emitter must be larger than that of the base in order to ensure that γ is close to unity; that is $N_E >> N_B > N_C$ must hold in order for the band offsets to discourage emitter current backflow in active biasing. However, this necessarily limits the doping concentration of the base region, and thus increases it's resistance. Another drawback is that it leads to a higher capacitance at the emitter-base junction that limits high frequency performance.

The heterojunction bipolar transistor (HBT) overcomes this drawback with its inherent band offset: the emitter is composed of a larger-bandgap material than the base creating a built-in hole barrier under forward bias. The band diagram of a conventional BJT and HBT (with graded emitter-base junction) is depicted in Figure 3.3. Note that the

base doping of the base region of the HBT is higher than that of the BJT, or $N_B >> N_E > N_C$.

However the back-injection current is minimized by the valence band offset in active-mode biasing as shown in Figure 3.3c.

This is further illustrated by comparing the collector current to the base hole current [77]:

$$I_{Bp} = \frac{qA_E D_{pE}}{X_E} \frac{n_{iE}^2}{N_E} \exp\left(\frac{qV_{BE}}{kT}\right), \text{ and} \qquad (3.3)$$

$$I_C = \frac{qA_E D_{nB}}{X_B} \frac{n_{iB}^2}{N_B} \exp\left(\frac{qV_{BE}}{kT}\right), \qquad (3.4)$$

where $q$ is the elementary charge, $A_E$ is the emitter area, $X_E$ and $X_B$ are the emitter and base perimeters, $D_{pE}$ and $D_{nB}$ are minority carrier diffusion coefficients of the emitter and base, $V_{BE}$ is the base emitter voltage, $k$ is the Boltzmann constant, and $T$ is temperature. As gain is the proportion of collector current to base current, it can thus be written as:

$$\frac{I_C}{I_{Bp}} = \frac{D_{nB} X_E N_E}{D_{pE} X_B N_B} \exp\left(\frac{\Delta E_V}{kT}\right), \qquad (3.5)$$

where $\Delta E_V$ is the valence band offset or the effective hole barrier. For a BJT, this $\Delta E_V$ is zero, thus $N_E$ must be larger than $N_B$ for gain to be above unity. However for an HBT, the exponential of Equation 3.5 is much larger than one, thus allowing for $N_B>>N_E$. For a graded junction HBT, $\Delta E_V$ becomes $\Delta E_g$, yielding even higher gains.

**(a)**

*n++*          *p*          *n*

Emitter      Base      Collector

**(b)**

*n+*          *p++*          *n-*

Emitter      Base      Collector

**(c)**

Forward-Injection Current

$\Delta E_v$

Back-Injection Current

Emitter      Base      Collector
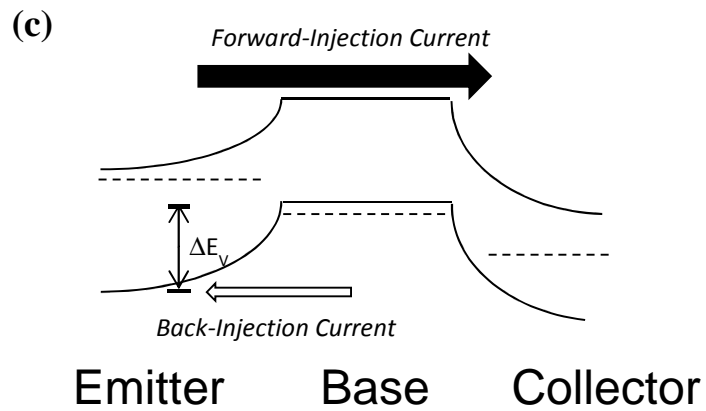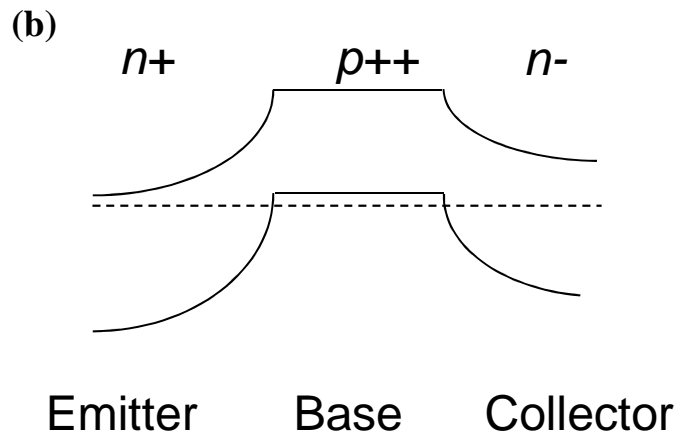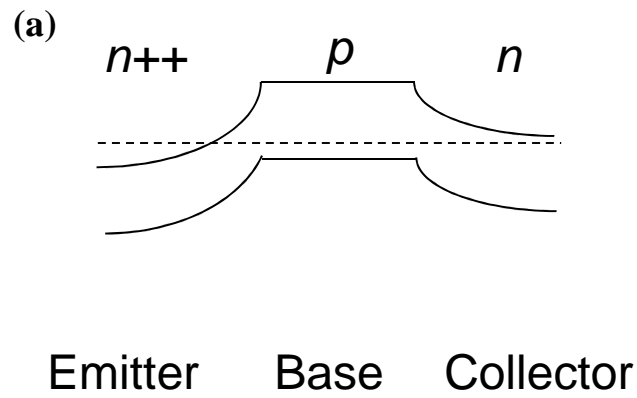
**Figure 3.3 Band diagram of (a) a BJT under zero bias, (b) a HBT under zero bias, and (c) a HBT under forward biasing.**

### 3.1.3 Technical Challenges

While the band offset present in an HBT largely eliminates the back-injection current, and has an emitter injection efficiency close to 1, there remain several other paths of non-ideal conduction within the base. These originate from the several methods of recombination the minority carrier can undergo while moving across the base. They include radiative recombination, where the electron and hole recombine to emit a photon; non-radiative recombination otherwise known as Shockley-Read-Hall recombination, where an electron recombines with a hole via a sub-band gap state(s) related to crystal defects; and Auger recombination, where a an electron recombines with a hole by transferring its energy to another free electron in the conduction band. Each of these components have a specific lifetime and can be combined into the overall minority carrier lifetime as [78]:

$$\tau_n = \left( \frac{1}{\tau_{rad}} + \frac{1}{\tau_{SRH}} + \frac{1}{\tau_A} \right)^{-1}, \tag{3.6}$$

where $\tau_{rad}$ is the radiative recombination lifetime, $\tau_{SRH}$ is the Shockley-Reed-Hall recombination lifetime, and $\tau_A$ is the Auger recombination lifetime. Thus the current gain

of an HBT can quantitatively be defined as the lifetime of a minority carrier relative to

the time it takes that carrier to traverse the base, or:

$$\beta = \frac{I_C}{I_{B,bulk}} = \frac{\tau_n}{\tau_b} \, ,$$
(3.7)

where $I_{B,bulk}$ is the bulk recombination current of the base (which dominates $I_B$ since base

back-injection is near zero) and $\tau_b$ is the base transit time. For example, if the transit time

is 100 ns and an electron is lost to recombination every 2 μs, then the gain of the device

is 20. To improve the gain, the base width can be decreased at the expense of base sheet

resistance and the possibility of base-width modulation, or $\tau_n$ can be increased by

reducing recombination lifetimes. From a material perspective, most control can be

exerted over $\tau_{SRH}$ by reducing the defect density. There are several means of

accomplishing this such as optimizing structure design, adjusting growth parameters, and

reducing lattice strain, all of which will be discussed in a later chapter.

## 3.2 III-N Semiconductor Optoelectronics

### 3.2.1 Electrical Injection and Radiative Recombination

The light-emitting diode (LED) is a *pn*-junction device that functions under forward bias. Charge carriers are injected via electrical contacts: holes at the *p*-type contact, electrons at the *n*-type side. The carriers recombine across the junction, and under the right conditions will emit a photon (Figure 3.4). This is called radiative recombination.
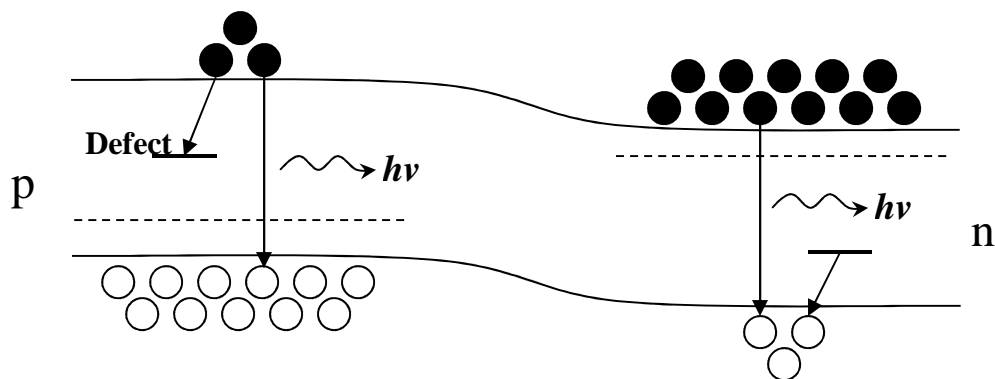


**Figure 3.4 Energy band diagram of a p-n junction under forward bias featuring radiative recombination.**

The wavelength of this light is determined the energy bandgap of the semiconductor as per Equation 2.2. The active region of DUV III-nitride LEDs is typically $In_xGa_{1-x}N$, the bandgap of which is tuned by varying $x$, which in turn tunes the wavelength of emission.

Defects in the material and sub-bandgap energy states can result in non-radiative recombination of carriers, the product of which is a phonon or heat. Radiative and non-radiative recombination are quantized by a parameter known as recombination lifetime by the following relationship:

$$\frac{1}{\tau} = \frac{1}{\tau_r} + \frac{1}{\tau_{nr}},$$

(3.8)

where $\tau_r$ and $\tau_{nr}$ are the radiative and non radiative lifetimes respectively. The probability of radiative recombination occurring is calculated as the internal quantum efficiency (IQE) by:

$$\eta_{IQE} = \frac{1/\tau_r}{1/\tau}.$$

(3.9)

In an ideal case, $\tau_{nr}$ is 0 making the IQE equal to 1. But for practical applications, the technical challenges lie in reducing non-radiative recombination as much as possible by limiting the formation of defects.

### 3.2.2 Double Heterostructures and Quantum Wells

The IQE can be improved if the charge carriers are physically confined, increasing the probability of radiative recombination. One way to accomplish this is with a double heterostructure, where a narrow bandgap material is sandwiched between two materials of larger bandgap, for example AlGaN between AlN as shown in Figure 3.5. Charge carriers always "prefer" lower energy states, and so charge diffusion will concentrate the carriers within the central region. Thus there are more electron-hole pairs readily available for radiative recombination.
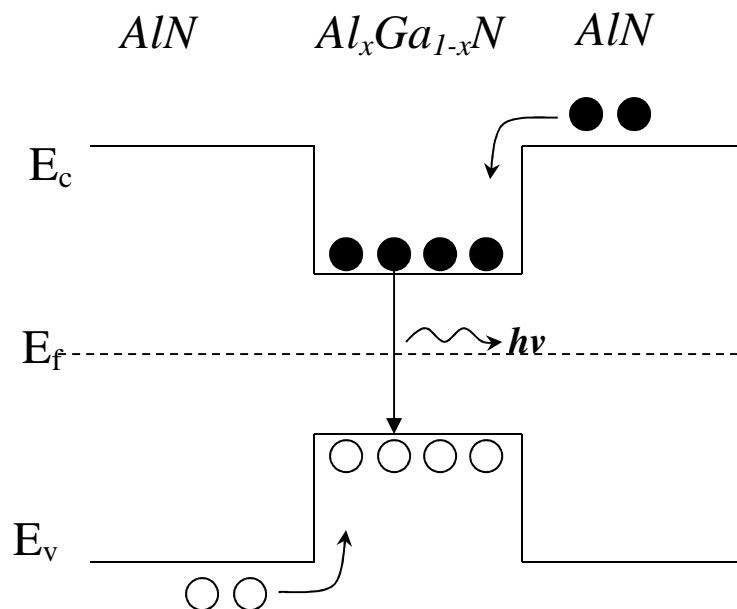


**Figure 3.5 Energy band diagram of a AlN/AlGaN/AlN quantum well with electrical carrier injection and radiative recombination.**

If the central region of this structure is narrow enough, it effectively limits the carrier movement to two dimensions, and is known as a quantum well. In AlGaN LEDs, the well width is typically in the range of 3 nm. This enhanced confinement leads to enhanced IQE. Since there are a finite number of energy states per well, multiple quantum wells (MQW) can be used to prevent band filling, thus increasing the amount of band-to-band radiative recombination.

### 3.2.3 Technical Challenges

Quantum wells are the structure of choice for commercial LEDs. However, they still involve several technical challenges to be overcome, especially as the wavelength approaches 300 nm and below for DUV emission.

Quantum-Confined Stark Effect

Since AlN is a polar structure (when grown in the *c*-axis direction), is contains a spontaneous electric polarization field. Even with no external bias applied, this internal bias will exert influence on carrier motion. Furthermore, built-in strain between hetero-epitaxial layers produces piezoelectric fields, resulting in large internal biases. In quantum wells, this piezoelectric field separates charge carriers, inhibiting the radiative

recombination of electron hole pairs. This is known as the quantum-confined Stark effect

(QCSE), and is particularly important in AlGaN quantum wells undergoing large lattice

mismatch strain when pseudomorphically grown on AlN, where the strength of the

internal fields can be as high as 1-2 MV/cm [79].
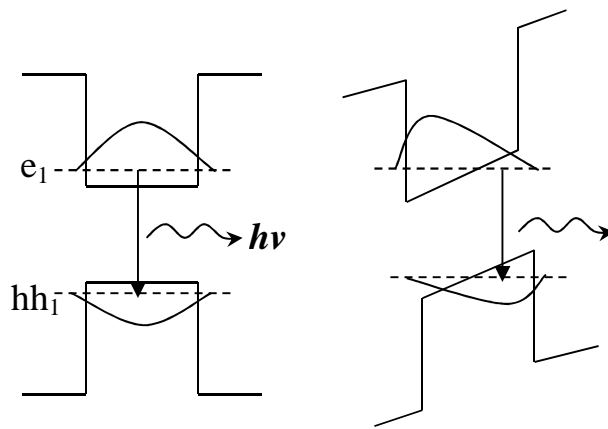


**Figure 3.6 Band diagrams demonstrating the quantum-confined Stark effect. A quantum well with (a) no electric field and another (b) in the presence of an electric field.**

QCSE-induced band bending also allows carriers to recombine at levels below the

bandgap of the material, resulting in a red-shift in the emitted wavelength, particularly at

low injection levels. At higher injection levels, the QCSE is screened as more carriers are

pumped into the wells, reducing charge separation and creating more instances of

electron-hole overlap which favors radiative recombination.

## 3.3 Semiconductor Laser Diodes

### 3.3.1 Stimulated vs. Spontaneous Emission

When an electron-hole pair undergoes band-to-band recombination emitting a photon as described in the previous section, it is known as "spontaneous recombination" due to the random nature of the process, and the resulting photons are emitted in a variety of directions. This is the fundamental operational mode of an LED.

Laser diodes work a bit differently. When a photon with energy $E_{ph} > E_g$ is incident upon a semiconductor, two things can happen: the photon can be absorbed by the material, exciting an electron from the valence to the conduction band, or it can stimulate the radiative recombination of an electron-hole pair, otherwise known as stimulated emission. If this second photon has the same frequency and direction as the first, the two photons create coherent light.
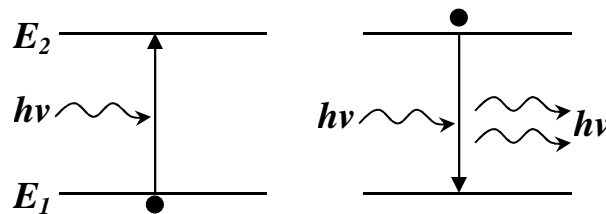


**Figure 3.7 Energy band diagrams featuring (a) photonic absorption and (b) stimulated emission.**

Population inversion occurs when the minority carriers in a *pn*-junction outnumber the majority carriers. This is accomplished either by optical excitation, where the diode is pumped by another laser, or by electrical injection at very high current densities. A diode is said to be "lasing" when population inversion leads to the stimulated emission of coherent light.

Before quantum theory was fully developed, Einstein mathematically described the transition probabilities of absorption, spontaneous emission, and stimulated emission. He considered two energy states, $E_1$ and $E_2$, analogous to the valence and conduction bands in a semiconductor ($E_1 \sim E_v$, $E_2 \sim E_c$), with $E_2 > E_1$ and $E_2 - E_1 = hv$. Each level has a respective electron density, $N_1$ and $N_2$, which are related by Equation 3.10 in equilibrium:

$$\frac{N_2}{N_1} = \exp(-hv/k_B T),\qquad(3.10)$$

where $k_B$ is the Boltzmann constant and $T$ is temperature. In an unperturbed state, $N_1 > N_2$. The probability of a transition from $E_1$ to $E_2$ (i.e. absorption) is given by

$$W_{12} = N_1 \varphi(v) B_{12},\qquad(3.11)$$

where $B_{12}$ is known as the Einstein absorption coefficient and $\varphi(v)$ is the radiation density

of photons with frequency $v$, defined as $\varphi(v)=N_{ph}hv$ where $N_{ph}$ is the number of photons

present. A transition from $E_2$ to $E_1$ can occur as spontaneous or stimulated emission, the

probability of which is:

$$W_{21} = N_2 A_{21} + N_2 \varphi(v) B_{21},$$ (3.12)

where $A_{21}$ and $B_{21}$ are the Einstein coefficients for spontaneous and stimulated emission

respectively, further defined by $A_{21}=1/\tau_r$ and $B_{21} = \lambda^3/8\pi\tau_r$ [80]. Under thermal

equilibrium, the probabilities of upward and downward transition are equal or:

$$N_1 \varphi(v) B_{12} = N_2 A_{21} + N_2 \varphi(v) B_{21}.$$ (3.13)

The Einstein relations also state that $B_{12} = B_{21}$ under equilibrium.

As with an LED, the rate of emission must exceed that of absorption and non-

radiative recombination for a laser diode to break the equilibrium condition and produce

light. Thus $N_2$ must exceed $N_1$, which is population inversion. A laser must also

accomplish the extra feat of having stimulated emission rates exceed that of spontaneous

emission and absorption, so $\varphi(v)$ must reach a critical level. Since $hv$ is fixed, the only

way to increase $\varphi(v)$ is to increase $N_{ph}$. The photon density of a coherent beam of

radiation in a two-level lasing medium is subject to two competing processes: absorption

and stimulated emission. The net loss of photon density per unit time is expressed as:

$$-hv\frac{dN_{ph}}{dt} = N_1\varphi(v)B_{12} - N_2\varphi(v)B_{21} = (N_1 - N_2)\varphi(v)B_{21} \Rightarrow \frac{dN_{ph}}{dt} = (N_2 - N_1)N_{ph}B_{21} \quad (3.14)$$

Again it is clear that in order for the number of photons in the coherent beam to increase

and produce consistent lasing, $N_2$ must be larger than $N_1$. For electrically pumped

devices, this is accomplished when the current density has reached a threshold value such

that the value $N_2$ is large enough to overcome absorption and spontaneous emission. In a

steady state, the change in $N_2$ is zero as each injected carrier spontaneously recombines

(so that $N_2$ never reaches $N_1$). This is quantitatively described by the equation:

$$\frac{dN_2}{dt} = \frac{J}{qd} - \frac{N_2}{\tau} = 0, \quad (3.15)$$

where *J* is the injection current density, *q* is electron charge, *d* is the thickness of the lasing medium, and $\tau$ is the recombination rate. To overcome this steady state, the threshold electron density must be breached. The corresponding threshold injection current density to accomplish this is extracted from Equation 3.15 and given by

$$J_{th} = \frac{qdN_{2,th}}{\tau} \, .$$

(3.16)

The threshold current density is one of the primary figures of merit for a laser diode, the lower the better. It can be improved a number of ways, for example: quantum wells within the *pn*-junction enhance population inversion via quantum confinement, which in turn enhances stimulated emission. Thus quantum wells are often found in the structures of III-nitride laser diodes. A further discussion on the quantum mechanics of lasing action can be found in the literature [81,82].

## 3.3.2 Optical Confinement

In order to increase the probability of stimulated emission, photons can be confined within the diode, resonating back and forth making several passes over the active region, as opposed to being emitted directly following electron-hole

recombination. This is done via optical waveguides on either side of the active region to confine photons in the transverse directions; the active region and waveguides must have different indices of refraction in order for reflection to occur at the interfaces. This ensures that the optical wave function is only subject to absorption losses within the active region. These losses are quantified by the absorption coefficient, defined as:

$$\alpha = (N_1 - N_2)B_{21}\frac{n_r}{c}, \tag{3.17}$$

where $n_r$ is the refractive index, $c$ is the speed of light, and $N_1$ and $N_2$ are carrier densities of $E_1$ and $E_2$, and $B_{21}$ is the Einstein coefficient for stimulated emission. In order for stimulated emission to occur, this absorption must become negative, by making $N_2 > N_1$ as described previously. Under this condition, Equation 3.17 is negated and is redefined as gain where $g = -\alpha$. But if the optical wave function leaks from the active region into the surrounding layers, the absorption coefficients of those layers are added to that of the active region in an amount proportional to the amount of optical leakage. The result is that total absorption losses are increased, and threshold gain is more difficult to achieve.

In an edge-emitting laser, photons are also lost at the ends of the device. For an LED, this would be fine. However a laser by definition produces a coherent beam of

light, which requires some confinement of the beam to make several passes through the active region resulting in more stimulated emission each time. The losses at these end boundaries are given by:

$$\gamma = \frac{1}{2l} \ln\left(\frac{1}{R_1 R_2}\right)$$

(3.18)

where $l$ is the length of the optical cavity, and $R_1$ and $R_2$ are the reflectivity at each end. Lateral optical confinement is achieved by cleaving the sides of the laser diode. The differences in refractive index at the air-semiconductor interface are sufficient to provide some reflection. This can be enhanced by the subsequent deposition of mirrors to the sides of the cleaved facets, which increase the values of $R_1$ and $R_2$.

The total threshold gain is a sum of the absorption losses within the optical cavity and transmission losses at the ends or $g_{th} = a + \gamma$. Thus good mirror facets, cladding, and material quality are all essential in lowering the threshold current density required to achieve threshold gain and ultimately lasing.

### 3.3.3 Technical Challenges

Strain-Induced Defects

Due to the additional requirement of optical confinement, laser diodes are significantly more complex than light emitting diodes in both epitaxial structure and device fabrication. To enhance transverse optical confinement, the index of the cladding layers must be reduced as much as possible, and thus the bandgap must be extended as much as possible. A common way to do this is by surrounding the AlGaN active regions with AlN. The drawback of this approach is the difference in lattice constant that accompanies bandgap as per Figure 1.1. If the resulting strain is too great, it can lead to crystal lattice relaxation, the product of which is a dislocation and/or cracking. These defects are non-radiative recombination centers and can strongly inhibit if not kill altogether the lasing potential of the diode.

The most common substrate for devices grown via MOCVD is sapphire due to its low cost and ready availability. However, the lattice mismatch between sapphire and AlN is large at around 14%. This leads to built-in strain in the epitaxial layers and increased formation of defects even with the low temperature buffers described previously. The added complexity of a laser diode structure – including contact layers, cladding layers, and the active region – amplifies this strain problem. To eliminate the effect of the

substrate mismatch, native AlN substrates can be grown using sublimation. Growing AlN

layers on a AlN substrate is known as "homoepitaxy." The result is a reduction in overall

lattice strain in the device, which reduces the probability of relaxation and defect

formation. A drawback of these AlN substrates is that they are slow and difficult to grow

making the cost of each individual wafer quite high.

# CHAPTER 4

# III-NITRIDE HETEROJUNCTION BIPOLAR TRANSISTORS

In this chapter, a III-nitride *NpN*-GaN/InGaN/GaN heterojunction bipolar transistor is developed for high-power operation. The several design challenges to be overcome involve *p*-type doping of the base, and difficulties in fabrication of ohmic contacts to *p*-type III-nitride material. Since GaN is chemically resistant to wet etchants, dry etching must be used to expose the base during device fabrication. However, this process damages the *p*-type base, and can lead to type conversion – from *p*- to *n*-type – at the etched surface owing to a plasma-etching induced N deficiency [83]. This makes it challenging to create a *p*-type ohmic contact to an HBT base region. While some work has been done with *pnp* designs [84], low hole doping efficiencies, low hole mobility, collector etch damage and the $Cp_2Mg$ "memory effect" in MOCVD all add extra layers of complexity to the structure.

The acceptor activation energy of InGaN is lower than that of GaN and scales as the bandgap decreases with increased indium content. Thus, higher hole concentrations can be achieved ($p \geq 1 \times 10^{18}$ cm$^{-3}$) in *p*-InGaN:Mg than in *p*-GaN:Mg [85]. The lower bandgap energy of InGaN also makes it suitable for the *p*-type base region of an GaN/InGaN/GaN HBT. Such configurations have been demonstrated with lower base resistance and higher gains than AlGaN/GaN HBTs [86,87]. Reduced etch damage to the base related to the level of indium incorporation has also been reported [88]. To further eliminate base damage as an inhibitor to device performance, some groups have employed a base regrowth design, where epitaxy is repeated after the base has been

exposed [89]. While this method has demonstrated impressive results, its added cost, complexity, and time of manufacture warrants further investigation of single growth designs.

In this work we have characterized the effect of two design considerations for an *NpN*-InGaN/GaN HBT. Firstly, we have studied the effect of indium composition in the base region which will influence the band discontinuity, doping efficiency, strain state, and defect formation. Second, we have utilized a free-standing GaN (FS-GaN) substrate to lattice match the buffer layer and collector regions, yielding significantly reduced dislocation density. Both developments have led to an optimized device for ultra-high-power operation.

## 4.1 Effect of Base Composition on GaN/In$_x$Ga$_{1-x}$N-Heterojunction Bipolar Transistors

One technical challenge of InGaN growth is the temperature requirement dictated by its thermal instability. Indium content decreases with increasing growth temperatures, so a low temperature is required to ensure sufficient indium incorporation, typically in the range of 850 °C for low [In] content In$_x$Ga$_{1-x}$N. Since high-quality GaN is typically grown around 1050 °C, some compromise must be made between the growth conditions of the InGaN base and the overlying GaN emitter. Higher temperatures preclude higher indium contents, so the compromise must be made by the GaN emitter which inevitably results in reduced crystal quality, and is a limiting factor on the performance of the device as a whole. Another challenge lies in avoiding lattice strain between the GaN and InGaN layers. Highly-strained interfaces may result in relaxation and defect formation, which will degrade device performance. To assist in strain relief and improve crystal quality,

grading layers have been developed for the base-collector and base-emitter junctions [90,91]. These grading layers also serve to eliminate the effects of conduction band discontinuities at each heterojunction, decreasing current blocking at high-injection currents as shown by simulation in Figure 4.1.
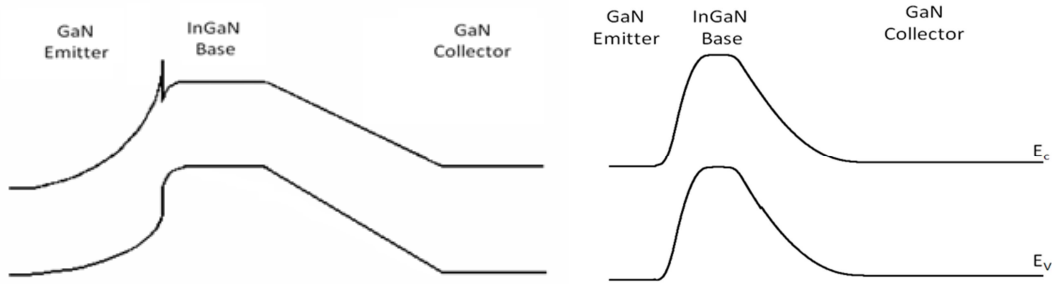


**Figure 4.1 1D simulation of HBT structure without grading layer (left) and with grading layer (right).**

To further explore the trade-off between InGaN composition and device performance, we have grown two $In_xGa_{1-x}N$/GaN HBT structures, with $x_{In}$ = 0.03 and 0.05. If we consider the band offset between the InGaN base and GaN layers, the HBTs with $p$-$In_{0.05}Ga_{0.95}N$ are expected to have an enhanced emitter-injection efficiency and show higher current gain than HBTs with $p$-$In_{0.03}Ga_{0.97}N$. This turns out not to be the case, as higher strain conditions and defect formation in the $In_{0.05}Ga_{0.95}N$ base compensate the advantages offered by higher indium content.

EpiPure$^{TM}$ trimethylgallium (TMGa, $Ga(CH_3)_3$), trimethylindium (TMIn, $In(CH_3)_3$), and high-purity ammonia ($NH_3$) were used as MOCVD precursors for GaN and InGaN, and silane ($SiH_4$) and bis-cyclopentadienylmagnesium (Cp$_2$Mg, $Mg(C_5H_5)_2$) were used as precursors for the $n$- and $p$-type dopants respectively. All structures were

grown on GaN templates which consist of a $c$-plane (0001) sapphire substrate, ~20 nm

low temperature ($T_g$ = 550 °C) GaN nucleation layer, and 2.5 μm high temperature ($T_g$ =

1050 °C), high-quality GaN buffer layer.  The layer structure of the HBTs developed for

this study is illustrated in Figure 4.2.  The only difference between the two structures is

the indium content of the base: one with $x_{In}$ = 0.03, the other with $x_{In}$ = 0.05 for

$In_xGa_{1-x}N$.  The collector and sub-collector for each sample were grown at 1065 °C.  The

3% InGaN base was grown at 850 °C, and the 5% InGaN base was grown using the same

TMIn flow rate but with reduced temperature, 825 °C, to achieve higher indium

incorporation. The base-collector (BC) graded junction was grown at the same

temperature as the base for each sample, with grading accomplished by ramping the

TMIn flow. The base-emitter (BE) grading layer was grown by ramping the TMIn flow

rate and temperature, from the base growth temperature to 950 °C, for both structures.

The emitters were grown at 950 °C which is well below the optimal growth temperature

for high-quality GaN (~1060 °C), but this reduced temperature is necessary in order to

prevent desorption of indium from the base during emitter growth. The indium

composition for each sample was confirmed with x-ray diffraction via an $\omega$-$2\theta$ scan.

Separate "base-only" samples were grown just up to - but not including - the base-emitter

grading layer in order to characterize the base material.

Device fabrication started with a two-step chlorine-based mesa etching in an

inductively-coupled plasma reactive-ion etching (ICP-RIE) system using $SiO_2$ etch masks

deposited via electron-beam evaporation.  The base layer was exposed by the first etching

step, with the second mesa etching stopping at the sub-collector layer.  After ICP etching,

these samples were treated in a diluted $KOH/K_2S_2O_8$ solution under ultraviolet

illumination to remove the dry-etching-induced surface damage [92]. The base contact consisted of a Ni/Ag/Pt metal stack, and was annealed at 500 °C. Even with reduced etch damage related to indium in the base and post-etch treatment, it should be noted that good ohmic contact to the base remains difficult to achieve. Ti/Al/Ti/Au metallization was used for the sub-collector and emitter contacts. Sub-collector contacts were annealed at 750° C. A top down scanning-electron microscope image of the final fabricated structure is shown in Figure 4.3.

| Layer | Material: doping | Thickness |
|---|---|---|
| Emitter | GaN:Si$^{++}$ | 70 nm |
| Base-Emitter Grading | In$_x$Ga$_{1-x}$N:Si $\rightarrow$ GaN:Si | 30 nm |
| Base | $p$-In$_x$Ga$_{1-x}$N:Mg | 100 nm |
| Base-Collector Grading | GaN:Si $\rightarrow$ In$_x$Ga$_{1-x}$N:Si | 30 nm |
| Collector | $n$-GaN:Si | 500 nm |
| Sub-Collector | $n$-GaN:Si+ | 1000 nm |
| Buffer | GaN:ud | 2.5 μm |
| Substrate | Sapphire | |

**Figure 4.2 Schematic of the epitaxial layer structure of the InGaN/GaN HBTs developed for this study. Two samples were created, one with $x_{In}$ = 0.03 the other with $x_{In}$ = 0.05.**
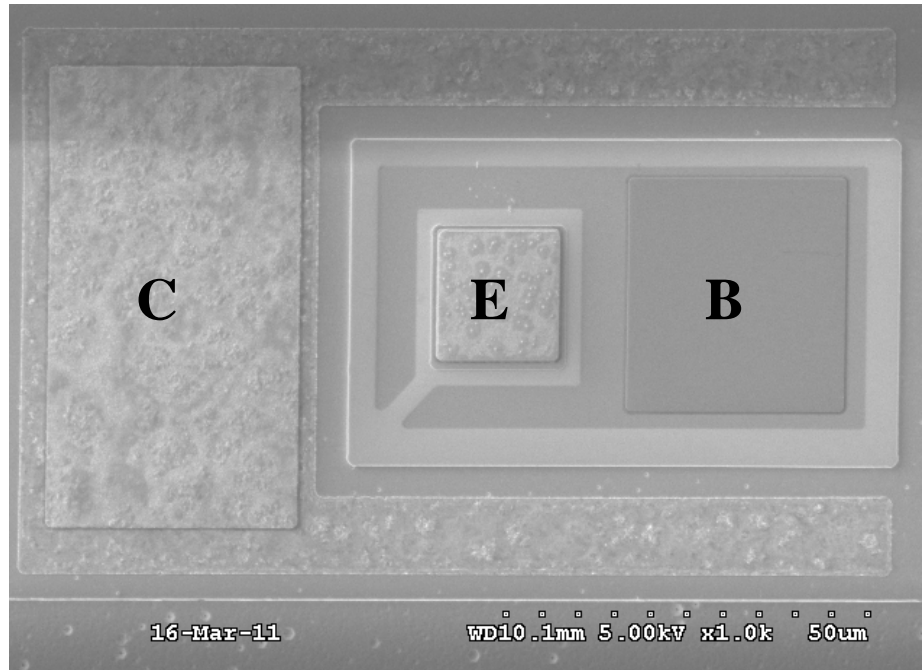
**Figure 4.3 A picture of the surface of the fully-fabricated HBT structure taken with a scanning-electron microscope. The collector, emitter, and based are labeled C, E and B respectively.**

The separate base-only samples, $x_{In} = 0.03$ and 0.05 for In$_x$Ga$_{1-x}$N, were grown and characterized first. Atomic-force microscopy scans of these samples, taken over $5 \times 5$ $\mu m^2$, are shown in Figure 4.4. A higher density of pits is observed for the sample with $x_{In} = 0.05$ in the base than $x_{In} = 0.03$. These pits are caused by the formation of V-defects, associated with threading dislocations and strain relaxation mechanisms, which are known to become more severe with higher indium content in terms of both density and size [93,94]. The presence of these pits is also reflected in the emitter surface morphology of the full structure, shown in Figure 4.5, with the $x_{In} = 0.03$ base sample showing a better surface morphology and lower root-mean square (RMS) surface roughness than the sample with $x_{In} = 0.05$ in the base. Since the emitter growth conditions are identical for the two structures, the reduction in emitter quality for the HBT with $x_{In} = 0.05$ in the base is attributed to the V-defects at the base-emitter interface which degrade the BE junction.
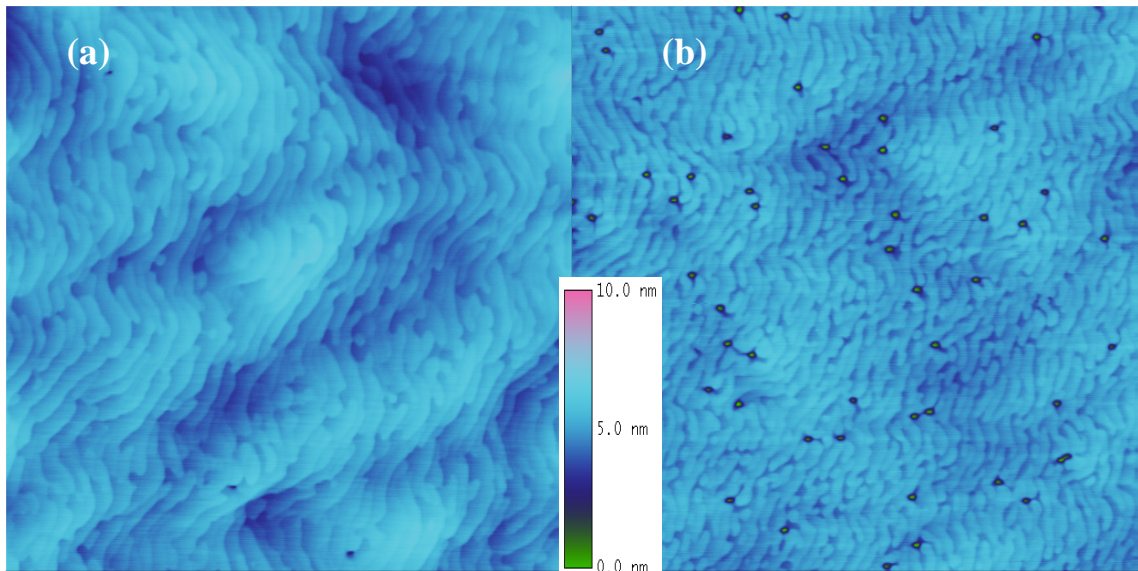
**Figure 4.4** 5×5 μm$^2$ AFM scans of the "base-only" samples with (a) $x_{In} = 0.03$ and (b) $x_{In} = 0.05$.
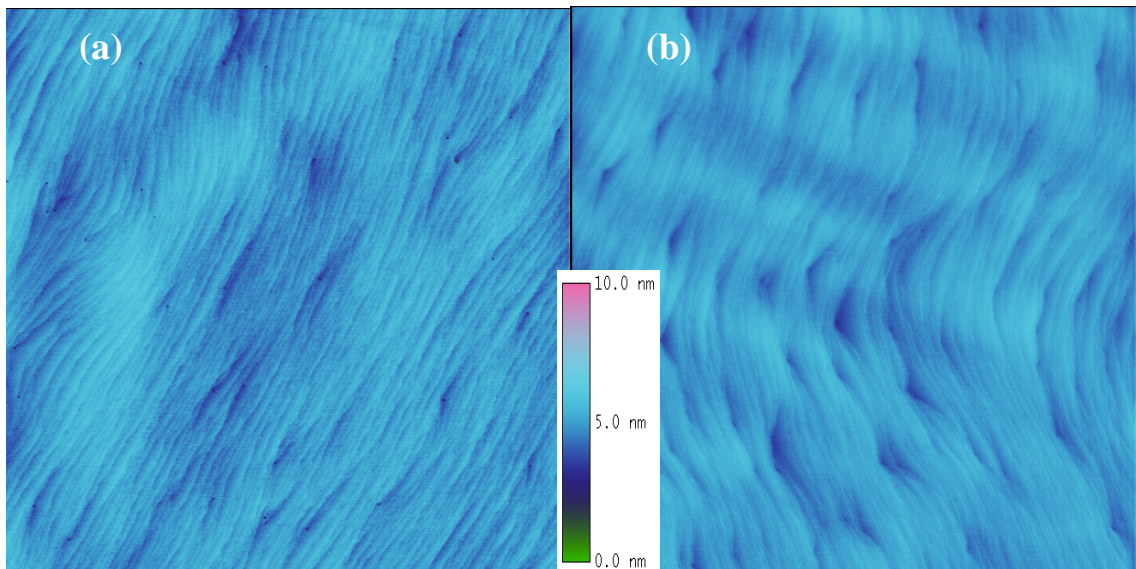


**Figure 4.5** 5×5 μm$^2$ AFM scans of the HBT emitter with (a) $x_{In} = 0.03$ and (b) $x_{In} = 0.05$.

Four-point van der Pauw patterns were deposited on both the base-only samples and full structures for electrical characterization of the bases and emitters of the HBTs. The sheet resistance was measured, and the mobility and bulk carrier concentrations were

determined via Hall-effect measurement. The results of these measurements are summarized in Table 4.1. As expected, the $x_{In} = 0.05$ base has lower resistance and increased carrier concentration because of its lower bandgap and improved doping efficiency over the base grown with $x_{In} = 0.03$. However, the material and crystalline qualities of the emitter and base of the $x_{In} = 0.03$ structure are superior to those of $x_{In} = 0.05$.

**Table 4.1 Electrical measurements of HBT base and emitter layers.**

| Sample | Sheet Resistance ($\Omega$/sq.) | Mobility ($cm^2$/Vs) | Carrier Concentration ($cm^{-3}$) |
|---|---|---|---|
| 3% Base | $9.6 \times 10^4$ | 6.5 | $+9.9 \times 10^{17}$ |
| 5% Base | $6.66 \times 10^4$ | 12 | $+1.1 \times 10^{18}$ |
| 3% Emitter | 1313 | 94.2 | $-7.0 \times 10^{18}$ |
| 5% Emitter | 1968 | 66.0 | $-6.6 \times 10^{18}$ |

Common-emitter *I-V* characteristics were measured at room temperature on fully fabricated HBTs with $20 \times 20$ $\mu m^2$ emitter areas and are shown in Figure 4.6. The $I_B$ steps were each 100 $\mu A$ to a maximum of 500 $\mu A$. The negative slope of the saturation region of the higher current curves is attributed to self-heating which typically sets in at collector currents higher than 10 mA, because of current crowding and the poor thermal conductivity of the sapphire substrate. The offset voltage and knee voltage of the $x_{In} = 0.05$ base device are 0.8 V and 10.8 V, respectively, while the device with $x_{In} = 0.03$ in

the base exhibits higher values of $V_{offset}$ = 1.8 V and $V_{knee}$ = 12.8 V. The lower offset and knee voltages imply that the $x_{In}$ = 0.05 structure has better base resistance than the $x_{In}$ = 0.03 structure, in agreement with the electrical characterization of the base only samples.
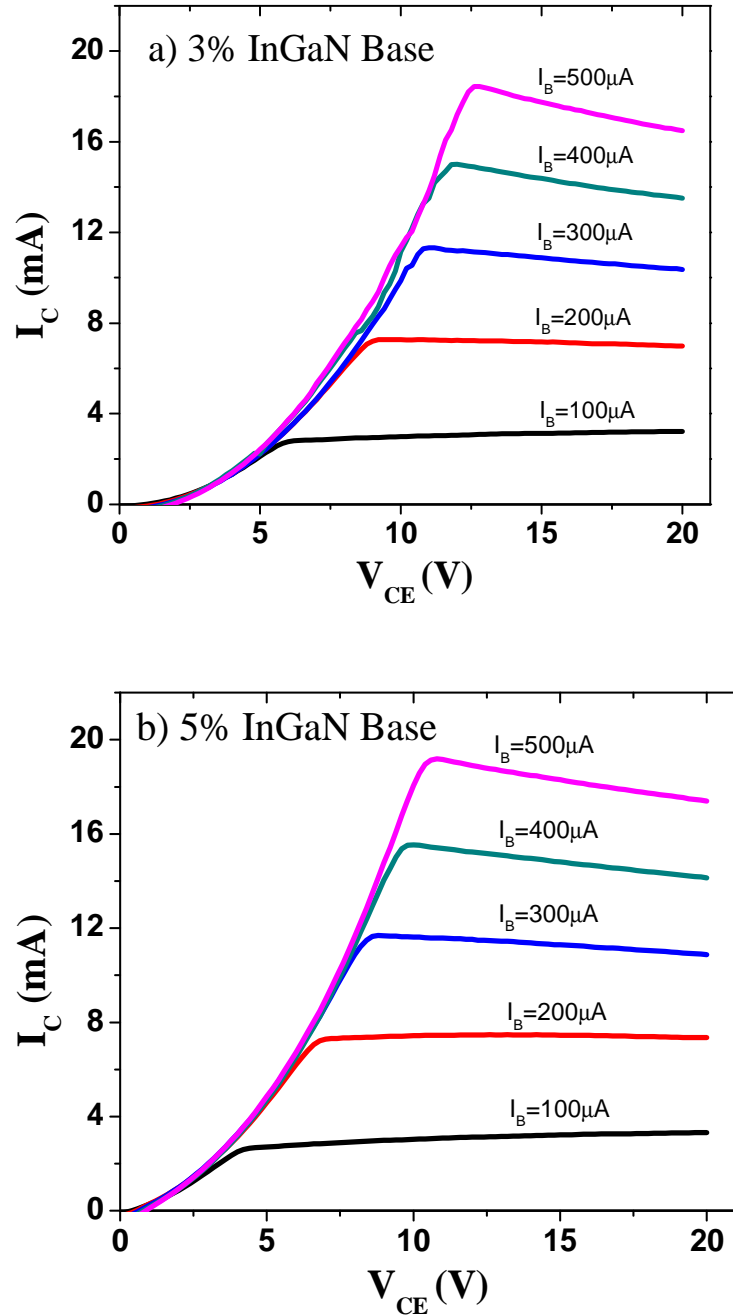


**Figure 4.6 Common-emitter *I-V* characteristics of the HBTs with (a) $x_{In}$ = 0.03 and (b) $x_{In}$ = 0.05 base compositions. The emitter area is 20×20 $\mu m^2$ for each device.**

The Gummel plot for each device at $V_{CB} = 0$ V is presented in Figure 4.7. The maximum differential gain ($h_{fe}$) and D.C. gain ($\beta$) for the $x_{In} = 0.03$ device are 47 and 38. The gains are nearly the same for the $x_{In} = 0.05$ device, with $h_{fe} = 44$ and $\beta = 37$. The common-emitter open-base breakdown voltage was also measured for each device with $BV_{CE0} = 110$ V and 55 V for $x_{In} = 0.03$ and 0.05 respectively. Thus the advantages that higher indium content offers to the base are compensated by a degraded base-emitter junction, and thus poor emitter injection efficiency, leading to the D.C. gains being nearly equal for both devices.

In summary, we have studied the effects of indium content in the InGaN base region of a InGaN/GaN HBT on device performance by growing two structures, one with $x_{In} = 0.03$ and the other with $x_{In} = 0.05$. As higher indium contents lead to lower bandgap, increased doping efficiency, and decreased sheet resistance, the performance of the HBT is also expected to improve. Accordingly, material characterization of the base revealed that $x_{In} = 0.05$ exhibits superior electrical characteristics, but inferior surface morphology resulting from the formation of V-defects. The lower offset and knee voltages observed in the common-emitter $I$-$V$ characteristics of the $x_{In} = 0.05$ InGaN device confirm the improvement in electrical properties of the base. However the D.C. gain for both the $x_{In} = 0.03$ and $x_{In} = 0.05$ structures was ~37. Thus we suggest that the more severe V-defect formation associated with higher base indium content leads to degraded emitter injection efficiency, and limits overall device performance. This trade-off between base electrical characteristics and emitter-base crystalline quality which depends on the indium content must be considered in further development of InGaN/GaN HBTs, aiming for the

development of HBT structures that can satisfy both improved electrical properties of the

base layer and improved crystalline quality of emitter and base with large band offsets.
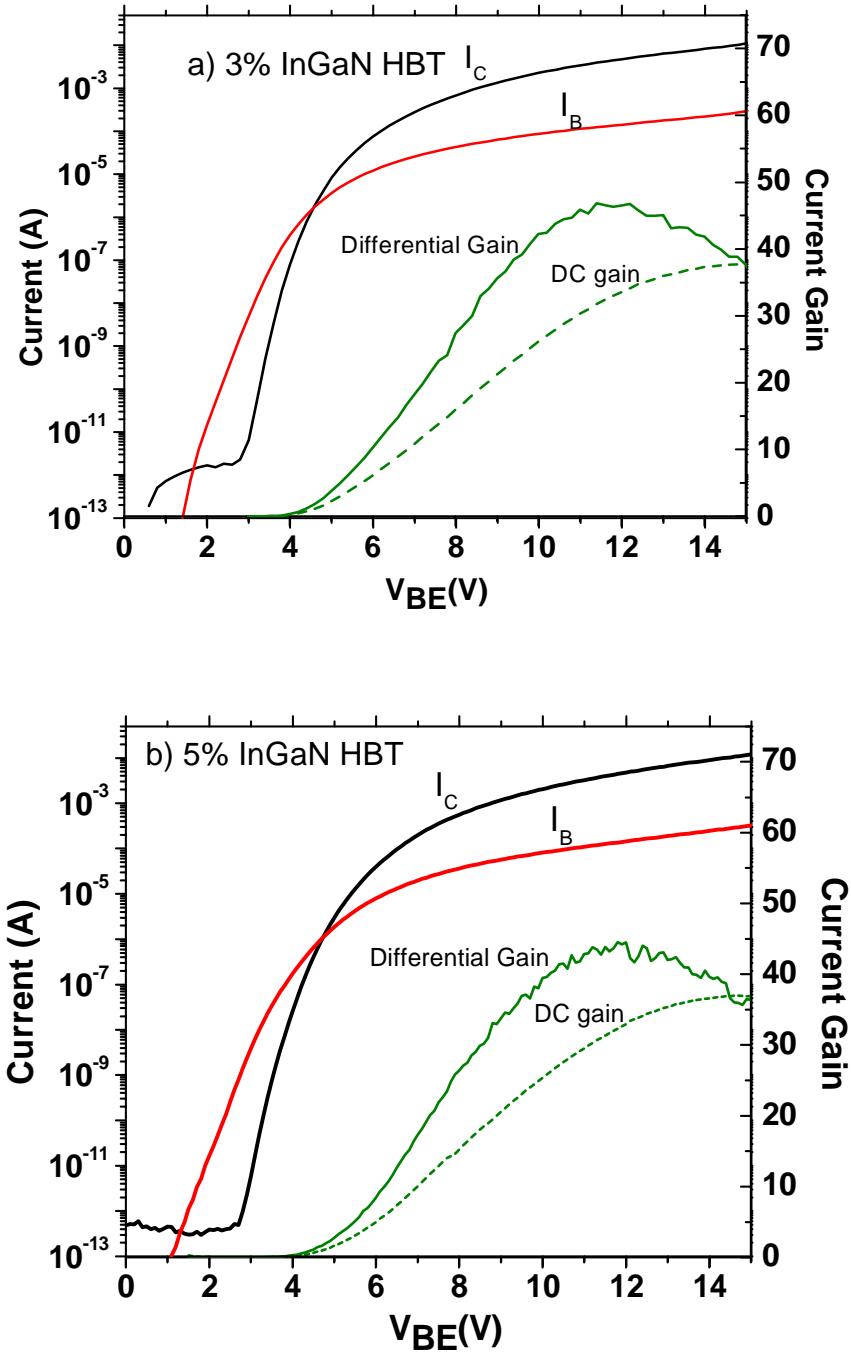


**Figure 4.7 Gummel plots of the HBTs with (a) $x_{In} = 0.03$ and (b) $x_{In} = 0.05$ base compositions.**

## 4.2 High Power Operation of GaN/In$_x$Ga$_{1-x}$N Heterojunction Bipolar Transistors on Free-Standing GaN Substrates

In order to address technical challenges in materials and device fabrication, expecially for the improvement in contact and bulk resistance of the base layer, HBTs employing a GaN/InGaN heterojunction structure on sapphire and SiC substrates have been developed to achieve improvements in current gain and output power [95]. One significant drawback is still a high density of threading dislocations (on the order of $10^8$~$10^9$ cm$^{-2}$) in the HBT epitaxial structures originating from the strained heteroepitaxial growth on foreign substrates with lattice and thermal mismatches [3]. While this rather high dislocation density does not prevent III-nitride devices from working, it limits their full potential, as these defects act as current leakage paths and carrier traps, reducing the current handling characteristics of electronic devices [96,97]. These problems are believed to be even worse for the HBTs than HFETs, as the operation of HBTs dominantly relies on carrier transport by diffusion of minority carriers.

For this work we have employed a free-standing GaN (FS-GaN) substrate for homoepitaxial growth of the collector layer. The removal of the low-temperature buffer layer ensures a reduced defect density throught the crystal structure, limited by the inherent quality of the substrate. In this case, the dislocation density is reduced from $10^9$ cm$^{-2}$ on sapphire to $10^6$ cm$^{-2}$ on FS-GaN. This reduced dislocation density may further benefit the performance characteristics for HBTs with an InGaN base layer. For InGaN/GaN devices, reduced dislocation density can suppress the formation of V-defects around dislocations [94] and indium (In)-rich quantum-dot (QD) like localized states, which are not found in AlGaN/GaN-based devices. In the present study, we have grown

and fabricated *NpN* GaN/InGaN/GaN HBTs on a FS-GaN substrate which have several advantages over their AlGaN/GaN counterparts, such as lower acceptor activation energy for *p*-type InGaN and high mobility of electrons. One caveat to this design is the non-ideal base contact formation: type conversion occurs at the surface of *p*-type III-nitride material as a result of dry etching damage, inhibiting the formation of an ohmic contact. However, one further advantage of using InGaN as the base material is resistance to this effect with the addition of indium as reported by Makimoto et al. [96]. Thus, while the *p*-In$_{0.03}$Ga$_{0.97}$N base contact in this study still exhibits a non-ohmic characteristic on etched *p*-type surface, the inclusion of indium allows improved current delivery through the contact as compared to *p*-GaN. We have also investigated the effect of threading dislocations on the current gain and diffusion length of minority carriers for a comparative study of HBTs on FS-GaN and sapphire substrates.

The epitaxial layer and device structure for the HBTs in this study is shown in Figure 4.8. They are virtually the same as the devices described in the previous section save for the substrate which now includes FS-GaN, and the base composition which has been set at $x_{In} = 0.03$. Both structures were grown in a single growth run—utilizing no additional re-growth—by MOCVD. Common-emitter *I-V* characteristics measured at room temperature for the 20×20 μm$^2$ devices on both substrates are shown in Figure 4.9. Both maximum collector current and gain are substantially higher for the device on FS-GaN, with a maximum collector current density ($J_C$) of 12.3 kA/cm$^2$ versus 1.81 kA/cm$^2$ for the device on sapphire. This improvement in current gain and collector current density for high-power operations is attributed to (1) the superior thermal conductivity of FS-GaN compared to that of sapphire substrates and to (2) the improvement in material

quality of HBT epitaxial structures on FS-GaN, including not only reduced threading-dislocation density, but also possible mitigation of microscopic localized states formation, which will be discussed in further detail.
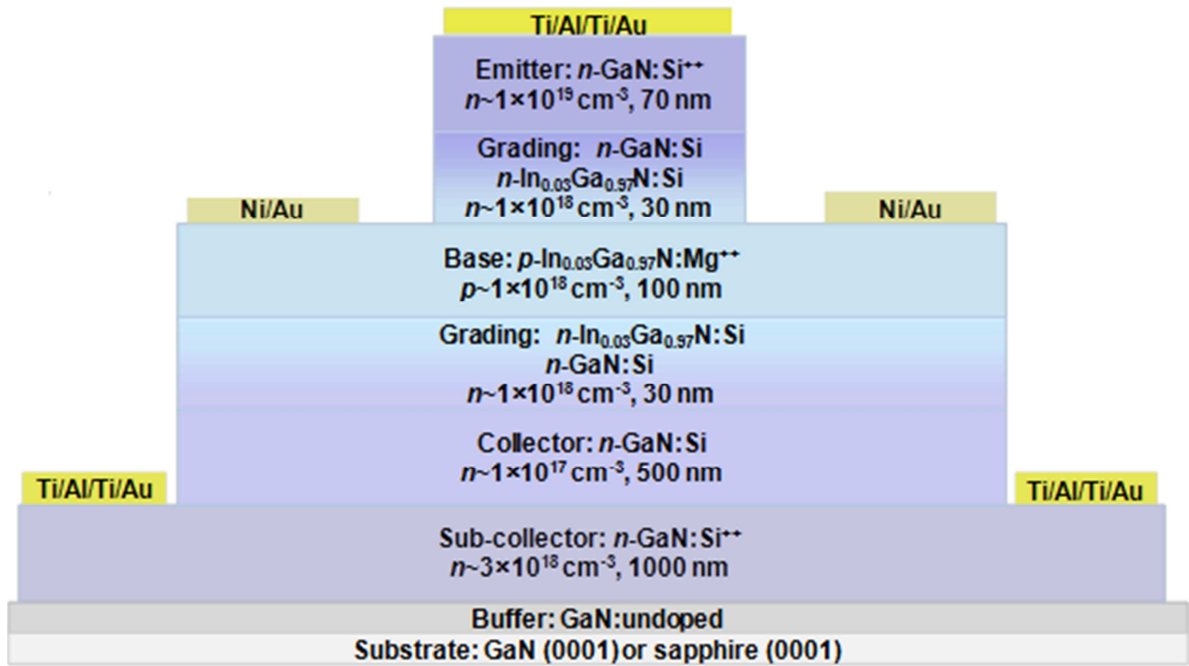


**Figure 4.8 Schematic illustration of epitaxial layer and device structure of *NpN* GaN/InGaN heterojunction bipolar transistors in this study.**
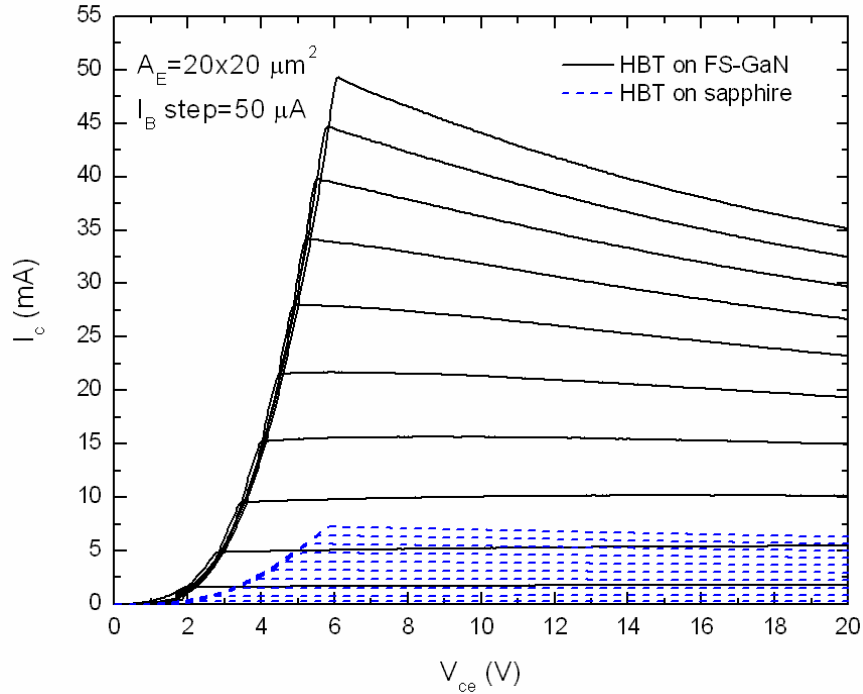
**Figure 4.9 Common-emitter *I-V* characteristics of HBTs with $A_E$ = 20×20 µm² grown on FS-GaN and sapphire substrates.**

The Gummel plot for these devices at $V_{CB} = 0$ V is shown in Figure 4.10. The advantages of FS-GaN over sapphire for HBTs are again made clear by the significant improvement in both D.C. gain ($\beta = I_C / I_B$) and differential gain ($h_{fe} = \delta I_C / \delta I_B$). D.C. and differential gain are 70 and 113 for the featured device on FS-GaN, while only 19 and 21 for the device on sapphire at $J_C = 2.7$ kA/cm², the level of current density at which the peak current gain for the sapphire device is reached. The maximum values of $\beta$ and $h_{fe}$ for the device on FS-GaN are 90 and 120, respectively.
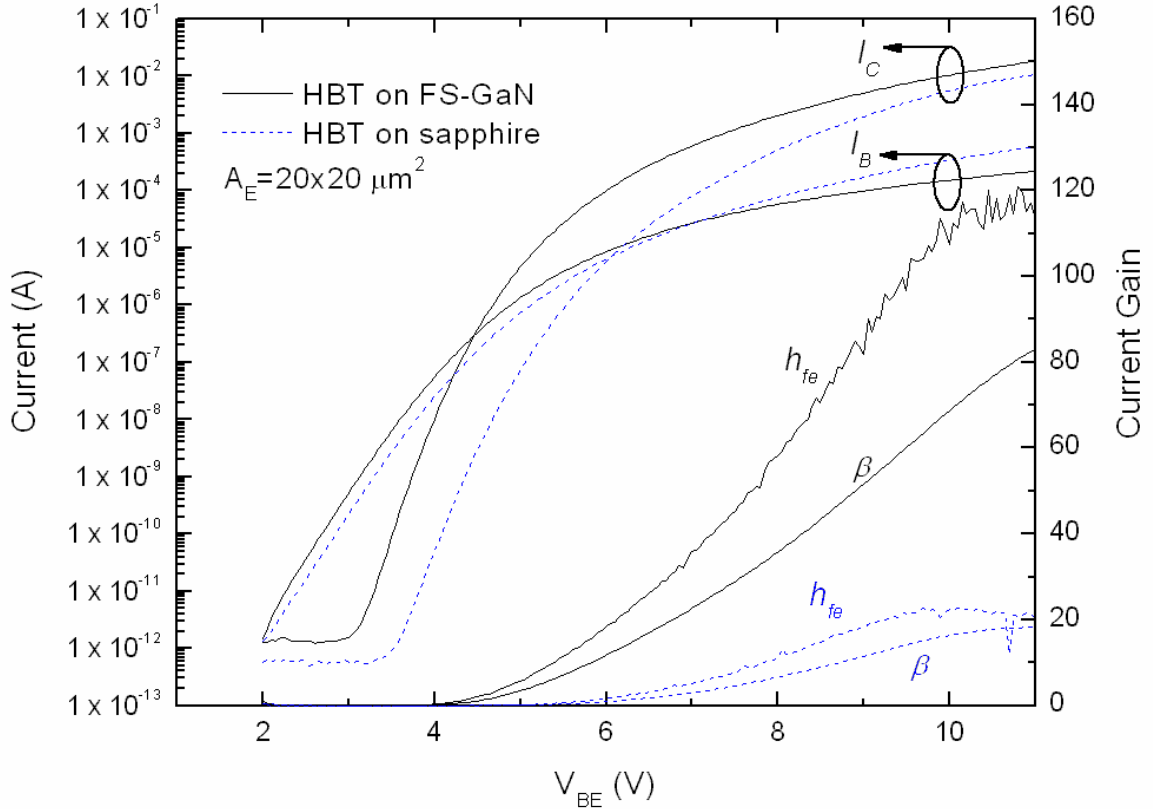
**Figure 4.10 Gummel plot at $V_{CB}$ = 0 V of HBTs with $A_E$ = 20×20 μm² grown on FS-GaN and sapphire substrates.**

In the case of the HBT epitaxial structure grown on FS-GaN substrates, the density of threading dislocations was estimated to be ~4×10⁶ cm⁻² based upon the dislocation density of the substrate. This value is significantly lower by several orders of magnitude than the typical value in the range of ~5×10⁸ cm⁻² to ~1×10⁹ cm⁻² for the HBTs grown on sapphire substrates. This reduced threading-dislocation density is critical to the material quality and structure of HBTs, particularly to the base region which predominately determines the device performance characteristics. First, in InGaN/GaN heterostructures, V-defects associated with threading dislocations are prone to form depending on the In mole fraction, thickness, and the accumulated strain energy. These V-defects can play a role as paths of leakage current at the *p*-InGaN/*n*-GaN BE junction,

as verified in other *p-n* junction structures [98]. However, with the design considerations we have employed in this structure, specifically a $p$-$In_{0.03}Ga_{0.97}N$ base layer with compositional grading in base-emitter (BE) and base-collector (BC) junctions, V-defects are not expected to form. Therefore, we can investigate the effect of threading dislocations without the influence of V-defects in this structure. When carriers recombine at crystalline defects (mainly threading dislocations in this study) the resulting recombination current detracts from the net gain of the device. The bulk recombination current ($J_{Bulk}$) consists of the BE reverse-injection current, defect-assisted base recombination and BE space-charge recombination. It can be derived from the normalized collector-current density ($J_c/\beta$) via the following equation [99]:

$$\frac{J_C}{\beta} = J_{Bulk} + K_{B,surface} \times \frac{L_E}{A_E},$$

(4.1)

where $K_{B,surface}$ is the perimeter dependent surface-recombination current (from surface states and contact losses), $L_E$ is the emitter perimeter, and $A_E$ is the emitter area. By plotting the normalized current density over several values of $L_E/A_E$ for several different devices, $J_{Bulk}$ is determined.

Figure 4.11 shows this data plotted for several values of $J_C$ for the HBT on FS-GaN substrate. At collector currents of 0.5, 5, and 50 A/cm$^2$, the bulk recombination currents were found to be 0.01, 0.18, and 1.23 A/cm$^2$ respectively. As a comparison to HBTs on a sapphire substrate, values for $J_{Bulk}$ have been previously reported as 0.25, 0.8, and 3.3 A/cm$^2$ for collector currents of 0.5, 5 and 50 A/cm$^2$ [100]. Thus the reduction in dislocation density plays a significant role in reducing parasitic bulk recombination

currents in the base, particularly at lower current densities where defects play a dominant role in performance limitation. At higher current densities, current crowding becomes the dominant limiting factor. In an analogous derivation, the minority carrier diffusion length ($L_n$) also exhibits a dependence on dislocation density, and can be obtained via the equation:

$$\beta = \frac{2L_n^{\ 2}}{W_B^{\ 2}}, \qquad (4.2)$$

where $W_B$ is the base width, assuming that the emitter efficiency is unity and that $L_n \gg W_B$. $L_n$ is calculated to be 308 nm for the HBT on sapphire shown in this study, and 670 nm for the HBT on FS-GaN, representing a ~118% improvement, which is significantly is higher than ~31% improvement for diffusion length of holes (*i.e.*, $L_h$=150→196 nm) in AlGaN/GaN HBTs on GaN [32].
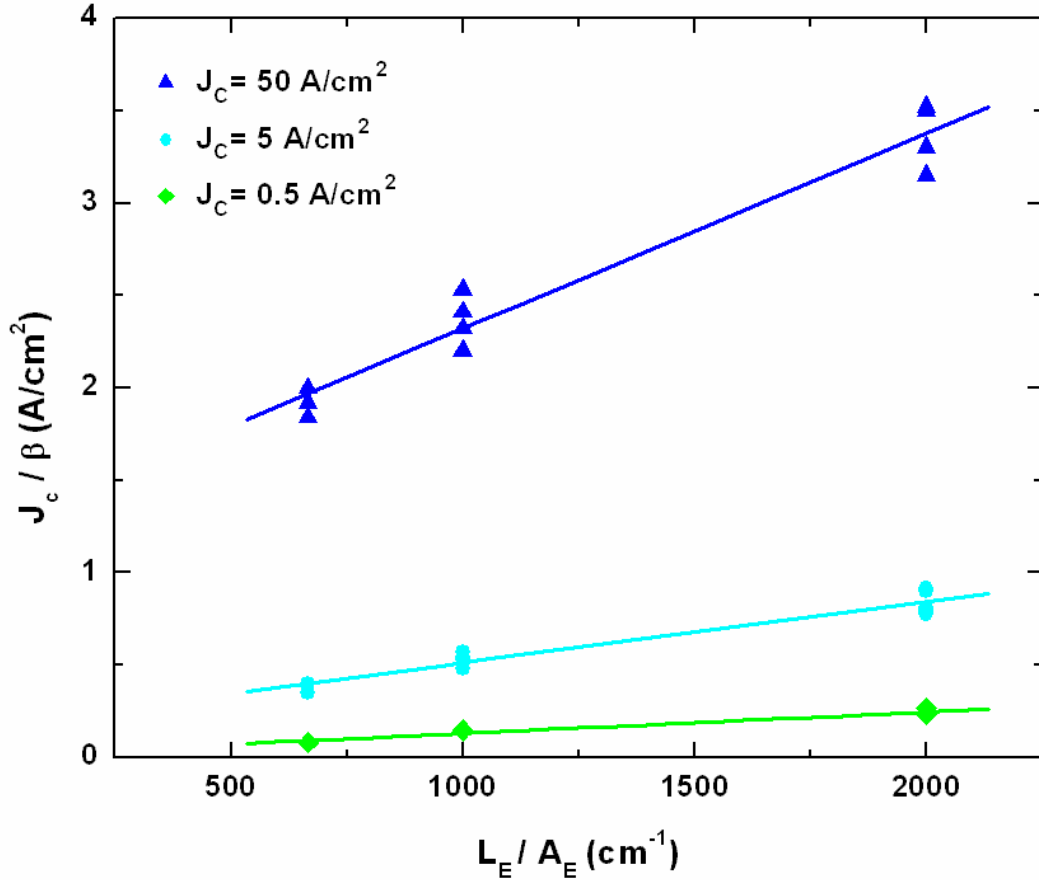
**Figure 4.11 Plot of normalized collector-current density ($J_c/\beta$) versus perimeter-to-area ratio ($L_E/A_E$) for HBTs on a FS-GaN substrate.**

Setting aside the difference between electrons and holes, such dramatic improvement may imply that, in addition to the direct effect of reducing dislocations, the diffusion length of minority carriers can be further improved for HBT structures containing an InGaN base. For the InGaN/GaN HBTs on both FS-GaN and sapphire substrates, *macroscopic* phase separation governed by thermodynamic equilibrium is believed to be the same; however, the formation of *microscopic* QD-like In-rich InGaN embedded in the $In_{0.03}Ga_{0.97}N$ base might be different between substrates. On the (0001) surface of growing InGaN, In will preferentially bind at the edges and interior of the surface structures [101], and thereby leading to an inhomogeneous In distribution near

crystalline defects with high energy sites. Experimental observation also confirms that the enhanced formation of In-rich QDs on high energy sites via intentional surface roughening [102]. This different behavior of QD-like localized states is believed to also be important, resulting in promoted/mitigated trapping of injected minority carriers in the base layer affecting their diffusion length. For the GaN/InGaN/GaN HBTs on FS-GaN in this study, reduction in QD-like localized states as well as threading-dislocation density may contribute to the significantly improved diffusion length of minority carriers.

### 4.2.1 Ultra-High Power HBT on FS-GaN Substrate

To further push the limits of high-power operation, small-area $3\times3$ $\mu m^2$ HBTs were fabricated from the HBT structure on FS-GaN substrate. This would enable us to achieve a higher power density at testable currents as long as our device did not break down. Figure 4.12 demonstrates the *I-V* characteristics of this device reaching a maximum current density of $J_c = 141$ kA/cm$^2$ at a base current of 400 $\mu A$. At this point, self-heating effects started to kick in, reducing the collector current at higher voltages. However, a maximum power density of 3.05 MW/cm$^2$ was achieved before breakdown. This performance is attributed to the reduction in heat-generating defects as well as the enhanced thermal conductivity of FS-GaN as compared to sapphire.
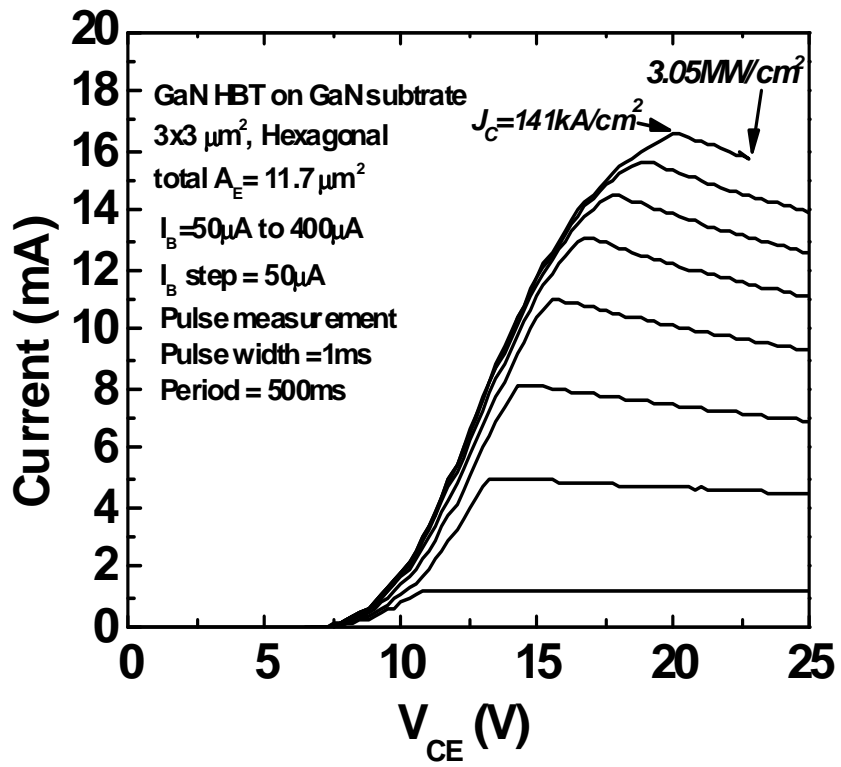
**Figure 4.12** *I-V* characteristics of a small area, ultra-high power HBT on FS-GaN substrate.

# CHAPTER 5

# III-NITRIDE DEEP-ULTRAVIOLET LIGHT EMITTERS

## 5.1 Heteroepitaxy vs. Homoepitaxy for Semiconductor UV Emitters

A major technical obstacle to the realization of stimulated emission in the deep-ultraviolet (DUV) region of the electro-magnetic spectrum from a semiconductor crystal is the high defect density found in heteroepitaxially grown III-nitride materials. As described in the introduction, these defect sites act as non-radiative recombination centers, which inhibit stimulated emission by increasing the threshold for population inversion.

A solution to this problem is provided by the recent advent of native AlN substrates. Prepared from high-quality bulk crystals, these substrates enable homoepitaxial growth of AlN buffer layers [103], leading to a reduced threading dislocation density in the subsequent $Al_xGa_{1-x}N$ MQW active region. The elimination of thermal mismatch between the substrate and epitaxial layers also enhances the growth and performance of the device by eliminating cracks that form during the thermal cycle and cool-down. There have been a handful of reports of successful growth on native-AlN substrates for both electrically and optically pumped UV devices [76,104], but efficiencies remain low and thus continued development is underway for better performance at shorter wavelengths.

In this study, we have used 500 μm thick aluminum-polar (0001) native AlN substrates cut from a boule grown by physical vapor transport. Prior to growth, the AlN

substrates were prepared in a 3:1 $H_2SO_4$ :$H_3PO_4$ solution at 90º C to remove the native surface oxide [103]. The epitaxial structure was grown in an AIXTRON 6×2" metalorganic chemical vapor deposition (MOCVD) reactor with close-coupled showerhead. An *in-situ* high-temperature ammonia treatment was then used to further etch the oxide to enable efficient AlN growth. Another difficulty encountered in the growth of high aluminum content structures is the low ad-atom mobility of aluminum compared to gallium. Thus, a high temperature and low V/III ratio (relative to GaN growth) must be carefully calibrated in order to promote smooth, two-dimensional AlN and AlGaN growth [105,106]. Here we have used a temperature of 1155º C and a V/III ratio of less than 100 for the AlN buffer and ~400 for all subsequent ternary layers. The ideal temperature range for such a structure is above 1200º C, however inherent limitations in the reactor design, particularly the tolerance level of the heater, prevent us from achieving such a high growth temperature without risking damage to the reactor.

Using these growth parameters as a basic template, we have grown several structures on AlN substrates to probe the lower reaches of the DUV spectrum. The first is a complex structure developed to examine the effects of *n*-cladding and contact layers on the material quality of a DUV active region. Top layers such as an electron blocking layer, *p*-cladding, and *p*-contact layers were purposefully emitted so that an excitation laser could penetrate to the active region for a photoluminescence measurement. The second and third structures were specifically optimized for optical pumping studies: they are significantly simpler containing a multi-quantum-well active region with AlN cladding layers. Thus the material quality of the active region would not be adversely

affected by the underlying *n*-layers, which should theoretically yield a reduced dislocation formation and a lower lasing threshold power density.

## 5.2 Lasing at 257 nm from ½ Laser Diode Structure on AlN Substrate

The structure examined in this study is a ½ laser diode designed specifically for optical pumping. For future studies, further expansion of the structure into an electrical injection design is possible with the addition of *p*-type layers. The structure began with a 200 nm homoepitaxial AlN buffer layer, followed by two strain-reducing superlattices consisting of 50 periods of $Al_{0.66}Ga_{0.34}N$/AlN (2 / 2 nm) and 50 periods of $Al_{0.55}Ga_{0.45}N$/$Al_{0.66}Ga_{0.34}N$ (2 / 2 nm). These layers are deemed necessary to provide a gradient of lattice constant between the AlN buffer and the following 500 nm thick, low aluminum content $Al_{0.55}Ga_{0.45}N$:Si *n*-type contact layer. This contact layer is a crucial design aspect of a DUV laser diode as it must be of low enough aluminum composition to accommodate efficient electron injection, yet have a higher aluminum composition than the active region so as not to absorb emitted photons. Following the contact layer is an 800 nm graded layer (from $Al_{0.55}Ga_{0.45}N$ to $Al_{0.80}Ga_{0.20}N$) that acts as *n*-type cladding, enhancing the optical field of the active region, albeit at the expense of electron injection into the MQWs. This trade-off between optical confinement and electrical conductivity must be carefully balanced, thus our decision to use compositional grading to reduce the energy barrier to current flow created by a more abrupt conduction band discontinuity. The grading layers also serve to enhance the carrier wavefunction overlap in the active region by distributing the interface polarization charge present at the heterojunctions. The $Al_{0.80}Ga_{0.20}N$ cladding is then linearly graded down to the composition of the

quantum barrier, followed by a three period $Al_{0.66}Ga_{0.34}N/Al_{0.53}Ga0_{.47}N$ (5 / 2.8 nm) MQW active region and 12 nm $Al_{0.66}Ga_{0.34}N$ cap.

| |
|---|
| **12 nm Spacer $Al_{0.66}Ga_{0.34}N$** |
| **Active region $Al_{0.535}Ga_{0.465}N/Al_{0.66}Ga_{0.34}N$ (2.8/5.5 nm) x3 MQWs** |
| **435 nm inner cladding 80→66% graded $Al_xGa_{1-x}N$:Si** |
| **300 nm inner cladding 55→80% graded $Al_xGa_{1-x}N$:Si** |
| **30 nm *n*-contact layer $Al_{0.55}Ga_{0.45}N$:Si-** |
| **570 nm *n*-contact layer $Al_{0.55}Ga_{0.45}N$:Si+** |
| **Buffer 2 nm $Al_{0.66}Ga_{0.34}N$ / 2 nm $Al_{0.55}Ga_{0.45}N$ x25** |
| **Buffer 2 nm AlN / 2 nm $Al_{0.66}Ga_{0.34}N$ x25** |
| **Regrowth interface** |
| **AlN template on Sapphire/Hexatech AlN sub** |

**Figure 5.1 Cross-section schematic of the DUV AlGaN MQW laser structure with *n*-contact and cladding layers**

The reciprocal-space mapping (RSM) of this structure taken with high-resolution x-ray diffraction (XRD) is shown in Figure 5.2. Even with the wide compositional variation and thick layers, the RSM shows the entire structure to be pseudomorphically grown to the AlN substrate. A cross-section of the structure taken with transmission-electron microscopy (TEM) is shown in Figure 5.3; an image of the same device grown on sapphire substrate with additional low-temperature buffer layer is also presented for comparison. Threading dislocations are readily seen in high density in the sapphire based sample, but nearly non-existent for the structure grown on AlN substrate. That is not to

say these structures are perfect crystals, but only that the defect density is significantly

reduced to an extent where stimulated emission becomes possible below 300 nm.
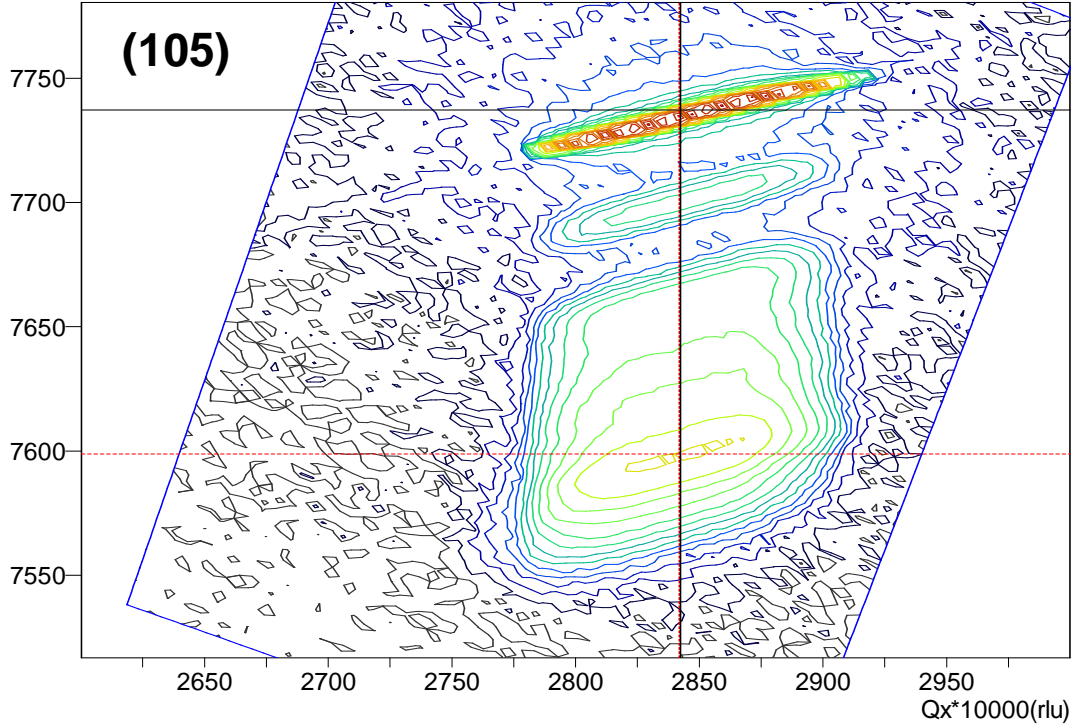


**Figure 5.2 X-ray diffraction reciprocal-space mapping of the optically pumped structure on AlN substrate demonstrating pseudomorphic growth.**
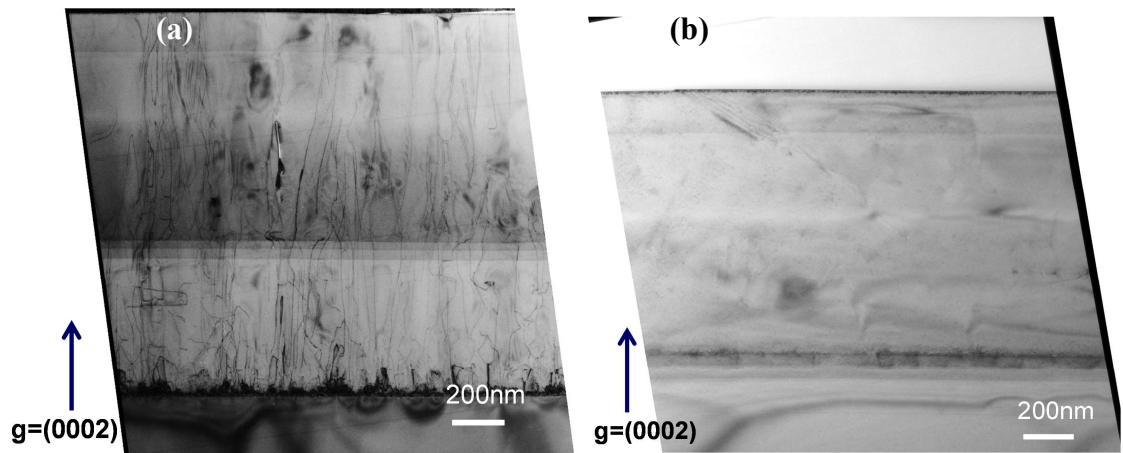


**Figure 5.3 Transmission-electron microscopy cross-section of identical structures on (a) sapphire and (b) AlN substrate.**

An atomic-force microscopy measurement for the surface of the epitaxial structure grown on the AlN substrate is shown in Figure 5.4. While the surface morphology exhibits a large amount of inhomogeneity, step flow morphology is clearly seen at higher magnifications. The inhomogeneity is due to the very low adatom mobility of aluminum compared to gallium, particularly at temperatures below 1200º C. This low aluminum adatom mobility results in localized areas of 2D growth separated by grain boundaries. These grain boundaries inhibit stimulated emission and push the lasing thresholds higher.

Following growth, the samples were thinned from the backside down to 50 μm via a chemical-mechanical lapping process to enhance confinement of the optical field within the sample. The pieces were then cleaved into laser bars of various sizes with widths ranging from 100 to 500 μm and lengths all in the range of 50 mm. The lengths of the bars are perpendicular to the *m*-cleavage plane and widths lie along the *a*-plane.
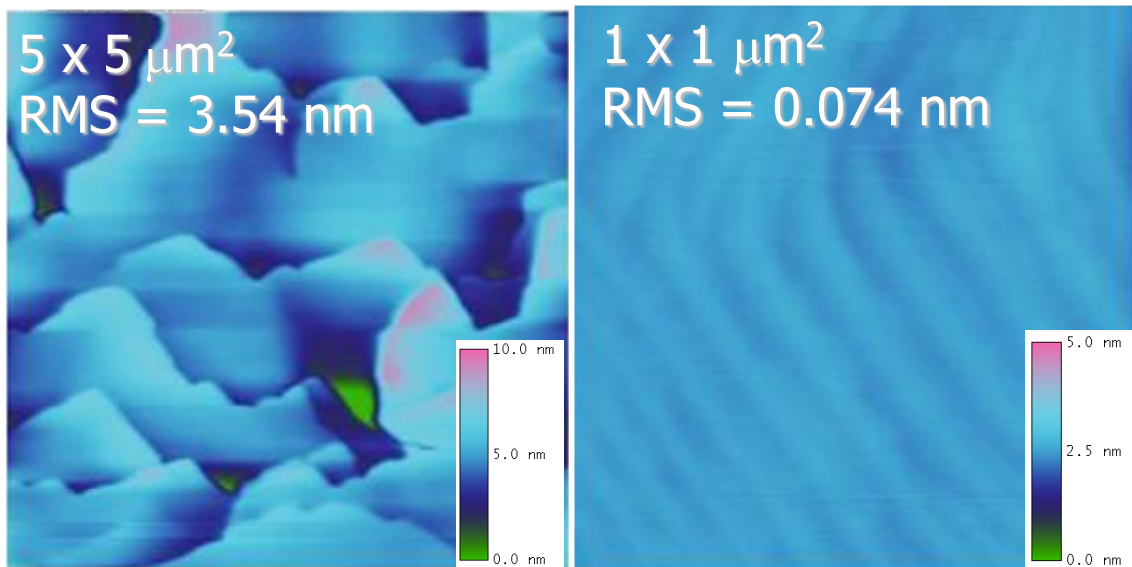


**Figure 5.4 Atomic-force microscopy surface scans of the structure on AlN substrate.**

The samples were then optically pumped with a 248 nm, 20 mW KrF laser to produce stimulated emission at room temperature. The sample emission spectrum is shown in Figure 5.5, lasing at a wavelength of 257 nm with a measured full-width half maximum of less than 2 nm. The maximum excitation power density is 4.9 MW/cm$^2$.
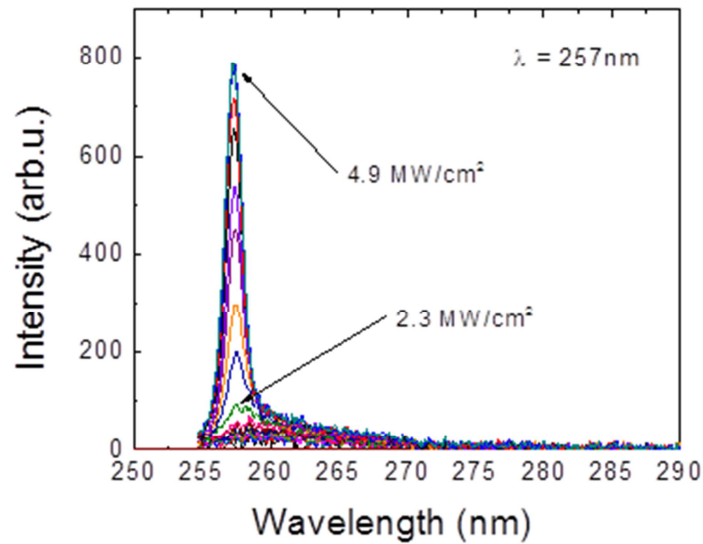


**Figure 5.5 Emission spectra at various excitation densities demonstrating lasing at 257 nm.**

The optical output power as a function of excitation density is shown in Figure 5.6, demonstrating lasing with a pump power threshold density of 1.88 MW/cm$^2$. While this is higher than threshold densities reported elsewhere [76], it is to be expected at lower wavelengths in higher aluminum content structures because of the higher bandgap energies, reduced carrier mobility, and enhanced defect related non-radiative recombination. However, we believe this threshold power density can be significantly reduced with further optimization of cladding layers and the addition of distributed Bragg

reflectors to improve the optical confinement of the structure so that the optical gain profile lies more squarely within the active region.
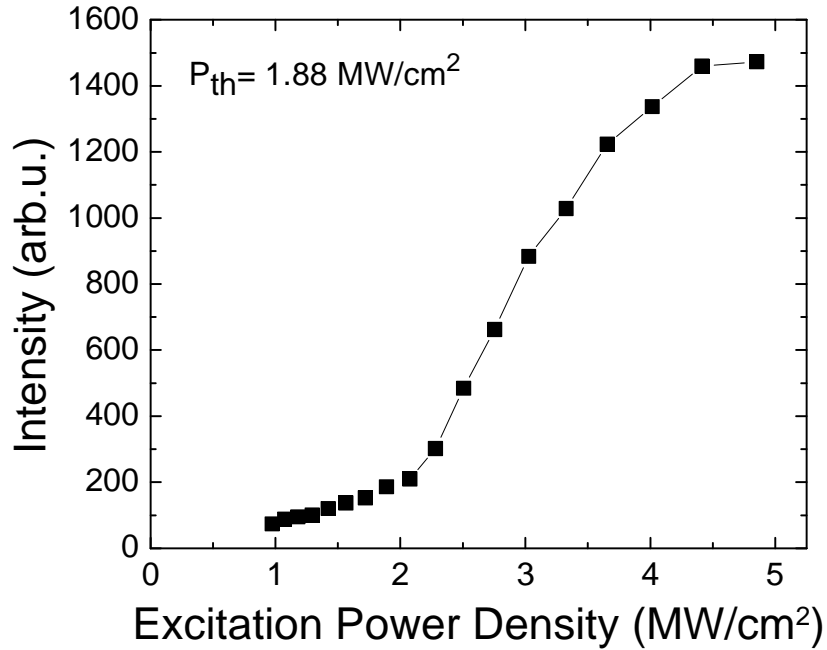


**Figure 5.6 Optical output intensity as a function of excitation power density.**

In summary, we have grown and fabricated an ultraviolet laser on AlN substrate and demonstrated stimulated emission via optical pumping. The elimination of thermal mismatch reduction in the strain state between the substrate and the AlN buffer layer yielded reduced defect formation compared to conventional substrates such as sapphire or SiC, thus enabling laser action at lower thresholds. The epitaxial design includes a full n-cladding layer for future expansion into a full-diode design with anticipated electrical injection. The development of high conductivity, high aluminum containing p-type $Al_xGa_{1-x}N$ will be crucial to this venture and it is critical to have an appropriate active region capable of lasing as demonstrated in this study.

## 5.3 Low-Threshold Lasing Below 250 nm from Optically Pumped AlGaN Structures on AlN Substrates

The epitaxial structure designed for this study, illustrated in Figure 5.7 was specifically optimized for optical pumping experiments. The active region consists of a 10 x MQW structure, with 3 nm $Al_{0.60}Ga_{0.40}N$ wells and 5 nm $Al_{0.75}Ga_{0.25}N$ barriers, between a 200 nm AlN regrowth buffer layer and a 10 nm AlN cap layer for surface passivation. The thickness of the cap layer was determined by the absorption coefficient of the material at the desired excitation wavelength so as to maximize the absorption within the active region. The omission of any underlying AlGaN layers for the purpose of strain reduction serves to enhance the confinement of the optical field within the active region. Even without such strain-engineered layers, high crystal-quality was still maintained.



| 10 nm AlN cap |
| $10\times Al_{0.60}Ga_{0.40}N/Al_{0.75}Ga_{0.25}N$ MQWs |
| 200 nm AlN Regrowth |
| (0001) AlN Substrate |
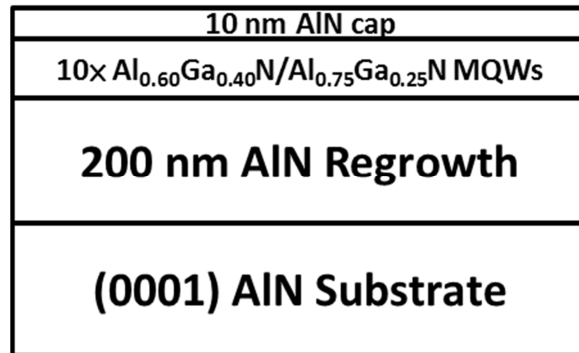
**Figure 5.7 Cross-section schematic of the DUV AlGaN MQW laser structure specifically optimized for optical pumping experiments.**

The surface morphology of the structure was measured by atomic-force microscopy illustrated in Figure 5.8. The RMS roughness is 0.87 nm, 0.90 nm and 0.91

nm for 5×5 μm², 10×10 μm², and 20×20 μm² measurements, respectively, indicating a relatively smooth surface with low defect density. Figure 5.9 shows the asymmetric (105) reciprocal space mapping (RSM) of the epitaxial structure taken by high-resolution triple-axis x-ray diffraction. The horizontal position of the AlN peak and that of the AlGaN/AlGaN active region indicate that the epitaxial grown layers are fully strained to the substrate, inhibiting the formation of defects such as cracks and dislocation associated with lattice relaxation.
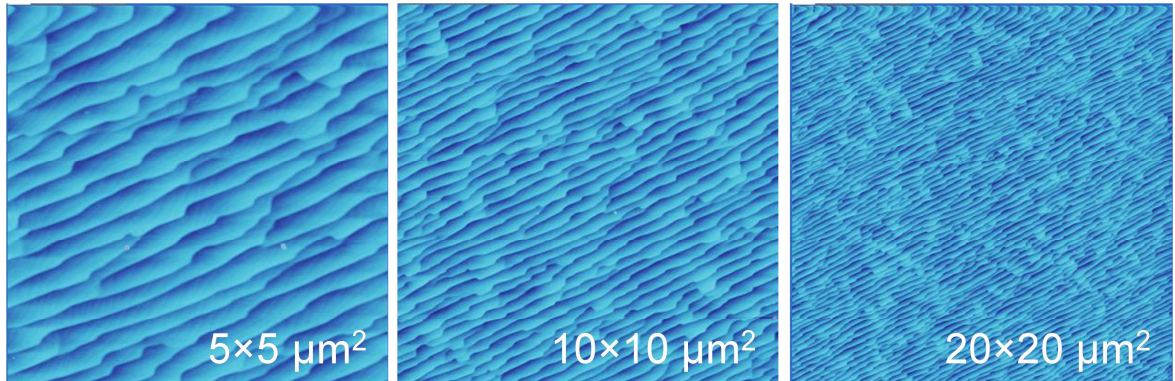


**Figure 5.8 Atomic-force microscopy measurements taken at 5×5, 10×10, and 20×20 μm² with RMS roughness values of 0.87, 0.90, and 0.91 nm respectively. The Z-height for all scans was 15 nm.**
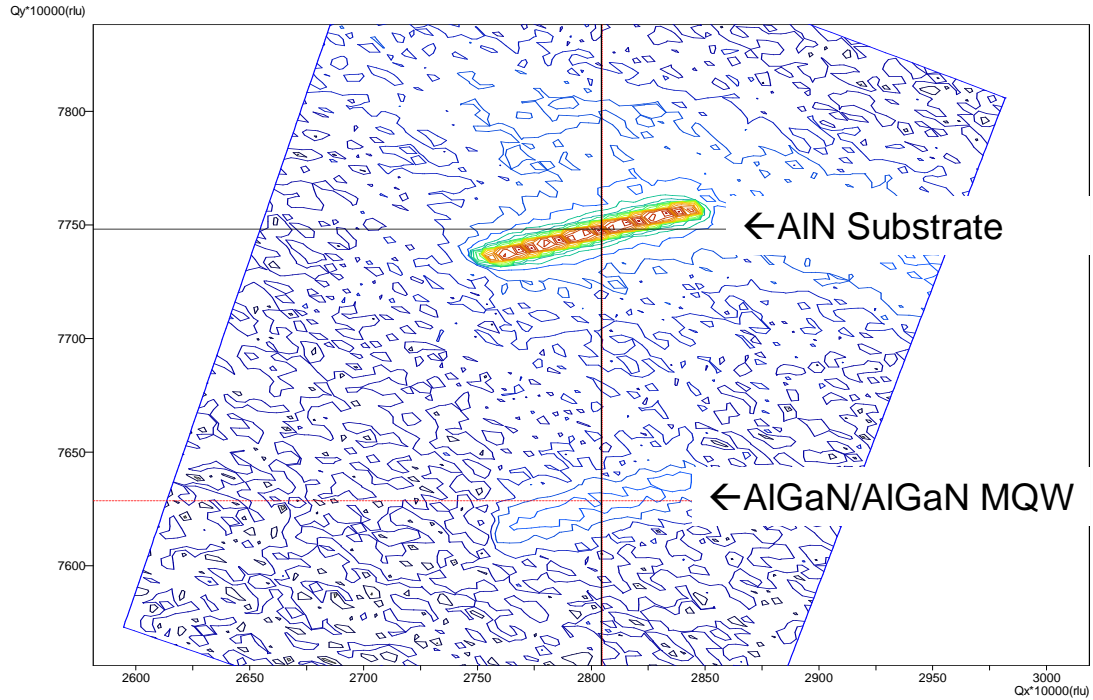
**Figure 5.9 Reciprocal-space mapping of the multi-quantum well sample taken via x-ray diffraction. The horizontal alignment of the multi-quantum well peak to the substrate indicates the layer is fully strained (i.e. pseudomorphically grown).**

Following growth, the wafer was thinned to 80 μm and Fabry-Perot etalons were formed using cleaved *m*-plane facets with a 1.25-mm long resonant cavity. No high reflection (HR) facet coatings were used. The laser bars were optically pumped by an ArF Excimer laser ($\lambda = 193$ nm) with a pulse width of 20 ns at a repetition rate of 10 Hz. The laser beam passes through an optical aperture with width of 0.1 cm and length of 1.27 cm and was illuminated over the surface of the cleaved bars. Attenuators were inserted to vary the pump power and a Glan-Laser α-BBO polarizer was used to measure the polarization of light emission. An optical fiber was placed in the proximity of the *m*-plane facets for spontaneous and stimulated light emission detection. The photon emission was collected and analyzed using an Ocean Optics Maya 2000 Pro spectrometer with a spectral resolution of 0.2 nm.
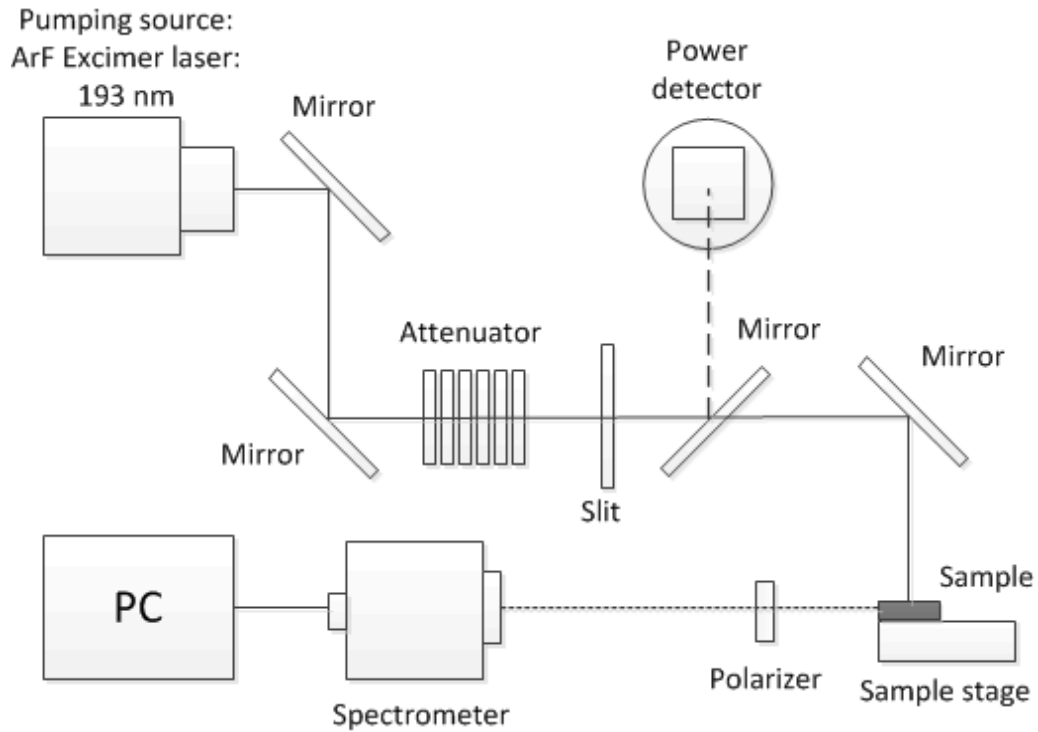
**Figure 5.10  Schematic diagram of optical measurement system.**

The photon emission spectrum at room-temperature with different pumping power densities is shown in Figure 5.11.  The peak emission wavelength was $\lambda = 246.8$ nm with the spectral linewidth reducing to 1.3 nm at the maximum measured pump-power of 709 kW/cm$^2$.  The optical output power as a function of excitation density (*L-L* curve) is shown in Figure 5.12 demonstrating a distinct threshold characteristic at a threshold pump power density ($P_{th}$) of 455 kW/cm$^2$.  The stimulated emission output increases linearly with the pumping power density beyond the threshold.  The measured $P_{th}$ is nearly three times lower than previously reported photo-pumped UV lasers grown on 4H-SiC at a similar emission wavelength of 241.5 nm [54].
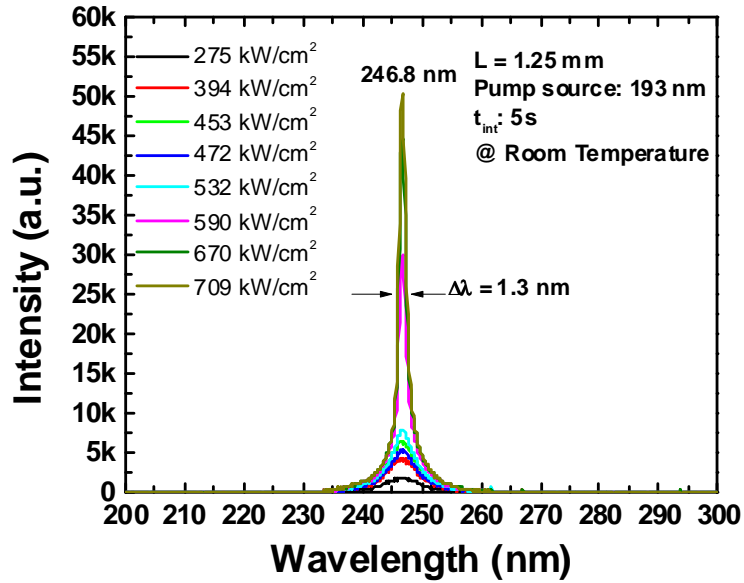
**Figure 5.11 Light-spectra of the MQW structure at various pump-power densities.**
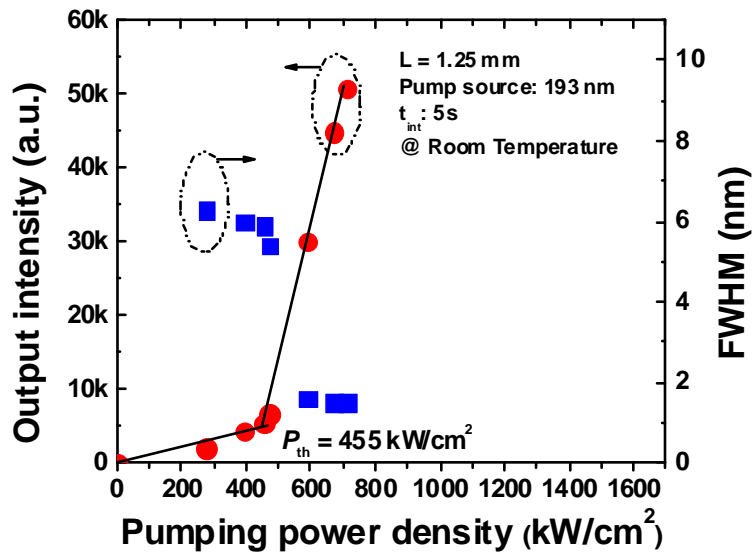


**Figure 5.12 Output intensity and spectral linewidth as a function of pump-power density. The threshold for lasing is 455 kW/cm2.**

The transverse electric (TE) and transverse magnetic (TM) emission spectra are shown in Figure 5.13 for the cleaved laser bar on native AlN substrate operating above threshold and the same structure grown on a sapphire substrate. We observed that the stimulated emission is strongly TE polarized for the device on AlN. On the contrary, the

spontaneous emission for the same MQW structure grown on AlN on sapphire is dominated by TM polarization. For AlGaN-based lasers, the polarization of the light emission is predicated to switch from the TE mode to the TM mode as the emission wavelength decreases from near-UV to deep-UV with corresponding increased AlN mole fraction since the topmost valence band transitions from heavy hole (TE polarization) to crystal-field-split hole (TM polarization) [107,108]. Our results (along with those of references 52, 53, and 109) suggest a mixing of these valence bands where a strong dependence on composition and strain state enables TE-mode gain to continue to dominate into the DUV region while TM-mode sees a modest boost for pseudomorphic AlGaN layers. This is similar to the conclusion reached by J. E. Northrup *et al.* in reference 110.
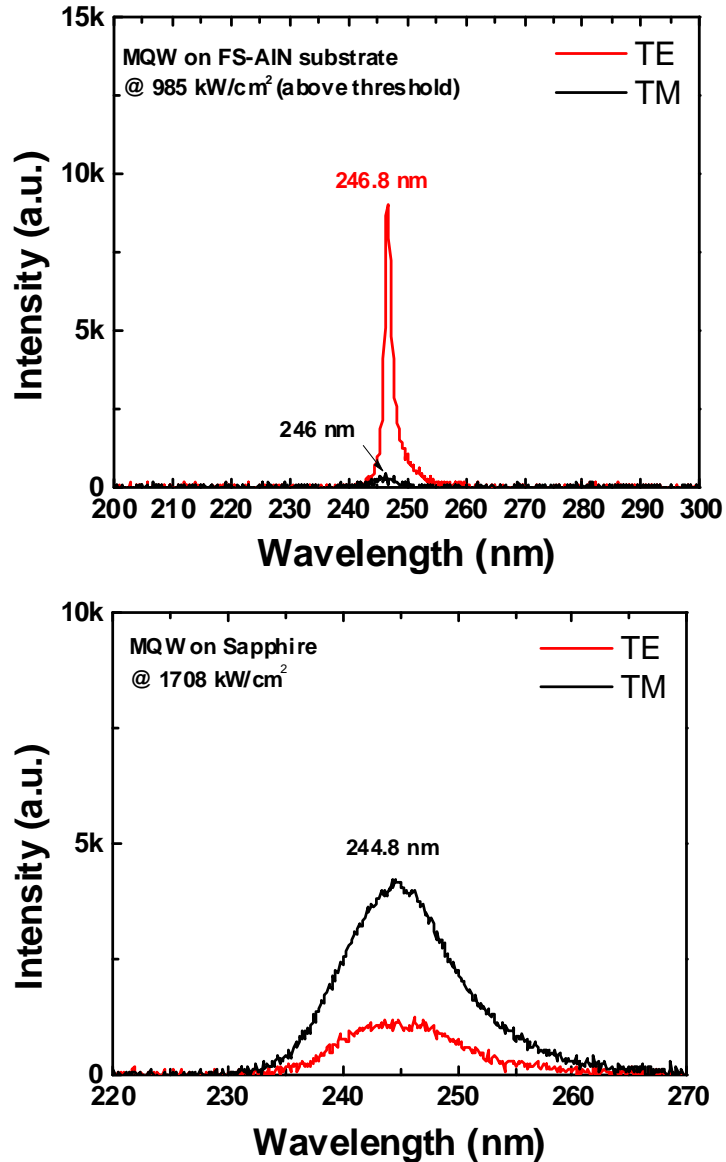
**Figure 5.13 Output-polarization measurements for identical MQW samples grown on FS-AlN and sapphire substrates. The stimulated emission spectrum of the sample on FS-AlN demonstrates TE-dominant polarization, while that on sapphire is dominated by TM polarization.**

In summary, we have used bulk-grown (0001) AlN substrates for the growth of AlGaN/AlN based MQW heterostructures by MOCVD to achieve DUV stimulated emission at 300K. By eliminating ancillary cladding and contact layers, we optimized the design for optical pumping and were able to reduce the pump power threshold density

while also reducing the emission wavelength. The peak wavelength demonstrated was 246.8 nm with a threshold power density of 455 kW/cm$^2$ and dominating TE polarization mode. These results confirm the viability of AlN substrates for future development of DUV AlInGaN based laser diodes.

## 5.4 Optimization of Optically-Pumped AlGaN MQW Structure using Dual-TMGa Source Growth Scheme

While the MQW structure designed for optical pumping yielded an impressive result, we observed an anomaly in the epitaxial layers by high-resolution transmission electron microscopy (HRTEM). As shown in Figure 5.14, the multi-quantum wells and multi-quantum barriers are separated by a high contrast layer. Further analysis of this layer was performed using high-angle annular dark field (HAADF) imaging coupled to the scanning tunneling electron microscope. The HAADF detector collects incoherently scattered electrons- as opposed to Bragg scattered electrons- which are highly sensitive to the square of the atomic number of atoms in the sample. Thus, a higher count indicates a higher atomic number. In this case, the higher atomic number indicates more gallium and therefore smaller bandgap. As seen in HAADF image of Figure 5.15, the high-contrast layers have a higher aluminum mole fraction spanning several monolayers and thus a larger bandgap than the quantum barriers. The result is a non-ideal band profile of the MQW structure that would inhibit the distribution and efficient radiative recombination of generated excitons.
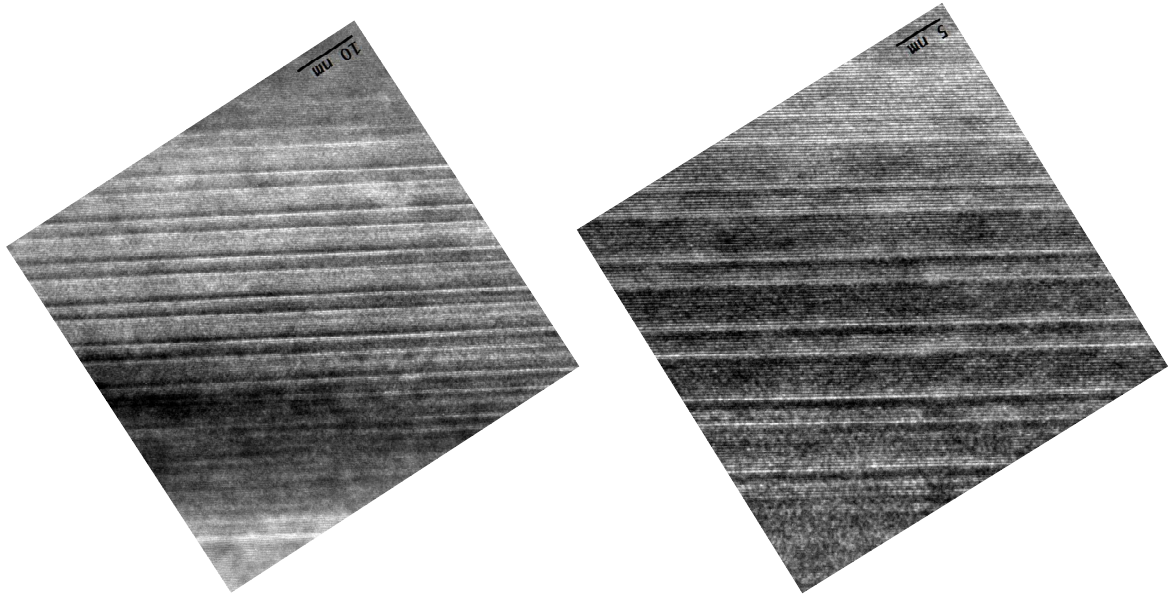
**Figure 5.14 HRTEM image taken under (1-100 ) axis of AlGaN MQW structure grown using a single TMGa source.**
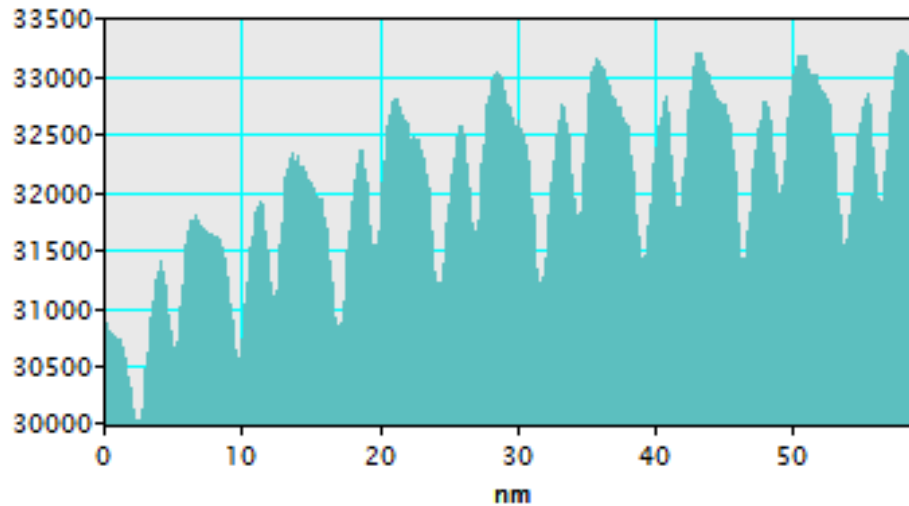


**Figure 5.15 HAADF measurement of the MQW active region grown using a single TMGa source. High peaks correspond to higher AlN mole fraction.**

The source of this layer was hypothesized to be a deficiency in our MOCVD growth recipe; specifically in our use of a single TMGa source. In order to grow our MQW active region, we need change the $Al_xGa_{1-x}N$ composition for the wells and

barriers. With a single TMGa source, this involved pausing the growth for 5-10 seconds while the TMGa flow rate ramped to the appropriate level. During this growth interruption, residual TMAl and aluminum from the previous layer may have mixed with the $NH_3$ over pressure to create an AlN rich layer at each interface.

To eliminate this effect, we made use of a second TMGa source. For the MQW region, the $NH_3$ and TMAl flow rates were kept constant while one TMGa source was set at the flow rate for a quantum barrier, and the other for a well. Thus we could instantly switch between them without having to pause the growth for a ramping time. With this dual-source growth scheme, we grew a structure identical in design to that of Figure 5.7. HRTEM was performed on this new sample and no high contrast layers were observed as shown in Figure 5.16. Neither does a HAADF analysis reveal any high AlN interface layers, as seen in Figure 5.17.
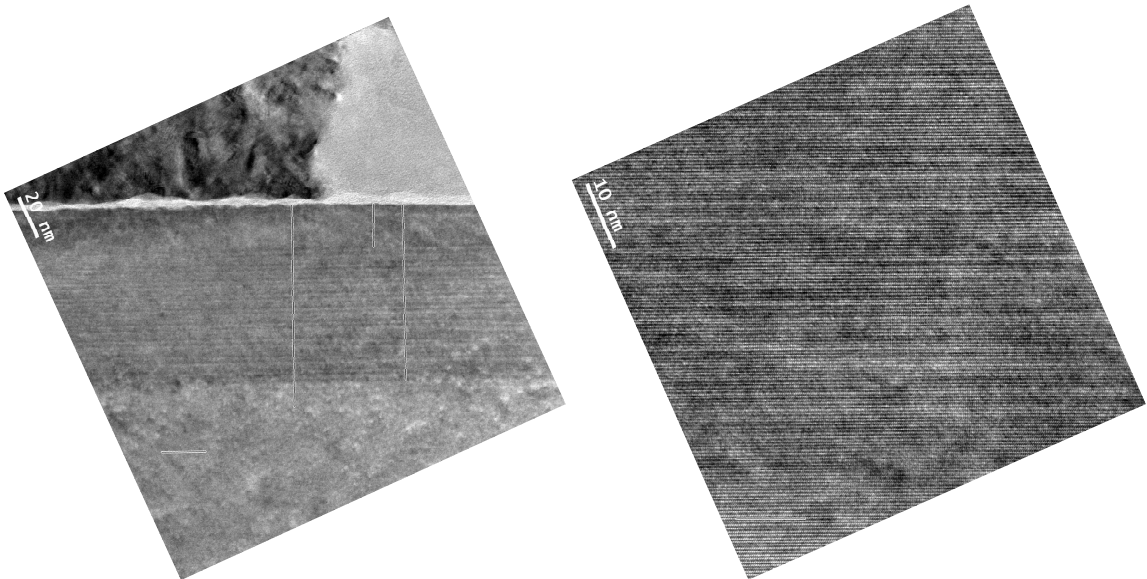


**Figure 5.16  HRTEM image taken under (1-100 ) axis of AlGaN MQW structure grown using a dual TMGa growth scheme.**
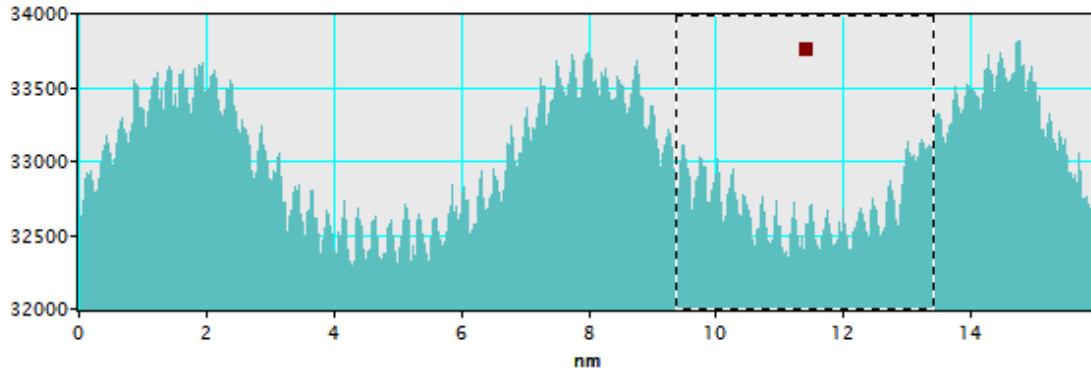
**Figure 5.17 HAADF measurement of the MQW active region grown using a dual TMGa growth scheme.**

As with the previous structure, high crystal-quality was measured by atomic force microscopy illustrated in Figure 5.18: terraced step-flow is observed, characteristic of two-dimensional layer-by-layer III-nitride epitaxial growth. The RMS roughness is 0.37 nm and 0.32 nm at $10 \times 10$ μm$^2$ and $5 \times 5$ μm$^2$ measurements, respectively, indicating a relatively smooth surface with low defect density.
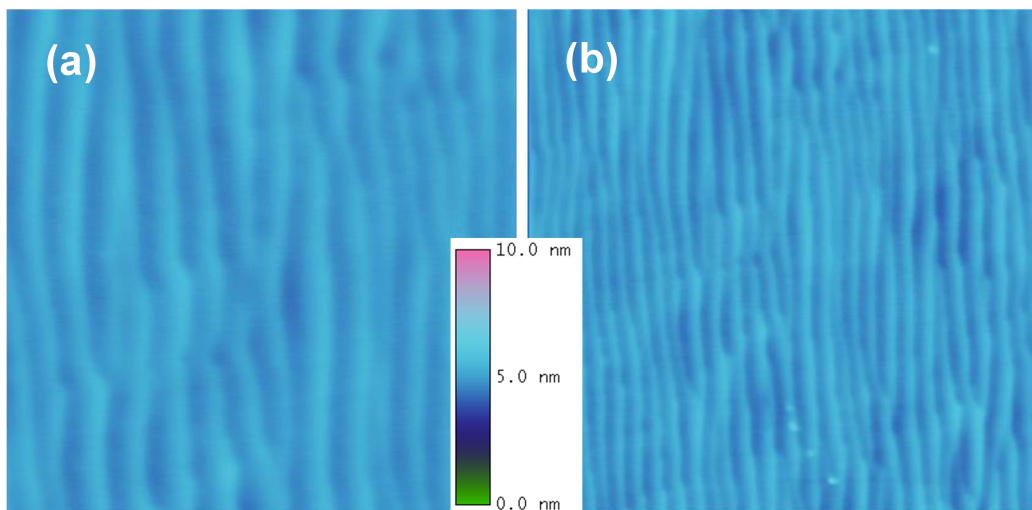


**Figure 5.18  Atomic-force microscopy measurements of the structure grown on (0001) AlN substrate taken at (a) $5 \times 5$ μm$^2$ and (b) $10 \times 10$ μm$^2$.**

The photon emission spectrum at room-temperature with different pumping power densities is shown in Figure 5.19. The peak emission wavelength was $\lambda = 243.5$ nm with the spectral linewidth reducing to 2.1 nm at the maximum measured pump-power of 620 kW/cm$^2$. The optical output power as a function of excitation density (*L-L* curve) is shown in Figure 5.20 demonstrating a distinct threshold characteristic at a threshold pump power density ($P_{th}$) of 427 kW/cm$^2$. The stimulated emission output increases linearly with the pumping power density beyond the threshold. Compared to the sample using a single TMGa source, the wavelength was reduced by 3 nm and the $P_{th}$ reduced by 27 kW/cm$^2$.
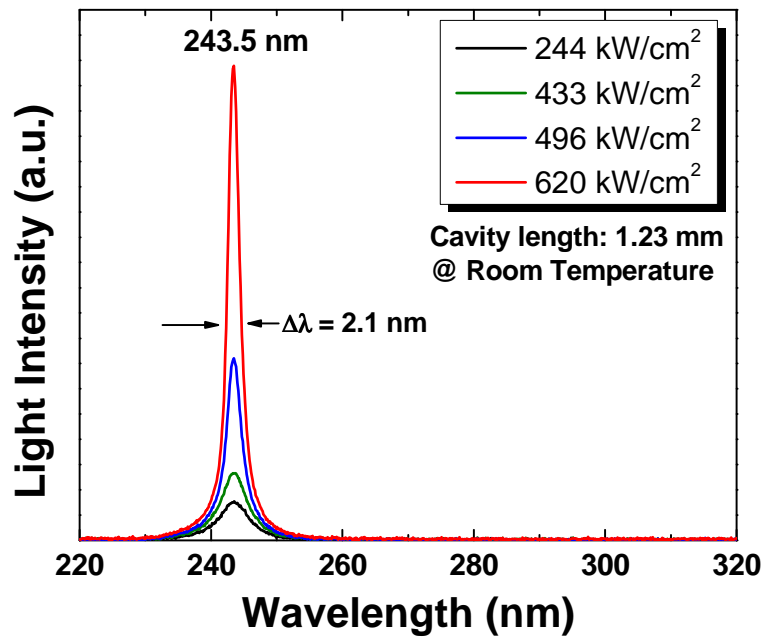


**Figure 5.19   The laser emission spectra with pump power densities below and above threshold at room-temperature.**
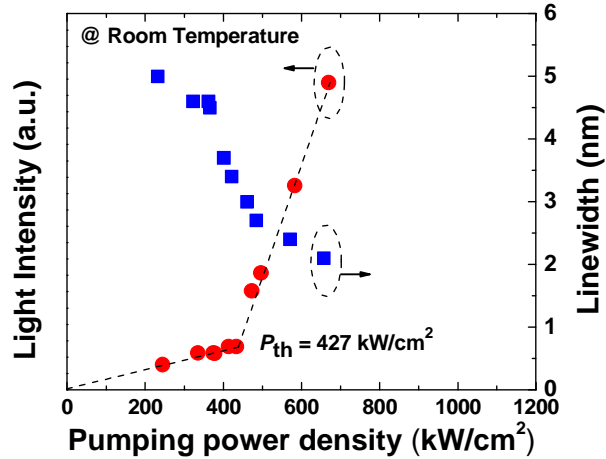
**Figure 5.20  Light-output intensity and linewidth as a function of the optical pump power density at room-temperature with lasing at λ = 243.5 nm.**

The transverse electric and transverse magnetic emission spectra from the cleaved laser bar operating above threshold are shown in Figure 5.21.  We observed that the stimulated emission is strongly TE-polarized with the degree of polarization (*P*) greater than 0.9, similar to the single TMGa source sample.  It is also noted that the TE-mode emission wavelength is about 1.6 nm longer than that for TM-mode emission.
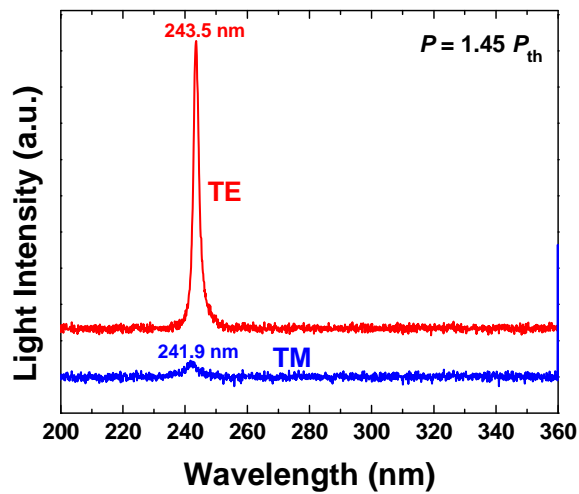


**Figure 5.21  TE and TM-modes emission spectra for the same laser bar operating above threshold at room-temperature.**

103

**5.4.1 Reduction of Threshold Power via MQW Reduction**

Utilizing the dual-TMGa growth scheme, the design of Figure 5.7 was further optimized to reduce the laser threshold power density. By reducing the cap layer from 10 nm to 8 nm, we can minimize the excitation beam absorption while still screening surface states. By reducing the number of quantum wells from ten to eight, we can reduce the number of states requiring population inversion before lasing occurs. However, to maintain the same amount of optical flux within the active region, we have increased the width of the quantum well slightly from 2.8 to 3 nm, and that of the quantum barrier from 5 nm to 6 nm. Thus the overall change in width of the active area changes only slightly from 78 to 72 nm.

These small changes resulted in a dramatic improvement. The wafers were cleaved into bars with cavity length of 1.45 nm. The emission wavelength was measured to be 245.3 nm with a linewidth of 0.9 nm, as per Figure 5.22. The threshold power density was reduced to as low as 297 kW/cm$^2$ for our champion device as shown in Figure 5.23. As with previous measurements, TE-mode polarization dominates as exhibited in Figure 5.24, but this time with no sign of TM-polarization.
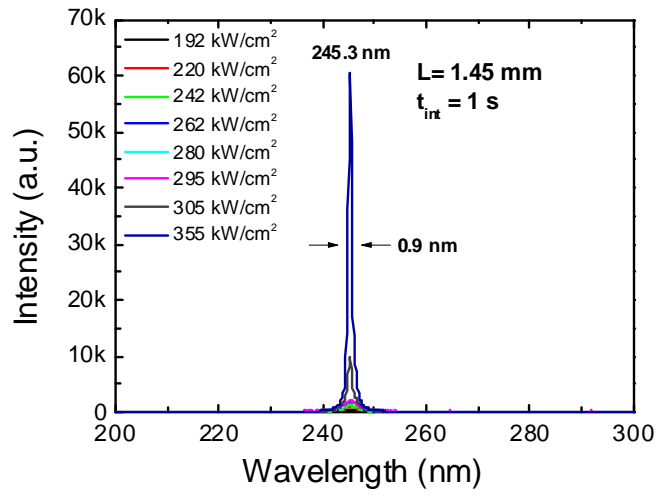
**Figure 5.22  Laser emission spectrum of the optimized optically pumped structure.**
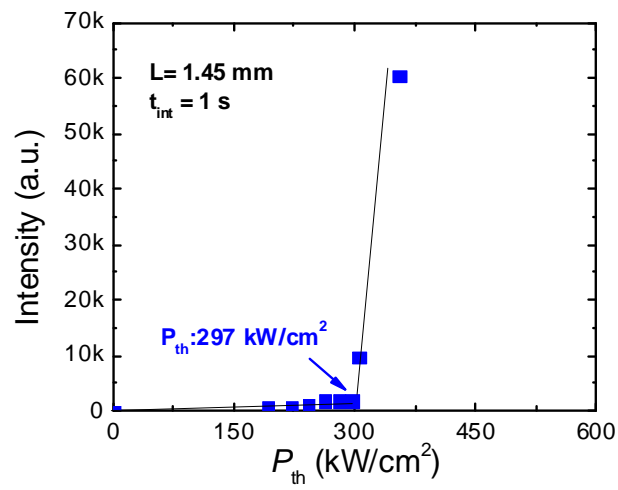


**Figure 5.23  Light-output intensity as a function of the optical-pump power density at room-temperature with lasing at λ = 245.3 nm.**
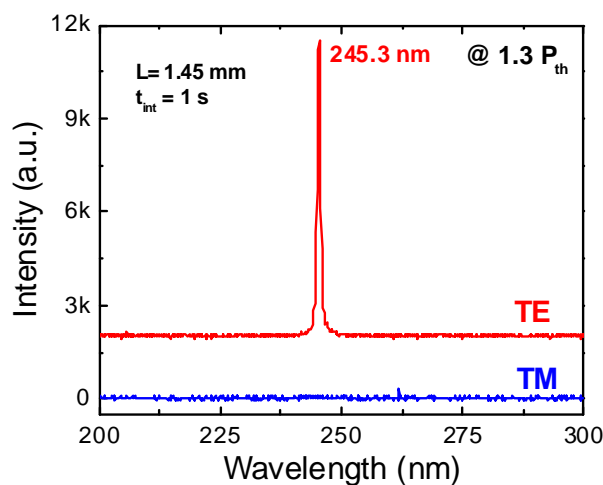
**Figure 5.24 TE and TM-modes emission spectra for the optimized laser bar operating at 1.3x the threshold power density at room-temperature.**

In summary, we have used native AlN substrates to grow AlGaN/AlN based MQW heterostructures by MOCVD for DUV stimulated emission. The use of a dual-TMGa source growth scheme eliminated interface layers of high AlN observed in the active region of the sample grown using a single TMGa source. The result was a more uniform band profile within the MQW region and thus reduced threshold pump power density. The peak wavelength demonstrated was at 243.5 nm with a threshold power density of 427 kW/cm$^2$ and dominating TE-polarization mode. To further optimize absorption of the excitation beam, we reduced the thickness of the AlN cap layer, and eliminated two periods of the MQW, while increasing well and barrier thickness to keep the overall area of excitation roughly the same. The result was a dramatic reduction in threshold power density to 297 kW/cm$^2$ at 245.3 nm. Further optimization of the device parameters and the addition of high-reflection coatings are expected to yield even better performance in the near future.

# CHAPTER 6

# GALLIUM AUTO-DOPING OF INDIUM ALUMINUM NITRIDE MATERIAL

During our experiments, we sought to optimize the growth and crystal quality of InAlN on AlN templates by varying temperature and pressure. The expected result was to find a functional relationship between each parameter and the material composition as there is with AlGaN and InGaN. But we eventually encountered some irregularities. First, we observed the composition would not change over a certain range of temperature, as measured by XRD and plotted in Figure 6.1. This mysterious compositional locking effect was unexpected: while a non-linear trend may be anticipated, a piecewise saturation region of no change over a range of 100 ℃ is somewhat unusual when compared to similar trends for AlGaN and InGaN. Secondly, we observed a significant variation in composition between different runs using the same conditions (e.g. precursor flow rate, temperature, pressure, V/III). Repeatability is crucial to the experimental method, and so the cause of such variation must be explained by an occurrence outside of the input parameters.
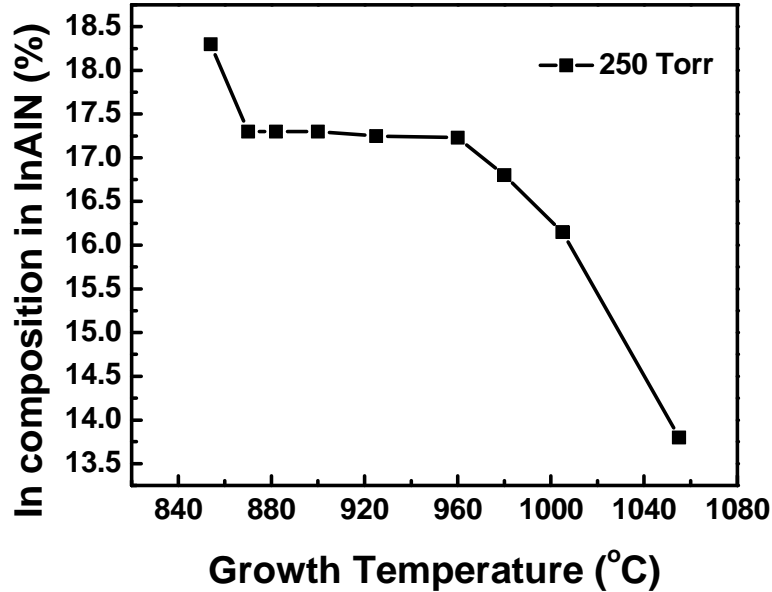
**Figure 6.1 The supposed "compositional-locking" effect of InAlN as measured by XRD.**

Over time, we noticed a pattern that the composition would seemingly reset itself if immediately preceded by a run involving GaN. Each successive run would then see a decrease in indium composition according to XRD observation; that is, the ternary peak would shift to higher angles, closer to that of AlN, with the only variation being the number of runs between that and the last GaN run. An example of this phenomenon is shown in Figure 6.2, with four spectra of InAlN samples on AlN templates all grown under the same conditions. The first InAlN run, shown by the blue curve, was grown immediately following a thick GaN template growth. With each proceeding run, the ternary peak moves closer to that of the AlN template, indicating that the aluminum content is increasing at expense of indium, or as it turns out, gallium.
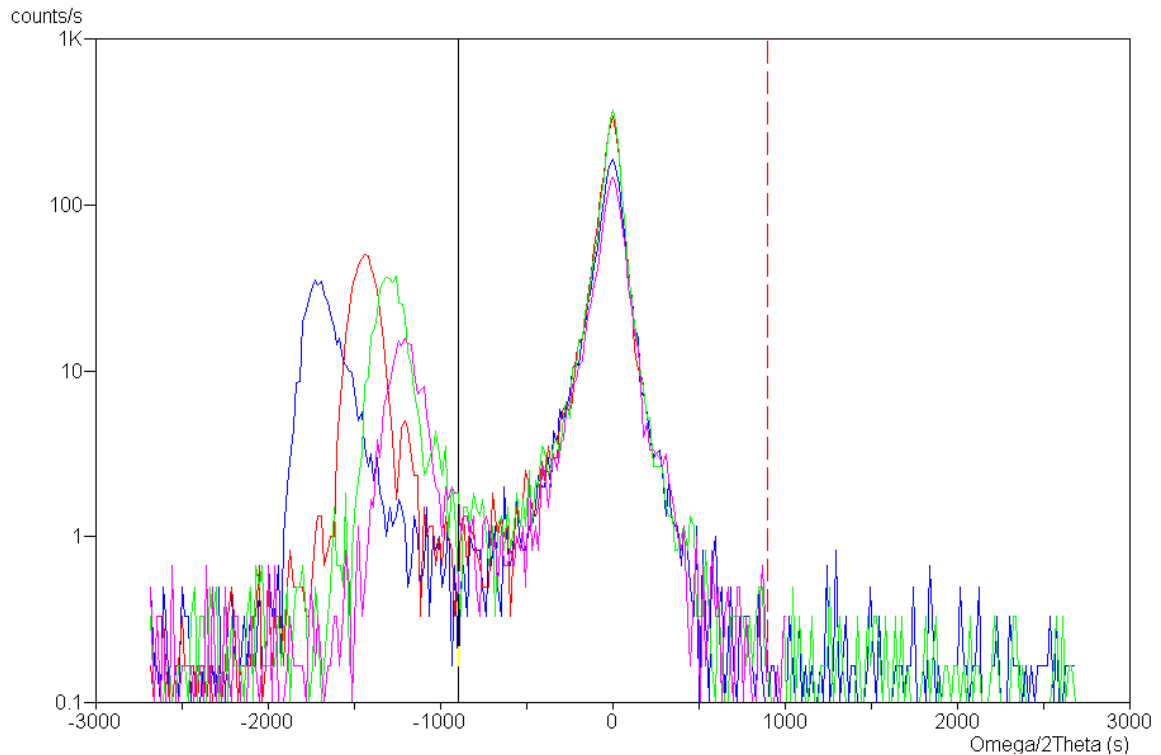
**Figure 6.2 XRD diffraction spectra of four InAlGaN samples grown using the same condition.**

Upon further investigation to determine the chemical composition of this material, we observed large concentrations of gallium, and a surprisingly small amount of indium as seen by secondary ion mass spectroscopy (SIMS) in Figure 6.3, and Rutherford backscattering (RBS) in Figure 6.4. The evidence quickly started to mount that some source of gallium was contaminating our InAlN samples. Thus it was concluded that we had been growing quaternary InAlGaN material all along. Further investigation has revealed the indium composition was never higher than 8% and usually only varied from 3-5%. This was shocking since we had not introduced any gallium precursor during these growth runs and the trimethylindium flow rate was relatively high compared to that of trimethylaluminum at a ratio of 4:1. And yet we were observing what was essentially AlGaN with a small sprinkling of indium. In a similar fashion, Zhu et al. observed a large

amount of unintentional gallium contamination during InAlN growth and attributed its source to their GaN template [111]. However, our growth of high [Al] compounds starts with an AlN template which we have determined via SIMS and RBS to contain no significant amounts of gallium incorporation. Thus the unintentional auto-doping of gallium accompanies only the inclusion of indium.
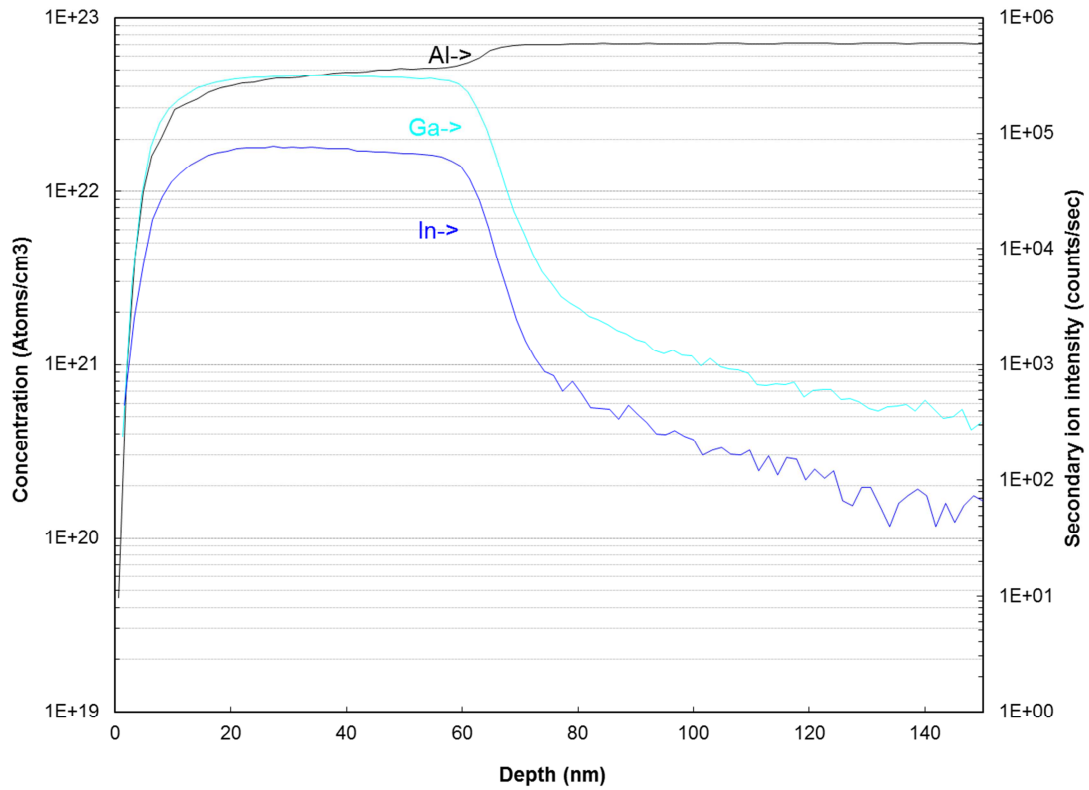


**Figure 6.3 SIMS depth profile of InAl(Ga)N grown on AlN template on sapphire.**
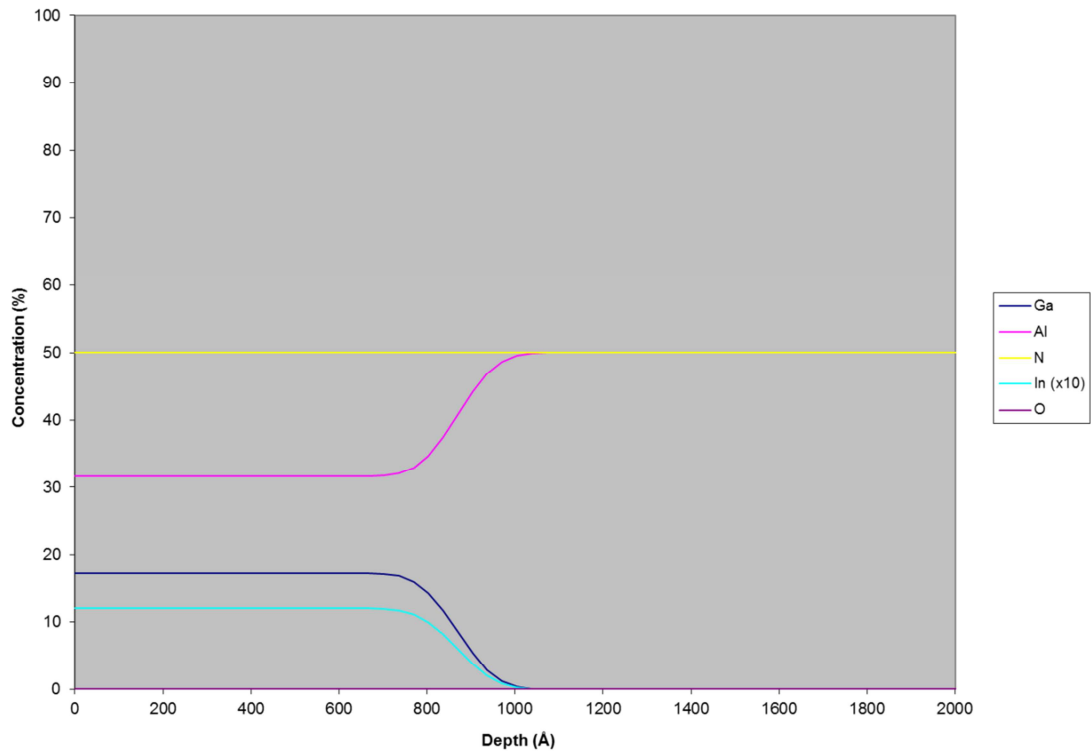
**Figure 6.4 RBS depth profile InAl(Ga)N grown on AlN template on sapphire.**

This phenomenon is explained by the nature of gallium and indium, and the design of our MOCVD reactor.  Firstly, it must be noted that solid gallium and indium will form a eutectic when simply brought into contact with one another at room temperature [112,113,114].  Second, although the 6 x 2" Thomas Swan MOCVD reactor is a pedestal style reactor, meaning the heating element is directly below the growth susceptor and does not encompass the entire chamber, the walls of the chamber - which consist of stainless steel and a quartz liner -  are heated by convection when the temperature of the heater is raised to over 800º C for a typical InAlN run.   This convection heating provides conditions that are more than suitable for the formation of In-Ga eutectic, which is then desorbed from the reactor wall or even the showerhead and finds its way to the sample.

The "memory effect" of the p-type dopant bis(cyclopentadienyl)magnesium has been well documented for nitride materials grown by MOCVD [11]. Because of the high stickiness of $Cp_2Mg$, the precursor will tend to coat the gas lines and walls of the reactor before being incorporated into the material, resulting in a "delayed turn-on" as observed in the depth profile via SIMS. This stickiness also provides a source of magnesium atoms even when the precursor source is closed, resulting in a delayed turn off in the depth profile as well. We propose a similar effect for the unintentional gallium auto-doping observed in InAlN when grown in a vertical-showerhead MOCVD reactor. Following a gallium-rich run, adatoms remain in the reactor environment including the gas lines, showerhead, chamber, and growth susceptor. During AlN or AlGaN runs, there is no indium present to facilitate eutectic formation, resulting gallium free samples as shown by the XRD spectrum as shown in Figure 6.5 and the chemical composition depth profiles of the previous two figures. For InGaN runs, the trimethylgallium flow rate is high enough so as to screen this effect.
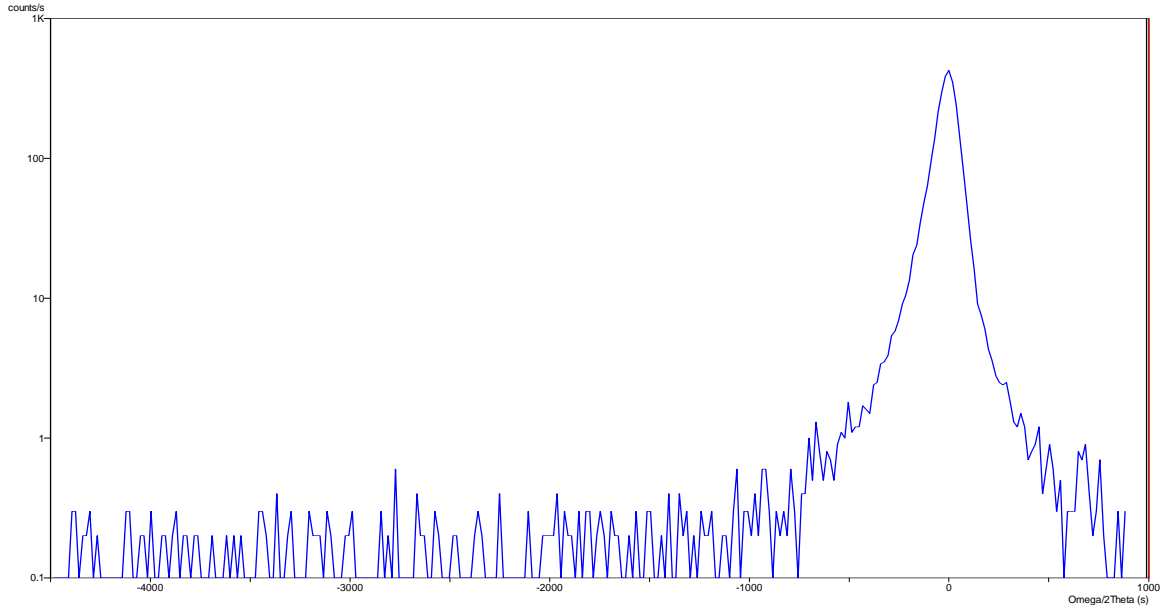
**Figure 6.5 XRD (002) *ω-2θ* scan of AlN grown on an AlN template. The lack of an additional ternary material peak demonstrates that AlN can be grown free of the gallium autodoping effect.**

In conclusion, we have observed the compositional variability of InAl(Ga)N to be difficult to precisely predict and control, since it depends not only on the growth condition of the current run, but also that of the runs prior to it. The situation is further complicated when growing a complex heterostructure that also includes gallium containing materials such as a laser diode with AlGaN active region and InAl(Ga)N claddings. In an attempt to control this process, we have begun purposefully flowing a low amount of trimethylgallium during all InAl(Ga)N runs in order to screen the auto-doping effect. This is successful in terms of repeatability, but the indium composition remains stubbornly low each time. Therefore, in order to effectively take advantage of InAl(Ga)N, its growth dynamics must be rigorously studied, the effect of indium incorporation must be fully understood and all epitaxial designs must take these practical limitations into account.

# CHAPTER 7

# SUMMARY AND FUTURE WORK

Metalorganic chemical vapor deposition was used to develop two advanced electronic and optoelectronic devices based on III-nitride materials: a heterojunction bipolar transistor and a deep-ultraviolet light emitter. The InAlN material system was explored for possible applications to DUV lasers; an unintentional auto-doping phenomenon was observed where residual gallium was incorporated into the material, and its influence and source was examined.

## 7.1 Heterojunction Bipolar Transistors

State-of-the-art heterojunction bipolar transistors were developed for advanced high power electronic device operations. The structure of the device was optimized on sapphire substrates, with specific attention given to the composition of the base region for an GaN/InGaN/GaN device. Both $x_{In} = 0.03$ and 0.05 for the $In_xGa_{1-x}N$ base were grown in separate structures for comparison [115]. The higher indium composition and lower bandgap of the 5% sample was expected to provide advantages in terms of superior emitter-injection efficiency and base doping level. However, the increased lattice strain

associated with heteroepitaxial growth on the underlying GaN collector advanced the

formation of defects when compared to the 3% sample, specifically the formation of V-

defects which are common to InGaN. These defects acted as current sinks and non-

radiative recombination centers, causing the performance of the $x_{In}$ = 0.03 and 0.05

samples to be comparable with slight edge to the $In_{0.03}Ga_{0.97}N$ sample. The D.C. gain was

~37 for both while the reverse biased break down voltage ($V_{CE0}$) was 110 V using $x_{In}$ =

0.03 for the base, double the value obtained for the $x_{In}$ = 0.05 base at 55 V.

Growth on a native free-standing GaN substrate was then developed using $x_{In}$ =

0.03 for the base [116]. Homoepitaxial growth allowed for a reduction in defect

formation, thus increasing the non-radiative recombination lifetime for minority carriers.

We were able to demonstrate a maximum differential current gain of 120 and D.C. gain

of 90 for the device on FS-GaN compared to 21 and 19 for that on sapphire for a 20 x 20

$\mu m^2$ device. The maximum current density for this device was 12 $kA/cm^2$ and 1.81

$kA/cm^2$ for the devices on FS-GaN and sapphire respectively. The genesis of defects was

examined for each device and quantitatively analyzed to further explain the benefits of

homoepitaxial growth on FS-GaN.

Further work in III-nitride HBTs grown by MOCVD will include high frequency

characteristics. However, in order to take full advantage of homoepitaxial growth for this

purpose, native GaN substrates with insulating properties will need to be developed for

sufficient device isolation. The doping profile of our structure may also be further

optimized; specifically the doping level of the emitter may be reduced slightly to reduce

the BE-junction capacitance.

## 7.2 Deep-Ultraviolet Light Emitters

High aluminum containing heteroepitaxial structures were developed for

ultraviolet optoelectronic applications.  In summary, we have grown and fabricated an

ultraviolet laser on AlN substrate and demonstrated stimulated emission via optical

pumping. The elimination of thermal mismatch reduction in the strain state between the

substrate and the AlN buffer layer yielded reduced defect formation compared to

conventional substrates such as sapphire or SiC, thus enabling laser action at lower

thresholds.  The epitaxial design of our first structure includes a full *n*-cladding layer for

future expansion into a full-diode design with anticipated electrical injection. Stimulated

emission at 257 nm was observed from a AlGaN/AlN multi-quantum well with a  pump

power threshold density ($P_{th}$) of 1.88 MV/cm$^2$ [117]. While stimulated emission is an

achievement itself, the power threshold density must be significantly reduced for

electrical injection to be practical. In the ½ laser diode design, the optical field overlap with the active region was quite poor, pushing the threshold power high.

For a more effective demonstration of stimulated emission by AlGaN/AlN MQWs, we optimized the structure for optical pumping experiments. By eliminating cladding and contact layers, we were able to reduce the pump power threshold density while also reducing the emission wavelength by improving the confinement of the optical field within the active region. The peak wavelength demonstrated was 246.8 nm with a threshold power density of 455 kW/cm$^2$ and dominating TE-polarization mode [118]. These results confirm the viability of AlN substrates for future development of DUV AlInGaN based laser diodes.

To further optimize this optically-pumped DUV MQW structure, we altered the growth recipe to use two TMGa sources instead of one to eliminate interface layers of high AlN content. The peak wavelength demonstrated was at 243.5 nm with a threshold power density of 427 kW/cm2 and dominating TE-polarization mode [119]. A further optimization of the structure by removing two of the quantum wells yielded an emission wavelength of 245.3 nm with a threshold of 297 kW/cm$^2$. Compared to previous work, these results represent a substantial improvement in terms of reducing the wavelength

below 250 nm while simultaneously reducing the pump-power threshold density below 1

MW/cm$^2$ as shown in Figure 7.1.
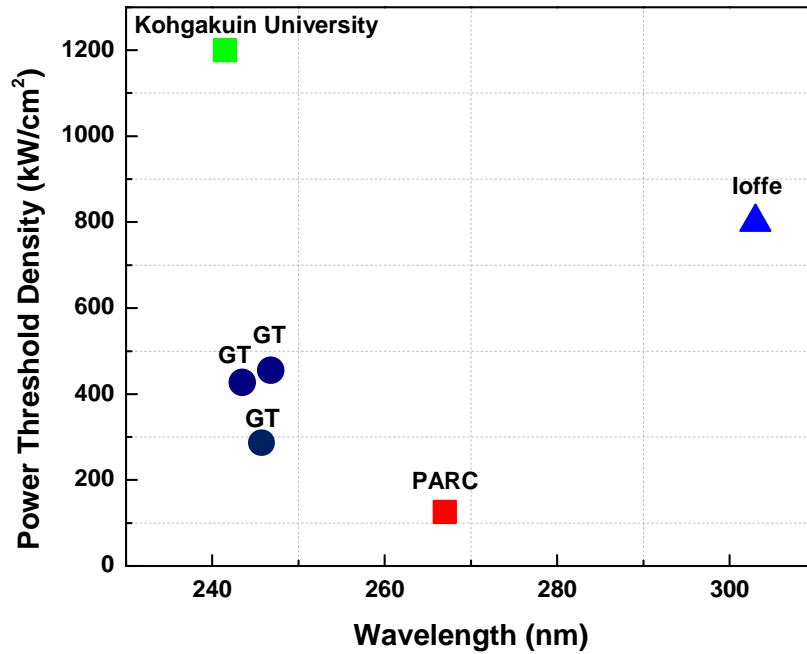


**Figure 7.1 Graphical summary of published results of optically pumped DUV lasers.**

Further development of DUV laser diodes will depend heavily on development of

high conductivity, high aluminum containing $Al_xGa_{1-x}N$ for electrical injection. While *n*-

type $Al_xGa_{1-x}N$ up to $x = 0.75$ has been achieved, *p*-type conductivity will be a much

more monumental challenge due the high acceptor activation energy. Demonstration of a

high [Al] *pn*-diode will be the first step in realization of this device. Effective cladding

layers and perhaps more importantly effective high-reflective facet coatings must also be developed for sufficient optical confinement.

## 7.3 Gallium auto-doping in InAl(Ga)N

An alternative ternary compound of InAlN was examined for improved performance for III-nitride UV emitters. Its ability to lattice match AlGaN at higher bandgap energies would be beneficial to the efficiency of the device by eliminating interface-polarization charge and significantly reducing strain-induced internal piezoelectric fields. However, we discovered a gallium auto-doping effect during the course of our studies, which takes place when indium is introduced into the growth chamber. The causes and effects of this phenomenon were studied, and the source was determined to be the formation of a gallium-indium eutectic on non-growth surfaces (e.g. reactor walls) which is then transported to the substrate and takes part in the epitaxial growth reaction.

Elimination or at least control of this auto-doping phenomenon is a pre-requisite to its incorporation into a device. This would enable lattice-matched cladding layers and potentially a higher doping efficiency for contact layers. Thus further development of this material is certainly worthwhile.

# REFERENCES

[1]    H. P. Maruska and J. J. Tietjen, "The preparation and properties of vapor-deposited single crystalline GaN," <u>Applied Physics Letters</u>, vol. 15, pp. 327, 1969.

[2]    H. M. Manasevit, F. M. Erdmann, and W. I. Simpson, "The use of metalorganics in the preparation of semiconductor materials," <u>Journal of the Electrochemical Society</u>, vol. 118, no. 11, pp. 1864, 1971.

[3]    H. Amano, N. Sawaki, I. Akasaki, and Y. Toyoda, "Metalorganic vapor phase epitaxial growth of a high quality GaN film using an AlN buffer layer," <u>Applied Physics Letters</u>, vol. 48, pp. 353, 1986.

[4]    S. Nakamura, T. Mukai, and M. Senoh, "Si- and Ge-Doped GaN films grown with GaN buffer layers," <u>Japanese Journal of Applied Physics</u>, vol. 31, pp. 2883, 1992.

[5]    S. Nakamura, N. Iwasa, M. Senoh, and T. Mukai, "Hole compensation mechanism of p-type GaN films," <u>Japanese Journal of Applied Physics</u>, vol. 31, pp. 1258, 1992.

[6]    H. Amano, M. Kito, K. Hiramatsu, and I. Akasaki, "P-type conduction in Mg-doped GaN treated with low-energy electron beam irradiation (LEEBI)," <u>Japanese Journal of Applied Physics</u>, vol. 28, pp. L2112, 1989.

[7]    S. Nakamura, T. Mukai, M. Senoh, and N. Iwasa, "Thermal annealing effects on p-type Mg-doped GaN films," <u>Japanese Journal of Applied Physics</u>, vol. 31, pp. L139, 1992.

[8]    H. M. Manasevit, "Single-crystal gallium arsenide on insulating substrates," <u>Applied Physics Letters</u>, vol. 12, pp. 156, 1968.

[9]     R. D. Dupuis, P. D. Dapkus, R. D. Yingling, and L. A. Moudy, "High-efficiency GaAlAs/GaAs heterostructure solar cells grown by metalorganic chemical vapor deposition," Applied Physics Letters, vol. 31, pp. 201, 1977.

[10]    R. D. Dupuis, P. D. Dapkus, J. N. Holonyak, E. A. Rezek, and R. Chin, "Room-temperature laser operation of quantum-well $Ga_{1-x}Al_xAs$-GaAs laser diodes grown by metalorganic chemical vapor deposition," Applied Physics Letters, vol. 32, pp. 295, 1978.

[11]    Y. Ohba and A. Hatano, "A study on strong memory effects for Mg doping in GaN metalorganic chemical vapor deposition," Journal of Crystal Growth, vol. 145, pp. 214, 1994.

[12]    S. Nakamura and T. Mukai, "High-Quality InGaN Films Grown on GaN Films," Japanese Journal of Applied Physics, vol. 31, pp. L1457, 1992.

[13]    J. Kolnik, I.H. Oguzman, K.F. Brennan, R. Wang, P.P. Ruden, "Monte Carlo calculation of electron initiated impact ionization in bulk zinc-blende and wurtzite GaN," Journal of Applied Physics, vol. 81, pp. 726, 1997.

[14]    P.M. Asbeck, M.F. Chang, K.C. Wang, D.L. Miller, G.J. Sullivan, N.H. Sheng, E. Sovero, J.A. Higgins, "Heterojunction bipolar transistors for microwave and millimeter-wave integrated circuits," IEEE Transactions on Microwave Theory and Techniques, vol. 35, pp. 1462, 1987.

[15]    H. Xing, D.S. Green, L. McCarthy, I.P. Smorchkova, P. Chavarkar, T. Mates, S. Keller, S. DenBaars, J. Speck, U.K. Mishra, "Progress in gallium nitride-based bipolar transistors," in Proceedings of the 2001 Bipolar/BiCMOS Circuits and Technology Meeting, pp. 125-130, 2001.

[16]    J. B. Limb, L. McCarthy, P. Kozodoy, H. Xing, J. Ibbetson, Y. Smorchkova, S. P. DenBaars, and U. K. Mishra, "AlGaN/GaN HBTs using regrown emitter," Electronics Letters, vol. 35, no. 19,  pp. 1671, 2000.

[17] H. Xing, D.S. Green, L. McCarthy, I.P. Smorchkova, P. Chavarkar, T. Mates, S. Keller, S. DenBaars, J. Speck, U.K. Mishra, "Progress in gallium nitride-based bipolar transistors," in <u>Proceedings of the 2001 Bipolar/BiCMOS Circuits and Technology Meeting</u>, pp. 125-130, 2001.

[18] A.P. Zhang, G.T. Dang, F. Ren, J. Han, A.G. Baca, R.J. Shul, H. Cho, C. Monier, X.A. Cao, C.R. Abernathy, S.J. Pearton, "Direct-current characteristics of *pnp* AlGaN/GaN heterojunction bipolar transistors," <u>Applied Physics Letters</u>, vol. 76, pp. 2943, 2000.

[19] T. Makimoto, K. Kumakura, N. Kobayashi, "High current gains obtained by InGaN/GaN double heterojunction bipolar transistors with *p*-InGaN base," <u>Applied Physics Letters</u>, vol. 79, pp. 380, 2001.

[20] K. Kumakura, T. Makimoto, and N. Kobayashi, "Common-emitter current voltage characteristics of a pnp GaN bipolar junction transistor," <u>Applied Physics Letters</u>, vol. 80, pp. 1225, 2002.

[21] K. Kumakura, T. Makimoto, and N. Kobayashi, "Common-emitter current voltage characteristics of a Pnp AlGaN-GaN heterojunction bipolar transistor with a low-resistance base layer," <u>Applied Physics Letters</u>, vol. 80, pp. 3841, 2002.

[22] J. Han, A.G. Baca, R.J. Shul, C.G. Willison, L. Zhang, F. Ren, A.P. Zhang, G.T. Dang, S.M. Donovan, X.A. Cao, H. Cho, K.B. Jung, C. R. Abernathy, S.J. Pearton, R.G. Wilson, "Growth and fabrication of GaN/AlGaN heterojunction bipolar transistor," <u>Applied Physics Letters</u>, vol. 74, pp. 2702, 1999.

[23] L.S. McCarthy, P. Kozodoy, M.J.W. Rodwell, S.P. DenBaars, U.K. Mishra, "AlGaN/GaN heterojunction bipolar transistor," <u>IEEE Electron Device Letters</u>, vol. 20, no. 6, pp. 277-279, 1999.

[24] E. Alekseev, D. Pavlidis, "DC and high-frequency performance of AlGaN/GaN Heterojunction Bipolar Transistors," <u>Solid State Electronics</u>, vol. 44, no. 2, pp. 245-252, 2000.

[25]    J.J. Huang, M. Hattendorf, M. Feng, D.J.H. Lambert, B.S. Shelton, M.M. Wong, U. Chowdhury, T.G. Zhu, H.K. Kwon, R.D. Dupuis, "Graded-emitter AlGaN/GaN heterojunction bipolar transistors," <u>Electronics Letters</u>, vol. 36, no. 14, pp. 1239-1240, 2000.

[26]    W. Gotz, N.M. Johnson, J. Walker, D.P. Bour, R.A. Street, "Activation of acceptors in Mg-doped GaN grown by metalorganic chemical vapor deposition," <u>Applied Physics Letters</u>, vol. 68, pp. 667, 1996.

[27]    E. Bahat-Treidel, F. Brunner, O. Hilt, E. Cho, J. Wurfl, and G. Trankle, "AlGaN/GaN/GaN:C back-barrier HFETs with breakdown voltage of over 1 kV and low $R_{on} \times A$," <u>IEEE Transactions on Electron Devices</u>, vol. 57, no. 11, pp. 3050-3058, 2010.

[28]    L. S. McCarthy, P. Kozodoy, M. J. Rodwell, S. P. DenBaars, and U. K. Mishra, "AlGaN/GaN heterojunction bipolar transistor," <u>IEEE Electron Device Letters</u>, vol. 20, no. 6, pp. 277, 1999.

[29]    J. Jan, A. G. Baca, R. J. Shul, C. G .Willison, L. Zhang, F. Ren, A. P. Zhang, G. T. Dang, S. M. Donovan, X. A. Cao, H. Cho, K. B. Jung, C. R. Abernathy, S. J. Pearton, and R. G. Wilson, "Growth and fabrication of GaN/AlGaN heterojunction bipolar transistor," <u>Applied Physics Letters</u>, vol.74, pp. 2702, 1999.

[30]    B. S. Shelton, D. J. H. Lambert, J. J. Huang, M. M. Wong, U. Chowdhury, T. G. Zhu, H. K. Kwon, Z. Liliental-Weber, M. Benarama, M. Feng, and R. D. Dupuis, "Selective area growth and characterization of AlGaN/GaN heterojunction bipolar transistors by metalorganic chemical vapor deposition," <u>IEEE Transactions on Electron Devices</u>, vol. 48, pp. 490-494, 2001.

[31]    M. K. Kelly, R. R. Vaudo, V. M. Phanse, L. Gorgens, O. A. Ambacher, and M Stutzmann, "Large free-standing GaN substrates by hydride vapor phase epitaxy and laser-induced liftoff," <u>Japanese Journal of Applied Physics</u>, vol.38, pp. L217-L219, 1999.

[32]  K. Kumakura and T. Makimoto, "High performance *pnp* AlGaN/GaN heterojunction bipolar transistors on GaN substrates," <u>Applied Physics Letters</u>, vol. 92, pp. 153509, 2008.

[33]  S. Nakamura and G. Fasol, <u>The Blue Laser Diode</u>, Springer-Verlag, Berlin, 1997.

[34]  S. Nakamura, T. Mukai, and M. Senoh, "Candela-class high-brightness InGaN/AlGaN double-heterostructure blue-light-emitting diodes," <u>Applied Physics Letters</u>, vol. 64, pp. 1687, 1994.

[35]  A. Kinoshita, H. Hirayama, M. Ainoya, Y. Aoyagi, and A. Hirata, "Room temperature operation at 333 nm of $Al_{0.03}Ga_{0.97}N/Al_{0.25}Ga_{0.75}N$ quantum well light-emitting diodes with Mg-doped superlattice layers," <u>Applied Physics Letters</u>, vol. 77, pp. 175, 2000.

[36]  T. Nishida, H. Saito, and N. Kobayashi, "Efficient and high-power AlGaN-based ultraviolet light-emitting diode grown on bulk GaN," <u>Applied Physics Letters</u>, vol. 79, pp. 711, 2001.

[37]  T. Cutler and J. Zimmerman, "Ultraviolet irradiation and the mechanisms underlying its inactivation of infectious agents," <u>Animal Health Research Review</u>, vol. 12, no. 1, pp. 15-23, 2011.

[38]  D. Parthenopoulos and  P. Rentzepis, "Three-dimensional optical storage memory," <u>Science</u>, vol. 245, pp. 843-845**,** 1989.

[39]  H-. H. Chun, J-. Y. Kim, and K. B. Song, "Inactivation of foodborne pathogens in ready-to-eat salad using UV-C irradiation," <u>Food Science and Biotechnology</u>, vol. 19, pp. 547 2010.

[40]  K. Baxter, M. Castle, S. Barrington, P. Withers, V.Foot, A. Pickering, and N. Felton, "UK small scale UVLIF lidar for standoff BW detection," <u>Proceedings of the SPIE,</u> vol. 6739, pp. 67390Z, 2007.

[41]   P. Parbrook and T. Wang, "Light emitting and laser diodes in the ultraviolet," IEEE Journal of Selected Topics in Quantum Electronics, vol. 17, pp. 1402-1411, 2011.

[42]   Y. Ohba, K. Kaneko, H. Katsuno, and M. Kushibe, "Highly efficient InGaN-based 383-nm ultraviolet light-emitting diodes fabricated on sapphire substrate using high-temperature-grown AlN buffer," Applied Physics Express, vol. 1, pp. 101101, 2008.

[43]   V. Adivarahan, A. Heidari, B. Zhang, Q. Fareed, S. Hwang, M. Islam, and A. Khan, "280 nm Deep Ultraviolet Light Emitting Diode Lamp with an AlGaN Multiple Quantum Well Active Region," Applied Physics Express, vol. 2, pp. 102101, 2009.

[44]   S. Fujikawa and H. Hirayama, "284–300 nm Quaternary InAlGaN-Based Deep-Ultraviolet Light-Emitting Diodes on Si(111) Substrates," Applied Physics Express, vol. 4, pp. 061002, 2011.

[45]   T. Wunderer, C. Chua, Z. Yang, J. Northrup, N. Johnson, G. Garrett, H. Shen, and M. Wraback, "Pseudomorphically grown ultraviolet C photopumped lasers on bulk AlN substrates," Applied Physics Express, vol. 4, pp. 092101, 2011.

[46]   A. Yasan, R. McClintock, K. Myes, D. Shiell, L. Gautero, S. Darvish, P. Kung, and M. Razeghi, "4.5 mW operation of AlGaN-based 267 nm deep-ultraviolet light-emitting diodes," Applied Physics Letters, vol. 83, pp. 4701, 2003.

[47]   J. Mickevičius, J. Jurkevičius, K. Kazlauskas, A. Žukauskas, G. Tamulaitis, M.S. Shur, M. Shatalov, J. Yang,  and R. Gaska, "Stimulated emission in AlGaN/AlGaN quantum wells with different Al content," Applied Physics Letters, vol. 100, pp. 081902, 2012.

[48]    K. Ban, J. Yamamoto, K. Takeda, K. Ide, M. Iwaya, T. Takeuchi, S. Kamiyama, I. Akasaki, and H. Amano, "Internal quantum efficiency of whole-composition-range AlGaN multiquantum wells," Applied Physics Express, vol. 4, pp. 052101, 2011.

[49]    H. Yoshida, Y. Yamashita, M. Kuwabara, H. Kan, "Demonstration of an ultraviolet 336 nm AlGaN multiple-quantum-well laser diode," Applied Physics Letters, vol. 93, pp. 241106, 2008.

[50]    Y. A. Xi, K. X. Chen, F. Mont, J. K. Kim, C. Wetzel, E. F. Schubert, W. Liu, X. Li, and J. A. Smart, "Very high quality AlN grown on (0001) sapphire by metal-organic vapor phase epitaxy," Applied Physics Letters, vol. 89, pp. 103106, 2006.

[51]    J. P. Zhang, H. M. Wang, M. E. Gaevski, C. Q. Chen, Q. Fareed, J.W. Yang, G. Simin, and M. Asif Khan, "Crack-free thick AlGaN grown on sapphire using AlN/AlGaN superlattices for strain management," Applied Physics Letters, vol. 80, pp. 3542, 2002.

[52]    T. Wunderer, C. L. Chua, J.E. Northrup, Z. Yang, N. M. Johnson, M. Kneissl, G. A. Garrett, H. Shen, M. Wraback, B. Moody, H. S. Craft, R. Schlesser, R. F. Dalmau, and Z. Sitar, "Optically pumped UV lasers grown on bulk AlN substrates," Physica Status Solidi C, vol. 9, pp. 825, 2012.

[53]    H. Yoshida, Y. Yamashita, M. Kuwabara, and H. Kan, "A 342-nm ultraviolet AlGaN multiple-quantum-well laser diode," Nature Photonics vol. 2, pp. 551, 2008.

[54]    T. Takano, Y. Narita, A. Horiuchi, and H. Kawanishi, "Room-temperature deep ultraviolet lasing at 241.5 nm of AlGaN multiple-quantum-well laser," Applied Physics Letters, vol. 84, pp. 3567, 2008.

[55]   J. Juzmik, "InAlN/(In)GaN high electron mobility transistors: some aspects of the quantum well heterostructure proposal," <u>Semiconductor Science and Technology</u>, vol. 17, pp. 540, 2002.

[56]   S. Choi, H.J. Kim, Z. Lochner, Y. Zhang, Y.-C. Lee, S.-C. Shen, J.-H Ryou, R.D. Dupuis, "Threshold voltage control of InAlN/GaN heterostructure field-effect transistors for depletion- and enhancement-mode operation," <u>Applied Physics Letters</u>, vol. 96, pp. 243506, 2010.

[57]   M.M Satter, H.J. Kim, Z. Lochner, J.-H Ryou, S.-C. Shen, R.D. Dupuis, P.D. Yoder, "Design and analysis of 250-nm AlInN laser diodes on AlN substrates using tapered electron blocking layers," <u>IEEE Journal of Quantum Electronics</u>, vol. 48, no. 5, pp. 711, 2012.

[58]   R. Butte, J.-F. Carlin, E. Feltin, M. Gonschorek, S. Nicolay, G. Christmann, D. Simeonov, A. Castiglia, J. Dorsaz, H.J. Buehlmann, S. Christopoulos, G. Baldassarri Hoger von Hogersthal, A.J.D. Grundy, M. Mosca, C. Pinquier, M.A. Py, F. Demangeot, J. Frandon, P.G. Lagoudakis, J.J. Baumberg, N. Grandjean, "Current status of AlInN layers lattice-matched to GaN for photonics and electronics," <u>Journal of Physics D: Applied Physics</u>, vol. 40, pp. 6328, 2007.

[59]   H.P.D. Schenk, M. Nemoz, M. Korytov, P. Vennegues, A.D. Drager, A. Hangleiter, "Indium incorporation dynamics into AlInN ternary alloys for laser structures lattice matched to GaN," <u>Applied Physics Letters</u>, vol. 93, pp. 081116, 2008.

[60]   M. Trejo, G. H. Jessen, A. Crespo, J.K. Gillespie, D. Langley, D. Denninghoff, G. D. Via, J. Carlin, D. Tomich, J. Grant, H. Smith, "Materials characterization and device performance survey of InAlN/GaN HEMT layers from commercial sources," in <u>Proceedings of the Compound Semiconductor Manufacturing Technology (CS-MANTECH) Conference</u>, 2008.

[61] J. Gillespie, A. Crespo, K. Chabak, M. Kossler, V. Trimble, M. Trejo, G. D. Via, B. Winningham, B. Poling, D. Walker Jr., "Ultra-Thin Barrier Layers for mmw Frequencies in III-N HEMT Technologies," in <u>Proceedings of the Compound Semiconductor Manufacturing Technology (CS-MANTECH) Conference</u>, pp. 181, 2010.

[62] E. V. Yakovlev, A. V. Lobanova, R. A. Talalaev, I. M. Watson, K. Lorenz, and E. Alves, "Mechanisms of AlInN growth by MOVPE: modeling and experimental study," <u>Physica Status Solidi C</u>, vol. 5, pp. 1688, 2008.

[63] C. Hums, J. Bläsing, A. Dadgar, A. Diez, T. Hempel, J. Christen, A. Krost, K. Lorenz, E. Alves, "Metal-organic vapor phase epitaxy and properties of AlInN in the whole compositional range," <u>Applied Physics Letters</u>, vol. 90, pp. 022105, 2007.

[64] J.M. Manuel, F.M. Morales, J.G. Lozano, D. Gonzalez, R. García, T. Lim, L. Kirste, R. Aidam, O. Ambacher, "Structural and compositional homogeneity of InAlN epitaxial layers nearly lattice-matched to GaN," <u>Acta Materiala</u>, vol. 58, no. 12, pp. 4120, 2010.

[65] M. E. Aumer, S. F. LeBoeuf, F. G. McIntosh, and S. M. Bedair, "High optical quality AlInGaN by metalorganic chemical vapor deposition," <u>Applied Physics Letters</u>, vol. 75, pp. 3315, 1999.

[66] Y. Liu, T. Egawa, H. Ishikawa, T. Jimbo, "Growth and characterization of high quality quaternary AlInGaN epilayers on sapphire," <u>Journal of Crystal Growth</u>, vol. 259, pp. 245, 2003.

[67] S.-N. Lee, H.S. Paek, H. Kim, K.K. Kim, Y.H. Cho, T. Jang, Y. Park, "Growth and characterization of the AlInGaN quaternary protective layer to suppress the thermal damage of InGaN multiple quantum wells," <u>Journal of Crystal Growth</u>, vol. 310, pp. 3881, 2008.

[68]     E. Dimakis, A. Georgakilas, M. Androulidaki, K. Tsagaraki, G. Kittler, F. Kalaitzakis, D. Cengher, E. Bellet-Amalric, D. Jalabert, N.T. Pelekanos, "Plasma assisted MBE growth of quaternary InAlGaN quantum well heterostructures with room temperature luminescence," Journal of Crystal Growth, vol. 251, pp. 476, 2003.

[69]     G. Binnig, C. Quate, and C. Gerber, "Atomic force microscope," Physical Review Letters, vol. 56, pp. 930-933, 1986.

[70]     L. van der Pauw, "A method of measuring specific resistivity and hall effect of discs of arbitrary shape," Phillips Research Reports, vol. 13, pp. 1-9, 1958.

[71]     R. Erni, M. D. Rossell, C. Kisielowski, and U. Dahmen, "Atomic-resolution imaging with a sub-50-pm electron probe," Physical Review Letters, vol. 102, pp. 096101, 2009.

[72]     B. Heying, X. H. Wu, S. Keller, Y. Li, D. Kapolnek, B. P. Keller, S. P. DenBaars, and J. S. Speck, "Role of threading dislocation structure on the x-ray diffraction peak widths in epitaxial GaN films," Applied Physics Letters, vol. 68, pp. 643 645, 1996.

[73]     C. Ryang Wie, "High resolution x-ray diffraction characterization of semiconductor structures," Materials Science and Engineering: R: Reports, vol. 13, pp. 1, 1994.

[74]     B. D. Cullity, Elements of X-ray Diffraction, 2d ed. ed. Reading, Massachusetts: Addison-Wesley Pub. Co., 1978.

[75]     B. E. Warren, X-ray Diffraction. Reading, Massachusetts: Addison-Wesley Pub. Co., 1969.

[76]     R.F. Pierret, Semiconductor Device Fundamentals. Reading, Massachusetts: Addison-Wesley, 1996.

[77] W. Liu, Fundamentals of III-V Devices: HBTs, MESFETs, and HFETs/HEMTs. New York, New York: John Wiley & Sons, 1999.

[78] W. Liu, Handbook of III-V Heterojunction Bipolar Transistors. New York, New York: John Wiley & Sons, 1998.

[79] J.-H. Ryou, P. D. Yoder, J. Liu, Z. Lochner, H. Kim H., S. Choi, H.-J. Kim, and R. D. Dupuis, "Control of quantum-confined stark effect in InGaN-based quantum wells," IEEE Journal of Selected Topics in Quantum Electronics, vol. 15, pp. 1080-1091, 2009.

[80] P. Bhattacharya, Semiconductor Optoelectronic Devices. Englewood Cliffs, New Jersey: Prentice Hall, 1994.

[81] T. Suhara, Semiconductor Laser Fundamentals. New York, New York: Marcel Dekker, 2004.

[82] K. F. Brennan, The Physics of Semiconductors: with Applications to Optoelectronic Devices. Cambridge, Massachusetts: Cambridge University Press, 1999.

[83] J.C. Zolper, D.J. Rieger, A.G. Baca, S.J. Pearton, J.W. Lee, R.A. Stall, "Sputtered AlN encapsulant for high-temperature annealing of GaN," Applied Physics Letters, vol. 69, pp. 538, 1996.

[84] A.P. Zhang, G.T. Dang, F. Ren, J. Han, A.G. Baca, R.J. Shul, H. Cho, C. Monier, X.A. Cao, C.R. Abernathy, S.J. Pearton, "Direct-current characteristics of $pnp$ AlGaN/GaN heterojunction bipolar transistors," Applied Physics Letters, vol. 76, pp. 2943, 2000.

[85] K. Kumakura, T. Makimoto, N. Kobayashi, "Activation energy and electrical activity of Mg in Mg-doped In$_x$Ga$_{1-x}$N ($x$<0.2)," Japanese Journal of Applied Physics, vol. 39, pp. L337-L339, 2000.

[86]  T. Makimoto, K. Kumakura, N. Kobayashi, "High current gains obtained by InGaN/GaN double heterojunction bipolar transistors," Physica Status Solidi (a), vol. 188, no. 1, pp. 183-186, 2001.

[87]  T. Makimoto, K. Kumakura, and N. Kobayashi, "High current gains obtained by InGaN/GaN double heterojunction bipolar transistors with $p$-InGaN base," Applied Physics Letters, vol. 79, pp. 380, 2001.

[88]  T. Makimoto, K. Kumakura, and N. Kobayashi, "Reduced damage of electron cyclotron resonance etching by In doping into p-GaN," Journal of Crystal Growth, vol. 221, pp. 350-355, 2000.

[89]  T. Makimoto, K. Kumakura, and N. Kobayashi, "Extrinsic base regrowth of p-InGaN for Npn-type GaN/InGaN heterojunction bipolar transistors," Japanese Journal of Applied Physics, vol. 43, pp. 1922-1924, 2004.

[90]  T. Chung, D.M. Keogh, J.H. Ryou, D. Yoo, J. Limb, W. Lee, S.C. Shen, P.M. Asbeck, and R.D. Dupuis, "High current gain graded GaN/InGaN heterojunction bipolar transistors grown on sapphire and SiC substrates by metalorganic chemical vapor deposition," Journal of Crystal Growth, vol. 298, pp. 852-856, 2007.

[91]  T. Chung, J. Limb, D. Yoo, J.H. Ryou, W. Lee, S.C. Shen, R.D. Dupuis, B. Chu-Kung, M. Feng, D.M. Keogh, and P.M. Asbeck, "Device operation of InGaN heterojunction bipolar transistors with a graded emitter-base design," Applied Physics Letters, vol. 88, pp. 183501, 2006.

[92]  Y. Zhang, J.H. Ryou, R.D. Dupuis, and S.C. Shen, "A surface treatment technique for III-N device fabrication," in Digest of Papers: International Conference on Compound Semiconductor Manufacturing Technology, 2008, pp. 13.13.

[93] X.H. Wu, C.R. Elsass, A. Abare, M. Mack, S. Keller, P.M. Petroff, S.P. DenBaars, J.S. Speck, and S.J. Rosner, "Structural origin of V-defects and correlation with localized excitonic centers in InGaN/GaN multiple quantum wells," Applied Physics Letters, vol. 72, pp. 692, 1998.

[94] J.P. Liu, Y.T. Wang, H. Yang, D.S. Jiang, U. Jahn, K.H. Ploog, "Investigations on V-defects in quaternary AlInGaN epilayers," Applied Physics Letters, vol. 84, pp. 5449, 2004.

[95] Y.-C. Lee, Y. Zhang, H. J. Kim, S. Choi, Z. Lochner, R. D. Dupuis, J.-H. Ryou, and S.-C. Shen, "High-current-gain direct-growth GaN/InGaN double heterojunction bipolar transistors," IEEE Transactions on Electron Devices, vol. 57, no. 11, pp. 2964-2969, 2010.

[96] L. McCarthy, I. Smorchkova, H. Xing, P. Fini, S. Keller, J. Speck, S. P. DenBaars, M. J. W. Rodwell, and U. K. Mishra, "Effect of threading dislocations on AlGaN/GaN heterojunction bipolar transistors," Applied Physics Letters, vol. 78, pp. 2235, 2001.

[97] A. Hinoki, J. Kikawa, T. Yamada, T. Tsuchiya, S. Kamiya, M. Kurouchi, K. Kosaka, T. Araki, A. Suzuki, and Y. Nanishi, "Effects of traps formed by threading dislocations on off-state breakdown characteristics in GaN buffer layer in AlGaN/GaN heterostructure field-effect transistors," Applied Physics Express, vol. 1, pp. 011103, 2008.

[98] X. A. Cao, J. M. Teetsov, M. P. D'Evelyn, D. W. Merfeld, and C. H. Yan, "Electrical characteristics of InGaN∕GaN light-emitting diodes grown on GaN and sapphire substrates," Applied Physics Letters, vol. 85, pp. 7, 2004.

[99] W. Liu and J. S. Harris, Jr., "Diode ideality factor for surface recombination current in AlGaAs/GaAs heterojunction bipolar transistors," IEEE Transaction on Electron Devices, vol. 39, no. 12, pp. 2726-2732, 1992.

[100]  S.-C Shen, Y.-C. Lee , H. J. Kim, Y. Zhang, S. Choi, R. D. Dupuis, and J.-H. Ryou, "Surface leakage in GaN/InGaN double heterojunction bipolar transistors," IEEE Electron Device Letters, vol. 30, no. 11, pp. 1119-1121, 2009.

[101]  H. Chen, R. M. Feenstra, J. E. Northrup, T. Zywietz, and J. Neugebauer, "Spontaneous formation of indium-rich nanostructures on InGaN (0001) surfaces," Physical Review Letters, vol. 85, pp. 1902-1905, 2000.

[102]  I.-K. Park, M.-K. Kwon, S.-H. Baek, Y.-W. Ok, T.-Y. Seong, S.-J. Park, Y.-S. Kim, Y.-T. Moon, and D.-J. Kim, "Enhancement of phase separation in the InGaN layer for self-assembled In-rich quantum dots," Applied Physics Letters, vol. 87, pp. 061906, 2005.

[103]  A. Rice, R. Collazo, J. Tweedie, R. Dalmau, S. Mita, J. Xie, and Z. Sitar, "Surface preparation and homoepitaxial deposition of AlN on (0001)-oriented AlN substrates by metalorganic chemical vapor deposition," Journal of Applied Physics, vol. 108, pp. 043510, 2010.

[104]  M. Kneissl, Z. Yang, M. Teepe, C. Knollenberg, O. Schmidt, P. Kiesel, and N. Johnson, "Ultraviolet semiconductor laser diodes on bulk AlN," ," Journal of Applied Physics, vol. 101, pp. 123103, 2007.

[105]  J. R. Grandusky, M. Jamil, V. Jindal, N. Tripathi, and F. Shahedipour-Sandvik, "Identification of important growth parameters for the development of high quality $Al_{x>0.5}Ga_{1-x}N$ grown by metal organic chemical vapor deposition," Journal of Vacuum Science Technology A, vol. 25, pp. 441, 2007.

[106]  T. Ohba and R. Sato, "Growth of AlN on sapphire substrates by using a thin AlN buffer layer grown two-dimensionally at a very low V/III ratio," Journal of Crystal Growth, vol. 221, pp. 258-261, 2000.

[107]  H. Kawanishi, M. Senuma, and T. Nukui, "Anisotropic polarization characteristics of lasing and spontaneous surface and edge emissions from deep ultraviolet ($\lambda \approx 240$ nm) AlGaN multiple-quantum-well lasers," <u>Applied Physics Letters</u>, vol. 89, pp. 041126, 2006.

[108]  K. B. Nam, J. Li, M. L. Nakarmi, J. Y. Lin, and H. X. Jiang, "Unique optical properties of AlGaN alloys and related ultraviolet emitters," <u>Applied Physics Letters</u>, vol. 84, pp. 5264, 2004.

[109]  W.W. Chow and M. Kneissl, "Laser gain properties of AlGaN quantum wells," <u>Journal of Applied Physics</u>, vol. 98, pp. 114502, 2005.

[110]  J.E. Northrup, C. L. Chua, , C. L. Yang, T. Wunderer, M. Kneissl, N.M. Johnson, and T. Kolbe, "Effect of strain and barrier composition on the polarization of light emission from AlGaN/AlN quantum wells," <u>Applied Physics Letters</u>, vol. 100, pp. 021101, 2012.

[111]  J.J. Zhu, Y.M. Fan, H. Zhang, G.J. Lu, H. Wang, D.G. Zhao, D.S. Jiang, Z.S. Liu, .M. Zhang, G.F. Chen, B.S. Zhang, H. Yang, "Contribution of GaN template to the unexpected Ga atoms incorporated into AlInN epilayers grown under an indium-very-rich condition by metalorganic chemical vapor deposition (MOCVD)," <u>Journal of Crystal Growth</u>, vol. 348, no. 1, pp. 25, 2012.

[112]  R.C. Chiechi, E.A. Weiss, M.D. Dickey, G.M. Whitesides, "Eutectic gallium–indium (EGaIn): a moldable liquid metal for electrical characterization of self-assembled monolayers," <u>Angewandte Chemie International Edition</u>, vol. 47, pp. 142, 2008.

[113]  M.J. Regan, P.S. Pershan, O.M. Magnussen, B.M. Ocko, M. Deutsch, L.E. Berman, "X-ray reflectivity studies of liquid metal and alloy surfaces," <u>Physics Review B</u>, vol. 55, pp. 15874, 1997.

[114]  D. Zrnic, D. S. Swatik, "On the resistivity and surface tension of the eutectic alloy of gallium and indium," <u>Journal of Less-Common Metals</u>, vol. 18, no.1, pp. 67, 1969.

[115]  Z. Lochner, H.J. Kim, S. Choi, Y.-C Lee, Y Zhang, S.-C. Shen, J.-H. Ryou, R. D. Dupuis, "Growth and characterization of NpN heterojunction bipolar transistors with $In_{0.03}Ga_{0.97}N$ and $In_{0.05}Ga_{0.95}N$ bases," <u>Journal of Crystal Growth</u>, vol. 315, pp. 278, 2011.

[116]  Z. Lochner, H.J. Kim, Y.-C Lee, Y Zhang, S. Choi, S.-C. Shen, P. D. Yoder, J.-H. Ryou, R. D. Dupuis, "NpN-GaN/$In_xGa_{1-x}N$/GaN heterojunction bipolar transistor on free-standing GaN substrate," <u>Applied Physics Letters</u>, vol. 99, pp. 193501, 2011.

[117]  Z. Lochner, T.-T. Kao, Y.-S. Liu, X.-H. Li, Md. M. Satter, S.-C. Shen, P. D. Yoder, J.-H. Ryou, R. D. Dupuis, Y. Wei, H. Xie, A. Fischer, and F. A. Ponce, "Stimulated emission at 257 nm from optically-pumped AlGaN/AlN heterostructure on AlN substrate," <u>Physica Status Solidi A</u>, accepted for publication, 2013.

[118]  Z. Lochner, T.-T. Kao, Y.-S. Liu, X.-H. Li, Md. M. Satter, S.-C. Shen, P. D. Yoder, J.-H. Ryou, R. D. Dupuis, Y. Wei, H. Xie, A. Fischer, and F. A. Ponce. Ponce, "Room-temperature optically pumped AlGaN-AlN multiple-quantum-well lasers operating at <260 nm   grown by metalorganic chemical vapor deposition ," <u>Proceedings of the SPIE</u>, vol. 8625, pp. 862519, 2013.

[119]  Z. Lochner, T.-T. Kao, Y.-S. Liu, X.-H. Li, Md. M. Satter, S.-C. Shen, P. D. Yoder, J.-H. Ryou, R. D. Dupuis, Y. Wei, H. Xie, A. Fischer, and F. A. Ponce. Ponce,, "Deep-Ultraviolet Lasing at 243 nm from Photo-Pumped AlGaN/AlN Heterostructure on AlN Substrate," <u>Applied Physics Letters</u>, vol. 102, pp. 101110, 2013.

# VITA

Zachary Meyer Lochner was born April 7$^{th}$, 1985 in Buffalo, NY to Thomas Lochner and Joan Meyer. After graduating from Williamsville East High School in 2003, he enrolled as a Distinguished Honor's Scholar at the State University of New York at Buffalo. Majoring in Electrical Engineering with minors in both Mathematics and Computer Science, Zachary earned his Bachelor of Science with Distinction in 2007. He also received the prestigious SUNY Chancellors Award, granted to just a handful of the graduating class amongst all disciplines, for his scholastic achievement and commitment to the SUNY-Buffalo community. In the Fall of 2007, he enrolled in the graduate program at the Georgia Institute of Technology as a Presidential Fellow, and joined with Dr. Dupuis' lab group in the Center for Compound Semiconductors. Zachary received his Master of Science in ECE in 2010, and completed his PhD in 2013 with a minor in Material Science.

This dissertation was typed by the author.